ADSORPTION OF CHLOROQUINE AND MALACHITE GREEN DYE USING MODIFIED AGROWASTES AND THEIR ZINC OXIDE COMPOSITE NANOMATERIALS

BY

TOKULA, BLESSING ENYOJO

(19PGCE000071)

A DISSERTATION SUBMITTED TO THE DEPARTMENT OF PHYSICAL SCIENCES, LANDMARK UNIVERSITY OMU-ARAN, IN PARTIAL FULFILMENT OF THE REQUIREMENTS FOR THE AWARD OF THE DEGREE OF MASTER OF SCIENCE (M.Sc.) IN CHEMISTRY

AUGUST, 2021

DECLARATION

I, TOKULA, BLESSING ENYOJO, a Master of Science student in the Physical Sciences Department, Landmark University, Omu-Aran, hereby declare that this dissertation entitled "Adsorption of Chloroquine and Malachite Green Dye Using Modified Agro-wastes and their Zinc Oxide Composite Nanomaterials", submitted by me is based on my original work. Any material(s) obtained from other sources or work done by any other persons or institutions have been duly acknowledged.

Student's Full Name and Matriculation number

Signature and Date

CERTIFICATION

This is to certify that this dissertation has been read and approved as meeting the requirements of the Department of Physical Sciences, Landmark University, Omu-Aran, Nigeria, for the award of Master's degree.

_____	_____
Dr. A. O. Dada (Supervisor)	Date
_____	_____
Dr. A. A. Inyinbor (Co-Supervisor)	Date
_____	_____
Dr. A. A. Inyinbor (Head of Department)	Date
_____	_____
Prof. F.A Adekola (External Examiner)	Date

ABSTRACT

Indiscriminate industrial and domestic discharge of effluents into water bodies have increased the level of water pollution via anthropogenic activities. Chloroquine (CQ) pharmaceutical and malachite green (MG) dye are a group of emerging contaminants whose unavoidable use leads to traces of them in water bodies. The dire consequences and hazardous effects they induce on both humans and aquatic life have raised concerns amongst researchers and hence the need to develop cheap methods for removing these eco-threatening contaminants. The use of effective and low-cost adsorbent such as rice husk and plantain peel will contribute to the availability of sustainable eco-friendly waste disposal methods and pollutant removal. This research therefore aimed at investigating the adsorption of CQ pharmaceutical and MG dye using modified agro-waste and their zinc oxide nanocomposites. The characterization of adsorbents alongside kinetic studies, mechanism, isotherm and thermodynamics were carried out.

Rice husk activated carbon (RHAC) and plantain peel activated carbon (PPAC) serving as base materials were successfully prepared by carbonization and chemical activation using 1 M H_3PO_4 (Orthophosphoric acid) for 1 hr at 400 ^oC. Zinc oxide (ZnO) nanoparticles was prepared and loaded on the base materials by precipitation and bottom-up approach using Zinc Nitrate solution (0.45 M) and NaOH (1.0M). The resulting ZnO nanocomposites (RHAC-ZnO-NCs and PPAC-ZnO-NCs) were thereafter calcinated in the muffle furnace for 4 h at 350°C. All adsorbents were characterized by series of physicochemical techniques such as ash and moisture content, volatile matter, Boehm titration, surface area determination using sears method, Iodine number, X-ray Diffraction (XRD), Scanning Electron Microscopy (SEM) and the surface functional group determined via Fourier Transform Infrared (FTIR). PPAC, RHAC, PPAC-ZnO-NCs and RHAC-ZnO-NCs were utilized for adsorptive uptake of malachite green dye and chloroquine via the batch adsorption technique. Various operational parameters (pH, initial concentrations, temperature and agitation time) were investigated to understand their effect on the removal efficiency and quantity adsorbed.

The physicochemical parameters determined for RHAC, RHAC-ZnO-NCs, PPAC, and PPAC-ZnO-NCs showed pH values within range of 6.53 and 7.21, pH_{pzc} (4.98-6.21), bulk density (0.37-0.88), moisture content (7.31-9.21 %), ash content (12.18- 18.45 %) and volatile matter (30.31-35.64 %). The SEM images showed the existence and availability of pores on the surface of each adsorbent which serve as sites for adsorption. XRD results on the nanocomposites also established the loading of ZnO nanoparticles onto the nanocomposites. The FTIR analysis for all adsorbents showed the presence of functional groups and the corresponding appearance, disappearance and shifting of peaks after loading with ZnO nanoparticles. Adsorption studies showed that adsorbate uptake increased with corresponding increase in temperature. Adsorption of CQ and MG dye was obtained within pH 6-9 at temperature 303 K with highest removal of 95.32 and 76.99 % for CQ and MG dye respectively. Equilibrium data were better described by Freundlich isotherm model and Pseudo second order (PSO) best described the kinetic data. The Langmuir maximum monolayer adsorption capacities (Q_{max}) calculated for adsorption of CQ ranged from 31.94 to 169.49 mg/g for all adsorbents and Q_{max} for adsorption of MG ranged from 33.67 to 77.51 mg/g. Q_{max} values obtained in this study surpassed other reported adsorbents in comparison, thereby indicating their unique quality and better performance ability. Thermodynamic parameters obtained suggested the endothermic nature of the adsorption process as all enthalpy(ΔH) values were positive. The positive entropy (ΔS) values and negative values of free energy change (ΔG) indicated that the adsorption of CQ and MG onto the adsorbents is rapid, random and spontaneous in nature.

In conclusion, these adsorbents have been found to be very efficient in removing CQ and MG dye from their solutions. This study may be useful for environmental protection and conservation.

DEDICATION

This work is dedicated to the Lord, God Almighty.

TABLE OF CONTENT

CERTIFICATION ii

ABSTRACT iii

DEDICATION v

TABLE OF CONTENT vi

ACKNOWLEDGEMENT x

LIST OF TABLES xi

LIST OF FIGURES xiii

LIST OF SYMBOLS xvi

CHAPTER ONE 1

1.0 INTRODUCTION 1

1.1 Background of Study 1

1.2 Statement of Problem 3

1.3 Scope of Study 3

1.4 Justification of Study 3

1.5 Significance of Research 4

1.6 Aim and Objectives 5

CHAPTER TWO 6

2.0 LITERATURE REVIEW 6

2.1 Pharmaceuticals 6

2.1.1 Chloroquine 7

2.2 Toxicity of Dyes 8

2.2.1 Malachite Green 9

2.3 Agricultural Waste as Precursor Material for Adsorbents 9

2.3.1 Rice Husk 10

2.3.2 Plantain Peel 10

2.4 Adsorption process 11

2.5 Rice husk Activated Carbon for the Sorption of Different Pollutants. 12

2.6 Plantain Peel Activated Carbon for The Sorption of Different Pollutants 13

2.7 Adsorption of Dyes and Pharmaceuticals using Agro-wastes 14

2.8 Nanoparticles and Nanocomposites 15

2.9 Nanoparticles and Nanocomposites for the Sorption of pollutants 16

CHAPTER THREE 18
MATERIALS AND METHODS 18
3.1 Materials 18
3.1.1 Raw materials 18
3.1.2 Reagents 18
3.1.3 Glassware /apparatus 18
3.2 Methods 18
3.2.1 Raw Materials Collection 18
3.2.2 Material Preparation/Carbonization 18
3.2.3 Chemical activation of Rice Husk/Plantain Peel using H_3PO_4 19
3.2.4 ZnO Nano-Composites Synthesis 19
3.3 Adsorbent Characterization 19
3.3.1 Determination of pH 19
3.3.2 Moisture Content 20
3.3.3 Ash Content 20
3.3.4 Volatile Matter 20
3.3.5 Bulk density 21
3.3.6 Simple Specific Surface Area Via Saer's method 21
3.3.7 Point of Zero-charge (pH_{pzc}) 21
3.3.8 Iodine Number 22
3.3.9 Boehm Titration 22
3.3.10 Scanning Electron Microscopy (SEM) 23
3.3.11 Fourier Transform Infrared (FTIR) Analysis 23
3.3.12 X-ray Diffraction (XRD) Analysis. 23
3.4 Adsorption Experiment 24
3.4.1 Preparation of Adsorbates 24
3.4.2 Batch Adsorption 24
3.4.2.1 Effects of pH 24
3.4.2.2 Effects of Contact time 24
3.4.2.3 Effects of Temperature 25
3.4.2.4 Effects of Initial Concentration 25
3.5 Isotherm Models 25

3.5.1 Langmuir Isotherm 25
3.5.2 Freundlich Isotherm 26
3.5.3 Temkin Isotherm 27
3.5.4 Dubinin-Radushkevich isotherm 27
3.6 Adsorption Kinetics 28
3.6.1 Pseudo-First Order Kinetics 28
3.6.2 Pseudo-Second Order Kinetics (PSO) 29
3.6.3 Elovich Kinetic Model 29
3.6.4 Intraparticle Diffusion (IPD) Model 29
3.7 Thermodynamics Models 30
3.8 Statistical Validity Models 31
CHAPTER FOUR 32
4.0 RESULTS AND DISCUSSION 32
4.1 Characterization of Adsorbents 32
4.1.1 Determination of Oxygen containing Functional groups (Boehm Titration) 34
4.1.2 Iodine number determination 35
4.1.3 Fourier Transform Infrared Analysis (FTIR) 36
4.1.4 Scanning Electron Microscopic (SEM) Analysis. 40
4.1.4.1 Scanning Electron Microscopic (SEM) studies on RHAC 40
4.1.4.2 Scanning Electron Microscopic studies on RHAC-ZnO-NC 41
4.1.4.3 Scanning Electron Microscopic studies on PPAC 42
4.1.4.4 Scanning Electron Microscopic studies on PPAC-ZnO-NC 42
4.1.5 XRD analysis on Nano Composites 43
4.2 Chloroquine Adsorption Studies 46
4.2.1 Maximum Adsorption wavelength for Chloroquine 46
4.2.2 Calibration Curve for Chloroquine 46
4.2.3 Adsorption Studies of Chloroquine onto RHAC, PPAC, RHAC-ZnO-NC and PPAC-ZnO-NC. 47
4.2.3.1 Effects of Contact Time, Initial Concentration, and Temperature 47
4.2.3.2 Effects of pH 52
4.2.3.3 Isotherm Studies 53
4.2.3.4 Kinetic Studies 64

4.2.3.5 Thermodynamic Studies 78
4.3. Malachite Green Adsorption Studies. 81
4.3.1 Maximum Adsorption wavelength (λ_{max}) for Malachite Green 81
4.3.2 Calibration Curve for Malachite Green 81
4.3.3 Adsorption Studies of Malachite Green Dye onto RHAC, PPAC, RHAC-ZnO-NC and PPAC-ZnO-NC. 82
4.3.3.1 Effects of Contact Time, Initial Concentration and Temperature 82
4.3.3.2 Effects Of pH 87
4.3.3.3 Isotherm Studies 88
4.3.3.4 Kinetic Studies. 100
4.3.3.5 Thermodynamic Studies 114
CHAPTER FIVE 117
5.0 SUMMARY, CONCLUSION AND RECOMMENDATION 117
5.1 Summary 117
5.2 Conclusion 118
5.3 Recommendations 118
5.4 Contributions to knowledge 119
REFERENCES 120
APPENDICES 137

ACKNOWLEDGEMENT

My deepest gratitude is to the Almighty God who has preserved, kept and provided for me all through this Master's program.

Words fail me on how much I appreciate my supervisor, mentor and tutor. 'Dr. A.O Dada' for his support, guidance, patience and encouragement throughout the timeline of this research and my Master's degree program. Despite his tight schedule, he is always available whenever his attention is needed and gave the necessary assistance that was needed. My appreciation also goes to the Head of Department, Physical Sciences, who served as my co-supervisor. Dr. A.A. Inyinbor. Thank you, ma, for all your guidance, encouragement and meticulousness to ensure that my work is nothing but the best. May God richly bless and reward you.

To our father in the department and award-winning Prof. O.S Bello who is always ready to assist, encourage and spur me to achieve the best results. I am deeply grateful Sir for all your support and guidance throughout the period of this research. To the postgraduate coordinator for the department, Dr. S.O. Ikubanni and my Lecturers in the department: Dr A.P. Oluyori, Dr. G.O. Egbaherva, Dr. T.O. Abodurin, Mr. S.O. Oluwole, Mrs. D. Bankole, and Mrs. A.C. Oladipo, for their guidance, advice, and support.

To my loving parents, Dr and Mrs. Tokula for their unending love, prayers and support. My siblings Emmanuel Tokula, Abigail Tokula and Deborah Tokula for their support throughout my project work. My sincere gratitude goes to my laboratory colleagues, Mr Tobi Agboola, Mr. Isaac Adesina, Miss Boluwape Okikiola and Miss Atunwa Bukola, your encouragements and constant help is deeply appreciated.

I appreciate the Industrial chemistry laboratory technologists Miss Afolabi, Mrs. Ajayi, and Mr. Olorunfemi for their efforts and support. Also, I appreciate the faculty and staff of Animal Science, Biochemistry and Microbiology departments for the kind support, Mr. Peter, Mr. Damilare, Mr. Yomade, Mr. Leke.

I deeply appreciate my friends whose timely help and encouragement really helped me. Mr. Falana Babatunde and Mr. Moses Ekemini. May God richly bless and reward you.

LIST OF TABLES

Table 2.1: Properties of Chloroquine 8
Table 2.2: Modified agro-wastes used for the adsorption of various pharmaceuticals and dyes. 14
Table 2.3: Properties of Nanoparticles 16
Table 4.1: Physicochemical parameters of adsorbents 31
Table 4.2: Oxygen Containing Functional groups 33
Table 4.3: Iodine Adsorption values 34
Table 4.4: FTIR bands of RHAC and RHAC-ZnO-NC and their possible functional groups. 36
Table 4.5: FTIR bands of PPAC and PPAC-ZnO-NC and their possible functional groups. 38
Table 4.6: Adsorption Isotherm Parameters for uptake of using RHAC at different temperatures 51
Table 4.7: Adsorption Isotherm Parameters for uptake of using RHAC-ZnO-NC at different temperatures 53
Table 4.8: Adsorption Isotherm Parameters for uptake of using PPAC at different temperatures. 55
Table 4.9: Adsorption Isotherm Parameters for uptake of CQ using PPAC-ZnO-NC at different temperatures
Table 4.10: Maximum Monolayer Adsorption Capacity of Adsorbents in this study in comparison with other agrowastes and nanocomposites for pharmaceutical uptake. 58
Table 4.11: Parameters of Kinetic Model for CQ Uptake using RHAC 64
Table 4.12: Parameters of Kinetic Model for CQ Uptake using RHAC-ZnO-NC. 67
Table 4.13: Parameters of Kinetic Model for CQ Uptake using PPAC 71
Table 4.14: Parameters of Kinetic Model for CQ Uptake using PPAC-ZnO-NC 75
Table 4.15: Outlined Thermodynamics Data for the Adsorption of CQ onto RHAC 76

Table 4.16: Outlined Thermodynamics Data for the Adsorption of CQ onto RHAC-ZnO-NC. 76
Table 4.17: Outlined Thermodynamics Data for the Adsorption of CQ onto PPAC 76
Table 4.18: Outlined Thermodynamics Data for the Adsorption of CQ onto RHAC 76
Table 4.19: Adsorption Isotherm Parameters for uptake of MG using RHAC at different temperatures 87
Table 4.20: Adsorption Isotherm Parameters for uptake of MG using RHAC-ZnO-NC at different temperatures 89
Table 4.21: Adsorption Isotherm Parameters for uptake of MG using PPAC at different temperatures 91
Table 4.22: Adsorption Isotherm Parameters for uptake of MG using PPAC-ZnO-NC at different temperatures 93
Table 4.23: Maximum Monolayer Adsorption Capacity of Adsorbents in this study in comparison with other agrowastes and nanocomposites for MG Dye uptake. 94
Table 4.24: Parameters of Kinetic Model for MG Uptake using RHAC 98
Table 4.25: Parameters of Kinetic Model for MG Uptake using RHAC-ZnO-NC 102
Table 4.26: Parameters of Kinetic Model for MG Uptake using PPAC 106
Table 4.27: Parameters of Kinetic Model for MG Uptake using PPAC-ZnO-NC 109
Table 4.28: Outlined Thermodynamics Data for the Adsorption of MG onto RHAC 110
Table 4.29: Outlined Thermodynamics Data for the Adsorption of MG onto RHAC-ZnO-NC 110
Table 4.30: Outlined Thermodynamics Data for the Adsorption of MG onto PPAC 110
Table 4.31: Outlined Thermodynamics Data for the Adsorption of MG onto RHAC-ZnO-NC. 110

LIST OF FIGURES

Figure 2.1	Routes of pharmaceuticals	7
Figure 2.2	Structure and 3D structure of chloroquine	8
Figure 2.3	Structure of Malachite green	9
Figure 2.4	Rice Husk	10
Figure 2.5	Plantain peels	10
Figure 4.1	pH(pzc) for (A) RHAC (B) RH-ZnO-NC (C) PPAC (D) PP- ZnO-NC. .	32
Figure 4.2	FTIR spectra of (a) RHAC (b) RHAC-ZnO-NC	37
Figure 4.3	FTIR spectra of (a) PPAC and (b) PPAC-ZnO-NC	39
Figure 4.4	Scanning Electron Micrograph of RHAC	41
Figure 4.5	Scanning Electron Micrograph of RHAC-ZnO-NC	41
Figure 4.6	Scanning Electron Micrograph of PPAC	42
Figure 4.7	Scanning Electron Micrograph of PPAC-ZnO-NC	43
Figure 4.8	(A) XRD pattern and (B) pie chart distribution of RHAC-ZnO-NC.	44
Figure 4.9	(A) XRD pattern and (B) pie chart distribution of PPAC-ZnO-NC.	45
Figure 4.10	Absorbance Spectrum of Chloroquine	46
Figure 4.11	Calibration Curve for CQ adsorption	47
Figure 4.12	Effects of Concentration and Contact time for CQ-RHAC system	49
Figure 4.13	Effects of Initial Concentration and Contact time on CQ uptake unto RHAC-ZnO-NC	49
Figure 4.14	Effect of concentration and contact time for uptake of CQ onto PPAC	50
Figure 4.15	Effect of concentration and contact time for uptake of CQ onto PPAC-ZnO-NC	50
Figure 4.16	Effect of temperature on the uptake of CQ onto (A)RHAC (B)RHAC-ZnO-NC (C)PPAC (D)PPAC-ZnO-NC.	51
Figure 4.17	Effects of pH on uptake of CQ onto (A) RHAC (B) RHAC-ZnO-NC (C) PPAC and (D) PPAC-ZnO-NC.	53

Figure 4.18 (A)Langmuir (B) Freundlich (C)Temkin and (D) D-R linear Isotherm plots for RHAC-CQ System. 56

Figure 4.19 (A)Langmuir (B) Freundlich (C)Temkin and (D) D-R linear Isotherm plots for RHAC-ZnO-NC-CQ System. 58

Figure 4.20 (A)Langmuir (B) Freundlich (C)Temkin and (D) D-R linear Isotherm plots for PPAC-CQ System 60

Figure 4.21 (A)Langmuir (B) Freundlich (C)Temkin and (D) D-R linear Isotherm plots for PPAC-ZnO-NC-CQ System 62

Figure 4.22 Plot of (A) PFO (B) PSO (C) Elovich and (D) IPD for RHAC-CQ system 67

Figure 4.23 Plot of (a) PFO (b) PSO (c) Elovich and (d) IPD for RHAC-CQ system. 70

Figure 4.24 Plot of PFO, PSO, Elovich and intraparticle diffusion for PPAC-CQ system. 73

Figure 4.25 Plot of (a)PFO (b)PSO (c) Elovich and (d) Intraparticle diffusion for PP-ZnO-NC-CQ system 76

Figure 4.26 Van't Hoff Plot for (a) RHAC-CQ System and (b) RHAC/ZnO-CQ System (C) PPAC-CQ and (D) PPAC-ZnO-NC 79

Figure 4.27 The absorbance spectrum of Malachite green 81

Figure 4.28 Calibration Curve for MG adsorption 82

Figure 4.29 Effects of Concentration and Time for RHAC-MG adsorption System. 84

Figure 4.30 Effects of Concentration and Contact time for uptake of MG onto RHAC-ZnO 84

Figure 4.31 Effects of Concentration and Contact time on the uptake of MG by PPAC 85

Figure 4.32 Effects of initial concentration and contact time for the uptake of MG onto PPAC-ZnO-NC 85

Figure 4.33 Effects of Temperature on MG uptake onto (A)RHAC (B)RHAC-ZnO-NC (C) PPAC (D)PPAC-ZnO-NC 86

Figure 4.34 Percentage of MG Adsorbed by (A) RHAC (B) RHAC-ZnO-NC (C) PPAC and (D) PPAC-ZnO-NC at Different pH 88

Figure 4.35 (A)Langmuir (B) Freundlich (C)Temkin and (D) D-R linear Isotherm plots for MG-RHAC System 91

Figure 4.36 (A)Langmuir (B) Freundlich (C)Temkin and (D) D-R linear Isotherm plots for MG-RHAC-ZnO-NC System 93

Figure 4.37 (A)Langmuir (B) Freundlich (C)Temkin and (D) D-R linear Isotherm plots for MG-PPAC System 95

Figure 4.38 (A)Langmuir (B) Freundlich (C)Temkin and (D) D-R linear Isotherm plots for MG-PPAC-ZnO-NC System. 97

Figure 4.39 Plot of (a) PSO (b) PFO (c) Elovich and (d) IPD plot for RHAC-MG System. 103

Figure 4.40 Plot of (a) PSO (b) PFO (c) Elovich and (d) IPD for RH-ZnO-NC-MG System. 106

Figure 4.41 Plot of (a) PSO (b) PFO (c) Elovich and (d) IPD for PPAC-MG System 109

Figure 4.42 Plot of (a) PSO (b) PFO (c) Elovich and (d) IPD for PPAC-ZnO-MG system 112

Figure 4.43 Van't Hoff Plot for the adsorption of MG onto (A) RHAC (B) RHAC/ZnO-NC (C) PPAC (D) PPAC-ZnO-NC 115

LIST OF SYMBOLS

C_e Concentration of adsorbate remaining at equilibrium (mg L^{-1})

C_o Initial Concentration of adsorbate (mg L^{-1})

V Volume of prepared adsorbate.

W Dry weight of adsorbent (grams)

q_t quantity of adsorbate at a specific time (mg g^{-1})

Q_e Amount of adsorbate at equilibrium (mgg^{-1})

Q_{max} Monolayer Coverage Capacity (maximum) of adsorbents from the Langmuir isotherm (mg g^{-1})

K_2 Rate Constant (Pseudo second order) (g/mg min)

k_1 Rate Constant (Pseudo first order) (min^{-1})

h_2 initial adsorption rate (Pseudo second order) (g^2/mg^2 min)

h_1 initial adsorption rate (Pseudo first order) (g/mg min)

K_F Isotherm Constant (Freundlich Isotherm)

K_L Isotherm constant (Langmuir Isotherm) (L mg^{-1})

α Rate equation of Elovich (g min^2/mg)

β Rate equation of Elovich (g min/mg)

R Gas constant (J/mol K)

A_T Isotherm equilibrium binding constant of the Temkin isotherm

b_T Isotherm Constant from the Temkin Isotherm (L g^{-1})

n_F Freundlich Isotherm exponent

R_L Separation factor from Langmuir isotherm (Dimensionless constant)

CHAPTER ONE

1.0 INTRODUCTION

1.1 Background of Study

Water is of utmost importance for life and survival of both plants and animals on earth. It is a very important natural resource as about 71 % of the total earth surface is water, although only about 2.5 % is fresh water (Rajasulochana & Preethy, 2016). Increasing human population and technological advancement has led to the establishment of many industries such as textile, pharmaceutical, petroleum, mining, etc. in various parts of the world. These industries however require large quantities of water daily for proper running and functioning of their daily operations. Contaminated effluents are inevitably released from these industries carrying a wide range of pollutants including traces of dyes, pharmaceuticals, heavy metals, pesticides, etc. into the water bodies, hence leading to severe cases of contamination and other negative health and environmental hazards (Okereke & Obasi, 2016).

Pharmaceuticals are a wide range of drugs with various physico-chemical properties and therapeutic effects used for the treatment, diagnosis and prevention of human and animal diseases (Renita, Kumar, Srinivas, Priyadharshini, & Karthika, 2017). Several studies have shown that the detection and presence of pharmaceuticals in the environment is a matter of concern with their increased and continued use (in veterinary and human medicine) leading to their continued release into the environment (Agboola & Bello, 2020). After use by humans and animals, a large portion (about 90%) of the administered dose of pharmaceuticals remain undegradable in the body and these undegraded or partly degraded metabolites are excreted (unchanged of converted back to the initial active compound through bacterial action) through sweat, urine and feaces and find their way into the environment (Olarinmoye, Bakare, Ugwumba, & Hein, 2016). The disposal of unused drugs into the sewage system, effluent discharge from pharmaceutical industries and leaching from the soil also introduces these metabolites into the environment as the treated sewage can be recycled and used for irrigation and other farming activities (Yazidi *et al.,*

2019).The existence of pharmaceuticals in potable water has shown that conventional waste treatment techniques are not effective in removing these pharmaceuticals, thus posing a risk to public health and aquatic life (Mountassir *et al.,* 2020).

Dyes are compounds that impact colour on a material. Dyes can be grouped based on their solubility and chemical properties. Dyes which are soluble in water include mordant, basic, acid and direct dyes while dyes insoluble in water include vat, reactive, disperse, azoic and Sulphur dyes. Their complex structures and synthetic origin make them inert, not easily biodegraded and highly toxic (Adegoke & Bello, 2015). They are also highly hazardous to the human health on account of their carcinogenic and mutagenic properties. As almost all industries use dyes, the yearly consumption is about 10,000 tons and disposal have become a challenge. Over 10-15 % are indiscriminately introduced into water bodies which have undesirable effects on aquatic life and humans. Exposure to dyes can lead to skin diseases, cancer, hormonal disruptions, etc. Introduction of dyes into the environment may cause a decline in photosynthesis, thereby leading to atmospheric changes and causing changes in the life cycle of organisms and dissolved oxygen depletion. The removal of dyes is therefore very necessary (Zhang *et al.,* 2013).

Studies have established the efficacy of the adsorption process for the uptake of a variety of pollutants (Rudd *et al.,* 2016). This process requires low initial cost, simple operation and high efficiency. Amongst the various adsorbents such as clay, chitosan, silica gel, activated alumina, etc. the activated carbon has been found to be very efficient and is preferred by dint of their large surface area, multiple sites for adsorption, high porosity, functional groups and ease of modification (Ahmed, Zhou, Ngo, Johir, & Sornalingam, 2017). However, the cost of the precursor for the commercially sold activated carbon is high, therefore the need to identify more cost-effective alternatives. Agricultural wastes and by-products have been identified as cheap and efficient alternatives that could be applied as adsorbents in the removal of various types of pollutants ranging from dyes (Adegoke & Bello, 2015; Ojediran *et al.,* 2020), phenols (Anna, Jens, Olov, Thomas, & Schroder, 2018), heavy metals (Dada *et al.,* 2017; Cruz *et al.,* 2020). Researchers have therefore found ways to improve the uptake capacity and efficiency of agro waste adsorbents by surface modification so as to improve the surface area and porosity

(Alipanahpour, Ghaedi, Asfaram, Mehrabi, & Fardin, 2019). This can be carried out through carbonization (physical activation), chemical activation (using acids, bases or salts) (Adegoke & Bello, 2015b)**.**

Formation of nanocomposites with the activated carbon creates and incorporates unique features, higher surface area and produces adsorbents with higher uptake capacity. These composites have high reusability capacity and can be applied multiple times without losing their efficiency (Masoudian, Rajabi, & Ghaedi, 2019).

1.2 Statement of Problem

Every living thing needs water for their survival. The discovery and detection of pollutants (pharmaceuticals and dyes) in water bodies attributed to the indiscriminate discharge of industrial effluent, is of great concern as it induces unfriendly and hazardous effects on the environment and affects aquatic life. Cheap and effective techniques for treatment and effective uptake of these contaminants from water, industrial effluents and domestic sewage are therefore needed.

1.3 Scope of Study

The present study utilizes rice husk (RH) and plantain peel (PP) to produce activated carbon using Orthophosphoric acid. Zinc Oxide (ZnO) Nanoparticles was then loaded onto the activated carbon. Characterization was carried out on the activated carbon and nano composites. The efficiency of activated carbon and nano composites to sequester chloroquine (CQ) and malachite green (MG) dye was studied.

1.4 Justification of Study

Due to the unavoidable use of CQ and MG dye, it is of great necessity to develop cheap methods for removing these eco-threatening contaminants. The use of effective and low-cost adsorbent such as rice husk and plantain peel will contribute to the availability of sustainable eco-friendly waste disposal methods and pollutant removal. Findings from this work will help provide cheap, effective, and readily available agricultural wastes that can be used to sequester CQ and MG dye from wastewater. To the best of our knowledge, no reported studies have been found on the adsorptive uptake of CQ onto agro-wastes and

nanocomposites. MG dye adsorption has however been reported, for other materials except agro-waste based nanocomposites. Hence, the need for this study.

1.5 Significance of Research

The significance of the current research is to investigate the efficiency and efficacy of an alternative bio adsorbent from rice husk and plantain peel waste for the removal of CQ pharmaceutical and MG dye. Plantain peel and rice husk are commonly found as local wastes in Nigeria which are mostly burnt or indiscriminately discarded into water bodies and litter most market places in developing countries and thereby leading to more environmental problems.

Recently, activated carbon from agricultural wastes have been successfully applied to biosorption process for removal of pharmaceuticals such as ciprofloxacin (Agboola and Bello, 2020), Paracetamol (Saucier *et al.,* 2017), amoxicillin (Chandrasekaran, Patra, Narayanasamy, & Subbiah, 2020), ibuprofen (Bello, Alao, Alagbada, & Olatunde, 2019) and dyes such as rhodamine B (Adekola *et al.,* 2018; Bello *et al.,* 2017; Dada *et al.,* 2019; Inyinbor *et al.,* 2016) Malachite green (Choudhary, Kumar, & Neogi, 2020; Malik, Ramteke, & Wate, 2007; Ojediran *et al.,* 2020). To the best of our knowledge, no reported research aimed at investigating the removal of chloroquine pharmaceutical and MG dye using nano composites loaded unto rice husk and plantain peel activated carbon exists. The conversion of these agro waste into activated carbon can help rice mills in reducing the disposal problem of rice husk waste thereby producing a value-added product from an unwanted agricultural waste, which contributes to solving part of the environmental and waste water problems that are germane to the sustainable development goals (SDG). This study is therefore targeted towards achieving SDG goal 6 (clean water and sanitation) and SDG 11(Sustainable cities and communities) of the United Nation goals.

1.6 Aim and Objectives

This research aimed at investigating the adsorption of CQ pharmaceutical and MG dye using modified agro-waste and Zinc Oxide composite nanomaterials.

The objectives of the study were to:

i. Prepare activated carbon using agro wastes (rice husk and plantain peel) by carbonization and chemical activation
ii. Prepare nanocomposites by loading ZnO nanoparticles onto the activated carbon.
iii. Prepare nanocomposites by loading ZnO nanoparticles onto the activated carbon.
iv. Characterize the prepared adsorbents using physicochemical and spectroscopic techniques.
v. Investigate the adsorption capacity of nanocomposites for the uptake of CQ pharmaceutical and MG dye.

CHAPTER TWO

2.0 LITERATURE REVIEW

2.1 Pharmaceuticals

This is a general term used to describe chemicals with biological activity applied for the treatment, diagnosis and prevention of diseases which includes veterinary and even illicit drugs. A broad variety of pharmaceuticals exist ranging from antibiotics to anti-inflammatory drugs to antimalarial drugs to contraceptives and anti-depressants amongst others.

Pharmaceuticals are introduced into the environment as metabolites or in their parent form via various routes. As illustrated in Figure 2.1, after consumption by humans or animals, undegraded pharmaceutical metabolites are excreted either through sweat, urine or feaces. The unused drugs are also discarded indiscriminately as domestic sewage. Industrial effluents also serve as a channel for introduction of pharmaceuticals into receiving water bodies. The increase in pharmaceutical consumption, has led to increase in production and effluent discharge into surface waters (Olarinmoye *et al.,* 2016). Other pharmaceuticals find their way to aquatic environment after direct applications through manure and in aquaculture.

These metabolites reach the waste water treatment plants (WWTPs) where they form other toxic and harmful products. These harmful products formed are more toxic than their parent compounds and are often times discharged with industrial effluents into lakes, rivers and other aquatic environment. Where through the action of microorganisms, these metabolic compounds can be changed back to their parent form. As such, the presence of pharmaceuticals in surface and ground water has become an issue of concern among researchers.(Lindroos, Hörnström, Larsson, Gustavsson & Maris, 2019).

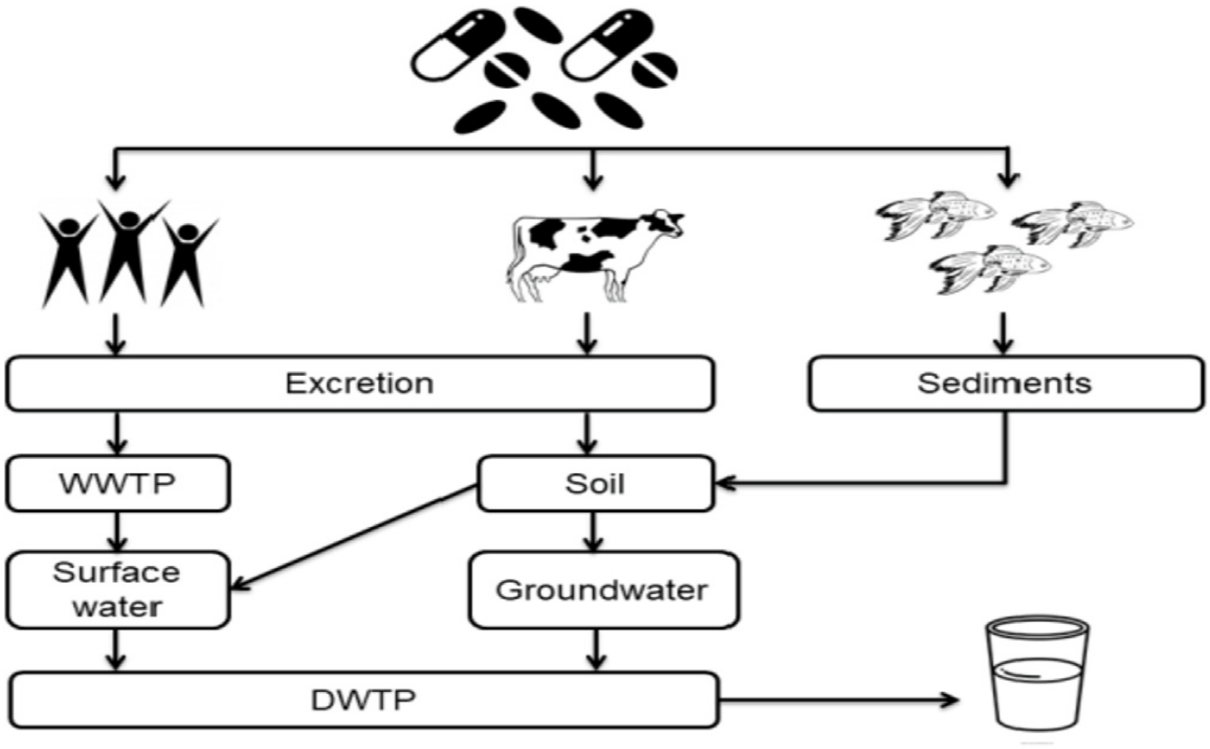

Figure 2.1: Routes of pharmaceuticals (Quesada et al., 2019).

2.1.1 Chloroquine

Chloroquine (CQ) with IUPAC name (7-chloro-4-(4-diethylamino-l-methylbutylamino)-quinoline) is a group of quinoline synthesized to be used as an antimalaria drug (Lindroos *et al.,* 2019). CQ however also possesses anti-inflammatory properties with radio sensitization and chemo sensitization activities. They have been applied for the treatment of various ailments such as lupus erythematosus, rheumatoid arthritis, etc. In 2020, various clinical trials and investigations commenced on the application of CQ for the treatment of COVID 19 (Obi-Ani *et al.,* 2020). The solitary trial by World Health Organization (WHO) was one of the biggest ongoing trial on the potency of CQ for COVID 19 treatment (Muhammed, 2020).

As is the case with other pharmaceuticals, the presence of CQ in the aquatic environment is already a reality. The chemical and biological properties of CQ have made them highly persistent with ability to bioaccumulate and thus contaminate all parts of the eco system (air, soil and water) (Lindroos *et al.,* 2019). Table 2.1 and Figure 2.2 outlines some properties and the structure of CQ. Due to the potentially persistent and bio accumulative

properties of CQ and its high volume production, it has been high recognized as an emerging pharmaceutical contaminant (Dabi, Babi & Skori, 2019). The potential for CQ to be incident in water is due to the presence the Nitrogen atom embedded in the cyclic quinoline ring. The derivatives of quinoline possess good solubility and low biodegradation which makes them a common contaminant in ground water and soil. Due to this high risk of contamination of natural waters, more attention needs to be given to limit the negative effects on the environment and human health (Howard & Muir, 2011).

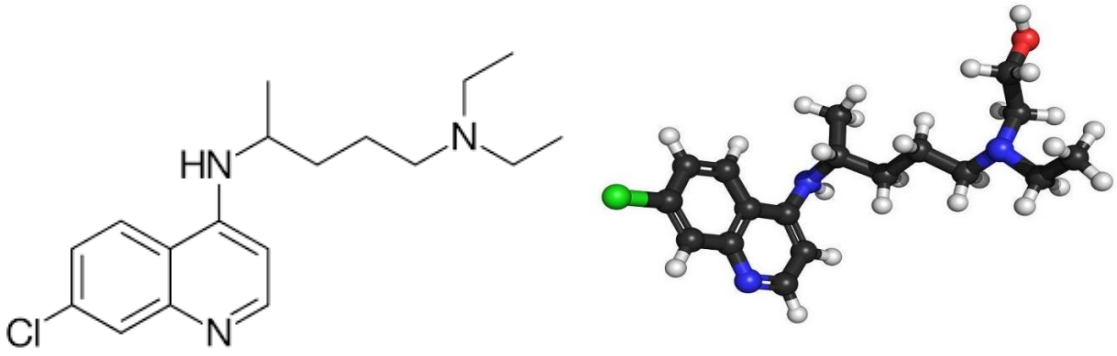

Figure 2.2: Structure and 3D structure of chloroquine (Schroeder & Gerber, 2014)

Table 2.1: Properties of Chloroquine (D'Alessandro *et al.*, 2020).

IUPAC name	(RS)-N'-(7-chloroquinolin-4-yl)-N,N-diethylpentane-1,4-diamine
Chemical formular	$C_{18}H_{26}ClN_3$
Class of drug	Antimalarial
Metabolism	Liver
Molar mass	319.872 g/mol
Half life	1-2 months
Pka	10.1

2.2 Toxicity of Dyes

Dyes find application in diverse industries such as paints, textile, printing, food, etc. leading to the production of over 10,000 varying dyes of about $7x10^5$ tons (Eltaweil,

Mohamed & El-monaem, 2020). Industrial effluents discharged into water bodies contain over 10-15 % containing dye pigments polluting and causing discoloration to aquatic environment (Wang & Ariyanto, 2007). Exposure to these pollutants leads to cancer, allergic reactions, skin irritation as they possess carcinogenic and mutagenic properties (Ayhan, 2008).

2.2.1 Malachite Green

Malachite green is a dark green basic, cationic dye used to impact color on various kinds of materials ranging from silk, wood, paper, cotton etc. MG has found application in farming and fisheries as an anti-microbial (Choudhary *et al.*, 2020). Its complex chemical structure (as shown in Figure 2.3) accounts for its high toxicity which makes degradation by microorganisms difficult. The presence of MG in water causes discoloration of the aquatic environment thereby reducing the rate of photosynthesis. The need to remove MG from dye effluents cannot be overemphasized as biological treatments are not suitable to removal of MG from wastewater (Ojediran *et al.*, 2020).

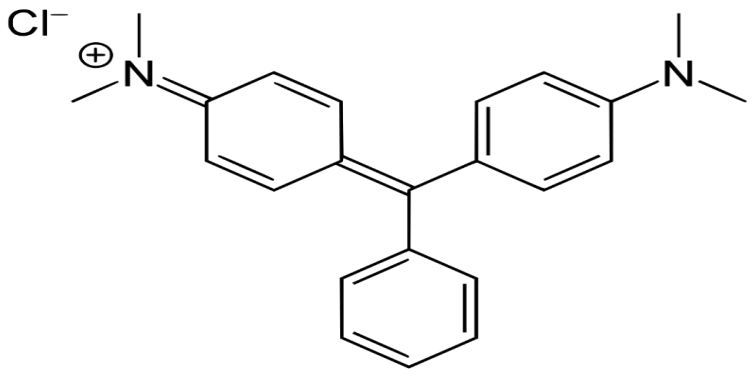

Figure 2.3:Structure of Malachite green (Muinde, Onyari, Wamalwa & Wabomba, 2020).

2.3 Agricultural Waste as Precursor Material for Adsorbents

Agricultural wastes are by products of agricultural practices which includes wood bark, sawdust, nuts, shells starch and cellulosic fibers of crops and plants. These wastes are often times discarded after harvesting or during the processing stage. They however possess high lignin, cellulose and carbon content, making them suitable for use as precursors in activated carbon production (Adegoke & Bello, 2015b). Most plant wastes are subjected to treatment

and modifications to enhance their adsorptive capacities, porosity and surface area. These resulting adsorbents are generally called bio-sorbents (Cruz *et al.,* 2020).

Recently, the conversion of agro-wastes to activated carbon, and the application of these activated carbon to remove pollutants from water has shown promising results (Anyanwu *et al.,* 2018). The interest of researchers to apply activated carbon for the uptake of pollutants could be due to the availability of agro-wastes and their potency to remove pollutants (Zhu, Li & Yang, 2018). Various agro-wastes have been applied for the sorption of pollutants from wastewater such as maize cob, cocoa pods (Adegoke & Bello, 2015b), rice hull (Tapia-Orozco *et al.,* 2016), sugarcane bagasse, coconut shells, coconut husk (Tursi, Chatzisymeon, Chidichimo, Beneduci & Chidichimo, 2018), banana peels (Leupin & Hug, 2005), orange and citrus peel (Afolabi, Popoola, & Bello, 2020). Agro-wastes are increasingly used as cost effective alternatives to expensive activated carbon for treating water (Tapia-Orozco *et al.,* 2016).

2.3.1 Rice Husk

Rice husk is the external coat protecting the rice grain usually obtained from threshing rice (Menya, Olupot, Storz, Lubwama, & Kiros, 2017). On a yearly basis, about 80 million tons of rice husk are produced and indiscriminately discharged around the world (Anyanwu *et al.,* 2018). They are made up of about 75-90 % lignin, hemicellulose and cellulose and other components include silica, water, trace elements (Shen & Fu, 2018). Several cereals have found application in the uptake of pollutants of waste water worldwide including rice, maize, wheat, oats, sorghum, etc. and these are cereals readily available around the world. Figure 2.4 shows the image of rice husk used in this research.

2.3.2 Plantain Peel

They are wastes which serve as a source of environmental pollution and thus a nuisance to the environment. They are readily available wastes in Nigeria and are often times disposed indiscriminately resulting in clogging of waterways and a source of unpleasant odours (Nworie *et al.,* 2018). Plantain peels have the potential to serve as good adsorbents. Figure 2.5 shows the image of plantain peels used in this research.

Figure 2.4: Rice Husk Used for this Research

Figure 2.5: Dried Plantain Peel Used for this Research

2.4 Adsorption process

This is a process whereby a substance attaches to the external surface of an adsorbent via chemical or physical bonds which is an efficient technique for treatment of wastewater (Mohammed, Al-Musawi, Kareem, Zarrabi, & Al-Ma'abreh, 2019). Various materials can be employed as adsorbents for the uptake of contaminants for waste water such as clay,

sand, zeolites, etc. The application of activated carbon (wide range of carbonized materials) for adsorption has attracted the interest of various researchers as a result of their high porosity, large surface area, low acid/base reactivity and thermostability.

Activated carbon has been widely employed for the separation, removal and modification of several compounds in gas and liquid phases. They can be made through wet or dry activation methods (Ahmad, Adilah, Ahmed, Adegoke, & Bello, 2020). The wet activation method involves the impregnation of either acid, bases or salts so as to improve the porosity, surface area and pore sizes of the material which aims at increasing its efficiency to adsorb contaminants. Wet acid activation with orthophosphoric acid is mostly applied at lower temperatures for lignocellulosic materials (Bello, Lasisi, Adigun, Ephraim, & Kalijadis, 2017). The use of Zinc Chloride is often avoided due to the environmental concerns raised although they produce activated carbons with higher surface area. For base activation, the application of potassium carbonate leads to activated carbon with better surface area than activated carbon using potassium hydroxide. Dry activation method involves the use of dry gas to improve the porosity and surface area of the carbon (Supong *et al.,* 2019).

2.5 Rice husk Activated Carbon for the Sorption of Different Pollutants.

Rice husk has been applied by various researchers for the adsorptive uptake of various contaminants from waste water. Adsorptive uptake of 2,4-dichlorophenol, by wheat husks biochar was investigated by (Kalderis, Kayan, Akay, Kulaksız, & Gözmen, 2017) and results showed 98.85 % removal. Similarly, Orimolade, Adekola, & Aminat (2018) evaluated the sequestration of bisphenol-A (BPA) from water using nano silica obtained from rice husk. The spectroscopic analyses revealed that the rice husk ash contains large fraction of amorphous silica. The adsorptive uptake of estrogen hormones (17β-estradiol and estrone) from water onto rice husk extracted silica was investigated by Zarghi, Roudbari, Jorfi, & Jaafarzadeh, (2019). Results showed the applicability and effectiveness of rice husk silica as an adsorbent for the uptake of these hormones.

Biocomposites were prepared by loading polyaniline (PANI), polypyrrole (PPY) and sodium alginate (NaAlg) onto barley husk (BH). These bio composites were applied to

sequester 2,4-dichlorophenol (2,4-DCP) from aqueous solution. The results reported by Bhatti *et al.,* (2020a) showed that the bio-composites have potential to remove 2, 4- DCP from industrial effluents In a similar study, the potency of modified rice husk to sequester Direct Red-31 (DR-31), Direct Orange-26 (DO-26), Ever direct Orange-3GL (EDO-3) and Direct Blue-67 (DB-67) dyes from aqueous media was investigated by (Bhatti *et al.,* 2020b). Results obtained revealed that the modified rice husk possessed high adsorptive capacity for uptake of the dyes.

2.6 Plantain Peel Activated Carbon for The Sorption of Different Pollutants

Plantain peel has found application in sorption of a wide range of pollutants ranging from dyes to pharmaceuticals. Removal of 3,7-Bis (dimethylamino)-phenothiazin-5-ium chloride and lead (II) was investigated by Sudhakar *et al.,* (2015) using unripe plantain peels. Sorption using this adsorbent was found to be feasible, favourable and endothermic. The uptake of Chromium present in battery recycling effluent by plantain wastes was studied by Adeolu & Dada, (2016) and the report established that the activated carbon derived from treatment of plantain peel had the highest sorption capacity.

Similarly, fresh and dehydrated banana peels were however used by Zhou *et al.,* (2017) as biomass feedstock to produce highly effective sorbent activated carbon. The results revealed the broad surface area and high porosity of the plantain peel made them effective adsorbents. Similar results were also obtained by Adekola, Ayodele, & Inyinbor (2019) who investigated the potency of plantain peel activated biochar to remediate Rhodamine B (RhB) dye contaminated media. 54.78 % removal efficiency of RhB dye was observed with optimum adsorption of 84.41 mg/g at 120 minutes.

The biosorption of Zinc (II) ions by plantain peel biomass was investigated by Nworie *et al.,* (2018) and results revealed the potential of Zn (II) ions to be remediated by plantain peel. Banana peels modified as a magnetic biochar was applied by Rong *et al.,* (2019) for the uptake of organic contaminants. Results showed that separation was easy with high catalytic behaviors enhanced by the Iron oxide nanoparticles.

2.7 Adsorption of Dyes and Pharmaceuticals using Agro-wastes

The application of modified agrowastes have been reported severally for the uptake of dyes and pharmaceuticals from waste water. Table 2.2 outlines some reported agrowastes used for the uptake of dyes and pharmaceuticals

Table 2.2: Modified agro-wastes used for the adsorption of various pharmaceuticals and dyes.

Class of Pollutant	**Name**	**Adsorbent**	**Reference**
Pharmaceuticals	Ciprofloxacin	Banana Stalk	Agboola & Bello (2020)
		Rice husk biochar	Nguyen, Phuong, & Van (2020)
	Ibuprofen	Kolanut husk	Bello *et al.,* (2021)
	Diclofenac	Peanut shell	Onaga *et al.,* (2021)
	Lumefanthrine	Banana Stalk	Agboola, Akanji, & Bello, (2021)
	Enrofloxacin	Rice husk biochar	Nguyen *et al.,* (2020)
Dyes	Malachite green	Zea Mays	Ojediran *et al.,* (2020)
	Rhodamine B		Inyinbor *et al.,* (2016)
			Dada *et al.,* (2019)
			Bello *et al.,* (2019)
			Bello *et al.,* (2017)
	Crystal violet	*Millettia thonningii* seed pods	Jasper, Ajibola, & Onwuka, (2020)
	Reactive orange	Empty cotton flower	Charola, Yadav, Das, & Maiti, (2018)
	Brilliant green dye	Areca nut husk	Sukla Baidya & Kumar, (2021)

2.8 Nanoparticles and Nanocomposites

Nanotechnology is a field of study that deals with nano particles less than 100 nm (Sridhar, Ramanane & Rajasimman, 2018). They find application in various scientific disciplines and innovations in optics, material and biomedical sciences, electronics, etc. Nanoparticles are modified forms of basic elements possessing special properties in addition to their small size which gives them an edge over other materials and allow them a wide range of application in preference to their bulk counterparts. They generally possess high surface area, speed of sorption when compared to other bio sorbents. Table 2.3 outlines the properties of some nanoparticles. They could be organic or inorganic in nature. Current trends as applied by researchers in nanoscience is the impregnation and loading of nanoparticles onto adsorbents to produce nanocomposites with improved efficiency for effective sequestration of pollutants (Dada *et al.*, 2017). Some of these nanocomposites have been reported to possess antibacterial properties and high bacteria resistance. (Ghani, Yusoff, & Andas, 2015).

Zinc Oxide nanoparticles and nanocomposites have been explored for the uptake of various pharmaceuticals as well as other pollutants and results have shown that they are effective adsorbents for the sorption of pharmaceuticals (Choina *et al.*, 2015; Deb, Kanmani, Debnath, Bhowmik, & Saha, 2019; Zhang *et al.*, 2013). Zinc Oxide nanoparticle is non-toxic, easy to manufacture and changes in environmental conditions does not affect its structure (Sridhar *et al.*, 2018). The wide band gap of 3.2eV, isoelectric point of 9.5 and large excitation binding energy of 60 MeV has made ZnO a nanoparticle of interest amongst researchers thereby making the loading of ZnO nanoparticles onto base adsorbents an area of interest in recent years. Mohammed *et al.*, (2019) investigated the uptake of antibiotics using pistachio shell powder loaded with ZnO nanoparticles and results showed that loading ZnO onto the base material improved its adsorption efficiency by increasing the surface area.

Table 2.3: Properties of Nanoparticles

Nanoparticles (NPs)	**Properties**	**Reference**
TiO_2 NPs	Antibacterial material, photo catalyst.	Masoudian *et al.*, (2019)
Ag NPs	Antimicrobial agents	Akter *et al.,* (2018)
Zinc Oxide NPs	optical, physical, and antimicrobial properties	Pour, Rangkooy, Jahani, & Golbaghi, (2019)
Silica NPs	low toxicity, large surface area to volume ratio, , high chemical and physical stability.	Karnati, Agbo, & Zhang, (2020)
Gold NPs	Unreactive in bulk form and therefore considered as non-toxic.	Adewale, Davids, Cairncross, & Roux, (2019)
Iron NPs	Small size, high surface area and magnetic property.	Ali, Alharbi, Alothman, & Alwarthan, (2018)

2.9 Nanoparticles and Nanocomposites for the Sorption of pollutants

Nanoparticles and their activated carbon-based nanocomposites have been employed and their effectiveness reported for the uptake of pollutants from aqueous media. In recent times, research interests have been geared towards the uptake of pollutants by activated carbon-based nanocomposites. This modified adsorbent does not just improve the properties of activated carbon but combines it's advantages with the properties of nanoparticles leading to composites possessing high porosity, improved functional groups, more active sites for adsorption, etc. therefore, these composites can be applied for the adsorptive uptake of various pollutants (Saucier *et al.,* 2017) including heavy metals, organic contaminants, and other inorganic contaminants (Qiu, Qin, Xu, Kang, & Hu, 2019).

In a study reported in 2019, organic pollutants were adsorbed by nanocomposites with catalytic and oxidative/reductive degradation (Qiu *et al.,* 2019). The adsorbent possessed excellent qualities as they combined the advantages of activated carbon and nanoparticles to promote its performance (Dasgupta, Ranjan, & Chidambaram, 2017).

Cruz *et al.,* (2020) incorporated ZnO onto modified corn cob and coffee husk biochar and the resulting composite was applied for the uptake of As(V) and Pb(II). The impregnated ZnO increased the adsorptive capacity and efficiency of the adsorbent thereby increasing the rate of adsorption of As(V) and Pb(II). In a similar study, the ability of *Nigella sativa* seed-based nanocomposite, MnO_2/BC to sequester Methylene Blue dye was monitored by (Siddiqui, Manzoor, & Chaudhry, 2018) and results showed high adsorptive capacity of the adsorbent.

According to Zeng & Xue (2019) , the loading of crayfish shell activated carbon with Ag and TiO_2 nanoparticles produced nanocomposites that was effective for the uptake of pollutants from water with strong antibacterial properties. Results showed that the novel nanocomposites could be applied for household purifiers and treatments units. Similarly, the sol gel method was applied by Zhang & Lu (2018) who loaded titanium dioxide (TiO_2) nanocomposites onto coconut shell activated carbon for the remediation of dye waste water. Results showed that the nanocomposite was highly applicable for treatment of effluent from dye industries. A cellulose acetate-based nanocomposite was synthesized for the uptake of organic pollutants. The degradation (photocatalytic) of methylene blue dye via solar light was also monitored (Gupta, Pathania, Singh, Kumar, & Rathore, 2014).

CHAPTER THREE

MATERIALS AND METHODS

3.1 Materials

3.1.1 Raw materials

The raw materials used in this study are Rice Husk (RH), and Plantain Peel (PP),

3.1.2 Reagents

Reagents purchased and utilized were of analytical grade. Orthophosphoric acid (H_3PO_4) (supplied by BDH chemicals CAS:7664-38-2), Ammonium Carbonate (NH_4CO_3) (Sigma Aldrich CAS:506-87-6), Zinc Nitrate (Zn $(NO_3)_2$, (LOBA Chemie CAS: 10196-18-16), distilled water, Chloroquine (Sigma Aldrich CAS:747-36-4), Malachite green, Sodium hydroxide (NaOH) (Carlo Erba CAS: 1310-73-2).

3.1.3 Glassware /apparatus

Magnetic stirrer (Bante MS300), crucible, centrifuge (SIGMA 4-5L), desiccator, evaporating dish, sieve, oven (GENLAB N30C), pH meter (Hanna HI 2210), furnace (Searchtech SX-5-12), thermostat shaker model SI-300R (Lab Companion®), UV/Vis spectrophotometer model M51 (Bel Engineering®).

3.2 Methods

3.2.1 Raw Materials Collection

Rice husk was collected from the Landmark University research farm, Omu-Aran, Kwara State, while the plantain peel was collected from a Landmark University kitchen.

3.2.2 Material Preparation/Carbonization

Rice husk and Plantain peel were screened and thoroughly washed to remove impurities and dust using distilled water. The rice husk was then oven dried for 3 h at 110 ^{0}C, treated

with Nitric acid to remove metallic impurities, rinsed and dried, then treated with NaOH to remove silica content and a brick red colored RH was obtained (Dada, Ojediran, & Olalekan, 2013). Similarly, after washing the plantain peels were allowed to air dry, then oven dried for about 8 h at 105 ^{o}C after which it was grinded and labelled PP. Both samples carbonized at 400 ^{o}C for 1 h (Ekpete, Marcus, & Osi, 2017).

3.2.3 Chemical activation of Rice Husk/Plantain Peel using H_3PO_4

50.0 g of the treated RH and PP was weighed and placed in a beaker. 1000 mL of 1 M H_3P0_4 was added and the beaker content was heated till a paste was formed. It was then transferred to a furnace at 400 ^{o}C for 1 h. The activated carbon was then left to cool and using distilled water, it was thoroughly rinsed to obtain a pH at the neutral region. The resulting activated carbon was oven dried and stored in an airtight container. It was then oven dried, packed and labelled as RHAC and PPAC respectively (Dada *et al.*, 2013).

3.2.4 ZnO Nano-Composites Synthesis

RHAC and PPAC was weighed (1.0 g) into a beaker already containing 100 mL Zinc Nitrate solution (0.45 M). 100 mL of 1.0 M NaOH was slowly introduced with constant stirring at 70 ^{o}C afterwards, it was centrifuged at 4,000 rpm for 30 mins. Then rinsed with distilled water, followed by ethanol and finally calcinated at 350 ^{o}C for 4 h. The samples were allowed to cool and placed in an airtight container then labelled RHAC-ZnO and PPAC-ZnO (Vinayagam, Ramachandran, Ramya, & Sivasamy, 2017)

3.3 Adsorbent Characterization

3.3.1 Determination of pH

The method as described by Bello *et al.*, (2017) was employed for the determination of the pH value of the adsorbent. 1.0 g of the adsorbent was weighed and placed into a beaker followed by the addition of 100 mL of distilled water. This was left to boil for a period of 5 min. Additional 100 mL distilled water was introduced and the solution was left to cool. A pH meter was then used to check the pH value.

3.3.2 Moisture Content

This was calculated using the method reported by Adeolu *et al,* (2016). The empty crucible was weighed and 1.0 g of the adsorbents was weighed into it after which it was placed in an oven and heated for 5 h in an oven. The samples were placed in a desiccator and left to cool, then reweighed. The percentage moisture in each sample was obtained by calculating the difference between the final and initial mass of carbon. The percentage moisture was then calculated using the equation below:

$$\text{Moisture \%} = \frac{loss\ of\ weight\ on\ drying\ (g)}{initial\ weight\ (g)} \text{ x } 100 \qquad (3.1)$$

3.3.3 Ash Content

The ash content of each sample was obtained using the method reported by Ekpete *et al.*, (2017). The crucibles were first preheated and weighed. 1.0 g of the sample added into the crucibles and weighed again. After weighing, it was transferred to the furnace and allowed to heat at 500 ^{o}C for about 1 h 30 min. it was placed in a desiccator for cooling and the final weight was measured. Equation 3.2 was used to calculate the % Ash content

$$\text{Ash \%} = \frac{ash\ weight}{oven\ dry\ weight} \text{ x } 100 \qquad (3.2)$$

3.3.4 Volatile Matter

The volatile matter determination was carried out by weighing the empty crucible, then placing 1.0 g of the sample into the crucible which was then re-weighed. The samples were heated at 500 ^{o}C for 10 min in a furnace. Calculations of the % volatile matter was carried out by applying Equation 3.3.

$$\text{Volatile \%} = \frac{weight\ of\ volatile\ component}{oven\ dry\ weight} \text{ x } 100 \qquad (3.3)$$

Where, volatile weight is the weight difference of samples before and after heating (Nworie *et al.,* 2018**).**

3.3.5 Bulk density

To determine the Bulk density, the method reported by Ekpete *et al,* (2017) was adopted in which a 10 mL measuring cylinder was weighed after and before it was packed with water. The sample was then packed into the measuring cylinder, tapped 2-3 times and then re-weighed. The weight difference and bulk density was determined with Equation 3.4.

$$\text{Bulk density} = \frac{w_2 - w_1}{v} \quad (3.4)$$

Where;

W_2= Weight of cylinder loaded with sample,

W_1= Weight of empty measuring cylinder

V = Volume of cylinder

3.3.6 Simple Specific Surface Area Via Saer's method

The adsorbent surface area was determined by applying sear's method which followed the following procedure. Adsorbent weight of 0.5 g was placed in a beaker and its pH was raised to values between 3-3.5 using 0.1 M HCl. After which, 1g of NaCl and distilled water (50 mL) was added. Titration was done with 0.1 M NaOH in cause a pH rise from 4 and then raised to 9 (Dada *et al,* 2013). The volume required to raise the pH was recorded and Equation 3.5 was used to calculate the surface area.

$$S\left(\frac{m^2}{g}\right) = 32v - 25 \quad (3.5)$$

3.3.7 Point of Zero-charge (pH_{pzc})

The pH_{pzc} was obtained by measuring 0.1 M NaCl (50 mL) into a beaker, then 0.1g of adsorbent was added to it. The initial pH was measured and varied from 2 to 12 using NaOH or HCl. After which it was sealed and shaken for 24 h. the final pH was then determined and a plot of the value difference between the initial and final pH, ($pH_f - pH_i$) versus the initial pH was plotted. The pH_{pzc} was recorded as the point where the initial pH minus the final pH equals Zero (Agboola & Bello, 2020).

3.3.8 Iodine Number

Method described by Bello *et al.,* (2017) was adopted for the iodine number test. A 1000 mL stock solution comprising of 2.7 g iodine pellets and 4.1 g KI (Potassium Iodide) was prepared. This was standardized using sodium thiosulphate (standard solution). 10 mL of 5 % HCl and 0.5 g adsorbent was placed in a flask and stirred so as to wet all the carbon. 100 mL of the prepared stock iodine solution was placed on the shaker for 60 min after which it was filtered. 0.1 M sodium thiosulphate was placed in a burette and titrated with 20 mL of the filtered adsorbent solution. The percentage iodine adsorbed was calculated using Equation 3.6

$$\% \text{ iodine} = \frac{(mL\ of\ Na_2S_2O_3\ in\ blank) - (mL\ of\ Na_2S_2O_3\ in\ sample)}{(mL\ of\ Na_2S_2O_3\ in\ blank)} \quad (3.6)$$

The iodine value was calculated using the formular as described in the literature (Zheng, Zhao, & Ye, 2014).

$$\text{Iodine value (IV)} = \frac{5\ x\ (10_{C_1} - 1.2_{C_2V_2})x\ 127}{m}\ x\ D \quad (3.7)$$

where C_2 and C_1 (mol/L) stands for the concentration of sodium thiosulfate and stock iodine solution respectively. M is the adsorbent mass, V_2 (mL) stands for the volume of sodium thiosulphate while D is the correction coefficient.

The surface area calculated from the iodine number (S_{BET}) was further calculated using the Equation 3.8 (Abdullah, Abdullah, Amin, & Zainol, 2018);

$$S_{BET} = \text{IV x } 0.986 \quad (3.8)$$

3.3.9 Boehm Titration

This method was applied to ascertain the oxygen containing functional groups on the adsorbents. The procedure reported by Bello *et al,* (2017) was adopted for this analysis. Adsorbent was weighed (1.0 g) and placed in a beaker containing 15 mL of solutions NaOH (0.1 M), Na_2CO_3 (0.5 M) and $NaHCO_3$ (0.1 M) to ascertain groups that are acidic.

However, for groups that are basic, 0.1 M HCl solution was used and at ambient temperature for 48 h they were placed on a shaker. The solution was titrated with NaOH (0.1 M) to determine groups that are basic, and HCl (0.1 M) for groups that are acidic. The number of oxygen-containing functional groups was evaluated using the Equation 3.9-3.10).

$$F_x = \frac{V_{bx} - V_{ex}}{Mx} \; X \; M_t \; X \; D_F \tag{3.9}$$

$$D_F = \frac{initial\ volume}{selected\ volume\ for\ titration} \tag{3.10}$$

Where V_{bx} stands for the titrant volume used for blank titration, D_F represents the dilution factor, F_x (mmolg^{-1}) stands for the amount of oxygen containing functional groups, M_t is the molarity of the titrant used, V_{ex} stands for the titrant volume used to titrate the extract (Bello *et al.,* 2017).

3.3.10 Scanning Electron Microscopy (SEM)

This analysis gives a pictorial view and surface morphology of the adsorbents. The SEM contain detectors that produce a three-dimensional image of the surface of the adsorbents surface. SEM works on the principle based on the bombarding of electron beams on the analyzed samples which in turn re-emits certain particles (Deb *et al.*, 2019).

3.3.11 Fourier Transform Infrared (FTIR) Analysis

This analysis was carried out on all adsorbents to identify all possible functional groups present on them (Ding, Cheng, Sun, & Wang, 2015).

3.3.12 X-ray Diffraction (XRD) Analysis.

The crystallinity, nature and mineral constituents of RHAC-ZnO and PPAC-ZnO nanocomposites was investigated using the X-ray Diffractometer.

3.4 Adsorption Experiment

3.4.1 Preparation of Adsorbates

Adsorbates stock solutions (CQ and MG) were prepared by adding 1.0 g of adsorbate into 1000 mL of distilled water. Working standards from 10-50 ppm were prepared by appropriate dilution.

3.4.2 Batch Adsorption

For the adsorption studies, adsorbent weight of 1.0 g was introduced into 100 mL of the adsorbate which was then subjected to shaking using a mechanical shaker at varying time intervals. The residual concentrations were obtained using a UV spectrophotometer. The Equation 3.11 was used for the calculation of quantity of adsorbate adsorbed.

$$Qe = \frac{(C_o - C_e)\,V}{m} \tag{3.11}$$

where C_e and C_o represent the initial concentration (mg/L) and equilibrium concentration (mg/L) respectively of adsorbate; V represents the volume of the solution (L); m represents the adsorbents mass (mg) and Q_e stands for the adsorption capacity (mg/g) of the adsorbent. For the removal efficiency of adsorbents, Equation 3.12 was used.

$$Removal\ (\%) = \frac{C_o - C}{C_o} \text{ x } 100 \tag{3.12}$$

where C_o and C stands for the initial and final adsorbate concentration (mg/L) after the adsorption.

3.4.2.1 Effects of pH

The effects of varying the initial pH on the adsorptive capacity of each adsorbent was monitored at pH values from 3, 5, 7, 9 and 11. These pH values were adjusted using 0.1 M HCl and NaOH

3.4.2.2 Effects of Contact time

The influence of time of contact between adsorbate and adsorbent was varied and monitored at 10, 20, 30, 60, 90, 120 and 240 minutes. The change in residual adsorbate at various time intervals was observed and recorded via a UV-vis spectrophotometer until

equilibrium was reached. A shorter contact time to reach equilibrium implies a faster rate at which adsorbate molecules leave the bulk and gets to the inner and outer surface of the adsorbents. It is thus a very important factor in the transfer process (Sudhakar & Soni, 2018).

3.4.2.3 Effects of Temperature

The influence of various temperatures at 30, 40 and 50 ^{o}C on the adsorption capacity of adsorbents (RHAC, PPAC, RHAC-ZnO-NC and PPAC-ZnO-NC) was observed. This adsorption parameter is important as increase in temperature generally increases sites for adsorption and decreases the boundary layer thickness surrounding the adsorbent (Sartape *et al.,* 2017).

3.4.2.4 Effects of Initial Concentration

The initial concentration is vital as it provides the driving force needed to overcome resistance of the adsorbate-adsorbent boundary due to mass transfer. The effects various inital concentration of 10, 20, 30, 40 and 50 ppm of adsorbates (MG And CQ) on their uptake using the adsorbents was monitored.(Gündüz & Bayrak, 2017).

3.5 Isotherm Models

Isotherm models describe the nature with which adsorbates and adsorbents react during the sorption process. In this research the adsorption data was subjected to four isotherm models to determine which model best describes the uptake. The Freundlich, Langmuir, Temkin and Dubinin Radushkelvich isotherm models were used (Ahmad *et al.,* 2020).

3.5.1 Langmuir Isotherm

The Langmuir isotherm assumes that there is a rapid decrease of intermolecular forces as distance increases. This isotherm predicts that the nature of coverage of the adsorbate on the adsorbent surface is monolayer, which implies that the layer adsorbed has a thickness of 1 mole (Dada *et al.,* 2013). When an adsorption data fits the Langmuir isotherm, it implies that chemisorption occurred on the adsorption sites with similar adsorption

energies (Dada *et al.*, 2016; Arampatzidou & Deliyanni, 2016). Equation 3.13 shows the Langmuir isotherm equation.

$$\frac{C_e}{q_e} = \frac{1}{q_{mK_L}} + \frac{1}{q_m} C_e \quad (3.13)$$

q_e represents the amount of adsorbed adsorbate per unit mass of adsorbent (mg/g), C_e is the adsorbates equilibrium concentration (mg/L), C_o represents the adsorbate initial concentration (mg/L), b stands for the Langmuir adsorption constant (L/mg) while q_m stands for the adsorption capacity (monolayer) in mg/g of the adsorbent, a plot of C_e/q_e versus C_e will give a straight line having $1/q_m$ as the slope and $1/K_L q_m$. as the intercept. A very important data parameter in the Langmuir isotherm is the R_L (separation factor) as shown in equation 3.14 is a dimensionless separation factor. An R_L value of less than 1 shows the favourability of the sorption process.

$$R_L = \frac{1}{1 + K_L C_o} \quad (3.14)$$

where; K_L stands for the adsorption constant (Langmuir)(L/mg) while C_0 stands for the highest initial solute concentration (mg/L).

3.5.2 Freundlich Isotherm

This isotherm model usually refers to multilayer adsorption, and it assumes a heterogenous adsorption as a result of differences of sorption sites (Dada *et al.*, 2017). Hence, this model is not restricted to monolayer formation (Foo & Hameed, 2010; Bouhamed *et al.*, 2012). The model however indicates physisorption on the adsorbent surface (Arampatzidou & Deliyanni, 2016). It can be expressed as

$$q_e = Kf \ \mathrm{Ce}^{1/n} \quad (3.15)$$

which can then be further rearranged to give:

$$\mathrm{Log}\ q_e = \frac{1}{n} \log Ce + \log Kf \quad (3.16)$$

q_e stands for the amount of adsorbed adsorbate per unit mass of adsorbent (mg/g), C_e represents the concentration in mg/L of adsorbate at equilibrium, whereas, K_f and n are constants (Freundlich) affiliated to the adsorption capacity and adsorption intensity respectively.1/n stands for the adsorption intensity. Plotting a graph of log q_e vs. log C_e generates a graph having 1/n as slope and log K_f. as intercept. A positive n value greater than 1 suggests that the favourability of the process (Mudyawabikwa, Mungondori, Tichagwa, & Katwire, 2017).

3.5.3 Temkin Isotherm

This model explicitly considers adsorbent–adsorbate interactions and does not consider the extremely low and extremely large concentration values. The model assumes that heat of adsorption (function of temperature) of all molecules, instead of decreasing logarithmic, will decrease linearly with coverage (Foo & Hameed, 2010).
The mathematical expression to describe the Temkin model is written as:

$$q_e = B \ln (K_T C_e) \quad (3.17)$$

Further rearrangement gives,

$$q_e = B \ln K_T + B \ln C_e \quad (3.18)$$

*w*ith, K_T standing for the equilibrium binding constant (L/mg), q_e represents the adsorbed adsorbate at equilibrium (mg/g), (B = RT/b) and this is a constant affiliated to the heat capacity (L/mg), T represents the absolute temperature (K), R is the Universal gas constant (8.314 J/mol K), C_e is the equilibrium concentration of adsorbate (mg/L).

3.5.4 Dubinin-Radushkevich isotherm

The D–R isotherm is generally applied to express the adsorption mechanism with a Gaussian energy distribution onto a heterogeneous surface (Dada *et al.*, 2018). It is used to differentiate the physisorption and chemisorption for the removal of a molecule from its location in the adsorption space to an infinite point (Foo & Hameed, 2010).
Equation 3.19 expresses the D-R model

$$q_e = q_m \exp(-B\,\varepsilon^2) \quad (3.19)$$

where,

$$\varepsilon = RT \ln\left[1 + \frac{1}{Ce}\right] \quad (3.20)$$

where: *B* stands for a constant affiliated with D-R, q_e represents the quantity of adsorbed adsorbate at equilibrium, *T* stands for the absolute solution temperature, *R* represents the universal gas constant, q_m stands for the maximum adsorption capacity while C_e stands for the adsorbate equilibrium concentration. A plot of ln q_e vs ε^2 produces a linear graph with ln q_m as intercept and B as slope. The value of E (free energy of adsorption) can be calculated from the value of the slope as seen in Equation 3.21

$$E = \frac{1}{\sqrt{2B}} \quad (3.21)$$

The nature of adsorption can also be evaluated via the E value. The adsorption is termed physical if the value of E falls between 1-8 KJ/mol hence, physisorption and termed chemical adsorption (chemisorption) if E values ranges between 9 -16 KJ/mol.

3.6 Adsorption Kinetics

Adsorption data was subjected to four Kinetic models (Pseudo Second Order. Pseudo First Order, Elovich and Intraparticle diffusion models). Kinetic studies provide valuable details on the reaction pathway and their mechanism. It describes the dependence of the rate of adsorption on adsorbate concentration solution besides determining the influence of adsorption rate on the adsorption capacity.

3.*6.*1 Pseudo-First Order Kinetics

This kinetic model was a part of the foremost equations used to explain the adsorption rate with respect to adsorption capacity. This model assumes the change of adsorption of solute per unit time is proportional to the amount of solid uptake with time and the difference in saturation concentration (Dada *et al.*, 2020). It is generally expressed as:

$$\ln(q_e - q_t) = \ln q_e - k_1 t \quad (3.22)$$

The linear plot of ln ($q_e - q_t$) vs. t. provides the parameters q_e and k_1 which can be obtained from the intercept and slope of the plot (Bello *et al.,* 2019)

3.*6*.2 Pseudo-Second Order Kinetics (PSO)

This kinetic model predicts the adsorption behaviour of an adsorption process over the entire range studied. It is used to predict the behavior of an adsorption process over the entire range studied (Dada *et al.,* 2019). It can be expressed as:

$$\frac{t}{qt} = \frac{1}{K2qe2} + \frac{1}{qe}t \qquad (3.23)$$

Plotting t/q_t versus t produces a linear graph where k_2 and q_e can be estimated from the intercept and slope of the plot.

3.*6*.3 Elovich Kinetic Model

The Elovich model suitably explains the kinetics of adsorption of heterogeneous adsorbents although, this model does not predict any definite mechanism (Dada *et al.,* 2016). The Elovich model is expressed as:

$$qt = \frac{1}{\beta}\ln(\alpha\beta) + \frac{1}{\beta}\ln t \qquad (3.24)$$

where: β represents the surface coverage extent and chemisorption energy of activation in g/mg, α stands for initial sorption rate (initial) in mg/g min. The values α and β can be calculated from the slope and intercept obtained by plotting a graph of qt vs ln t.

3.*6*.4 Intraparticle Diffusion (IPD) Model

The adsorption process includes the migration of adsorbate from the bulk to the external surface of adsorbents, sorption on the sites' surface and intraparticle diffusion of adsorbate molecules. The slowest of these steps is the rate-determining step (the step controlling the overall rate of the adsorption process). In the IPD model, the adsorbate uptake varies nearly proportional to $t^{1/2}$ (Ojediran *et al.,* 2020). It can be expressed as:

$$q_t = K_{diff}\ t^{1/2} + C \qquad (3.25)$$

where: k_{diff} represents the rate constant of IPD (mg/g min), q_t represents the amount of adsorbed adsorbate at time *t*, *C* stands for the intercept. A plot of q_t versus $t^{1/2}$ will produce a linear graph with intercept of *C* which describes the boundary layer effect and a slope the k_{diff}. The rate determining step largely depends on the input of surface sorption which in turn depends on the C value obtained. On plotting q_t against $t^{1/2}$, if the linear graph passes through the origin, then only the IPD model can be said to be the rate-controlling step, otherwise, other mechanisms may be involved alongside the intraparticle diffusion model (Dada *et al.,* 2017; Lazim, Hadibarata, Yusop & Nazifa, 2021).

3.7 Thermodynamics Models

Thermodynamic studies are carried out in order to study the nature, feasibility and spontaneity of the sorption process. The monitored parameter in thermodynamic studies disclose the various energy changes that occurred during the sorption process. Hence, three parameters are assessed which are the Standard free energy change (ΔG^o), Standard change in enthalpy (ΔH^o), and Standard change in entropy (ΔS^o) (Dada *et al.,* 2020).
Thermodynamic parameters can be evaluated using the equation:

$$\ln K_L = \frac{\Delta S}{R} - \frac{\Delta H}{RT} \tag{3.26}$$

where: ΔS^o stands for the change in standard entropy (kJ/mol K), K_L represents the Langmuir adsorption constant (L/mg), *R* represents the Universal gas constant (8.314 J/mol K), whereas *T* is the absolute solution temperature (K), ΔH^o is the change in standard enthalpy (kJ/mol K). On plotting ln K_L versus 1/*T*, the straight-line equation produced is used to calculate values of ΔS^o and ΔH^o from the graphs' intercept and slope. Positive ΔS^o values suggest increased randomness or disorderliness at the adsorbent-adsorbate interface in the sorption process besides shows adsorbent affinity toward the adsorbate. Positive ΔH^o values suggests that the adsorption process is endothermic and exothermic when negative ΔH^o values are obtained (Dada *et al.,* 2014). Furthermore, a negative ΔG^o value signifies

spontaneity of the adsorption process at the studied temperature. Free energy change can be evaluated using the equation:

$$\Delta G^o = -RT \ln K_l \quad (3.27)$$

The activation energy E_a, is used to determine the nature of the process using the Arrhenius equation. When the activation energy value ranges between 5 and 40 KJ/mol, physisorption process is said to have taken place and at higher values of E_a, between 40 to 800 KJ/ mol, the adsorption is said to be by chemisorption (Dada *et al.,* 2017). The mathematical expression of the Arrhenius equation is given by:

$$\ln k_2 = \ln A - \frac{Ea}{RT} \quad (3.28)$$

where: the absolute temperature is represented as *T* (K), Arrhenius energy activation as E_a for adsorption (kJ/mol), K_2 is the PSO kinetic model rate constant (g/mg min). Arrhenius factor is depicted by A, and the universal gas constant as *R* (8.314 J/mol K), On plotting ln K_2 versus 1/*T*, a straight-line graph is produced and the E_a value can be calculated from the slope of the graph.

3.8 Statistical Validity Models

In order to prove the validity of the isotherm models, the Sum of Square Error (SSE) and Chi-square (χ^2) validity models were applied. Validity of isotherm and kinetic models is important as the regression coefficient (R^2) alone may not be a good judge of which model will best describe the rate determining step and mechanism (Adegoke and Bello, 2015b). Equations 3.29 and 3.30 describe the statistical validity models applied.

$$X^2 = \sum_{i-1} \frac{(q_{e(\exp)} - q_{e(cal)})^2}{q_{e(cal)}} \quad (3.29)$$

$$SSE = \sum_{i=1}^{n} (q_{e(cal)} - q_{e(\exp)})^2 \quad (3.30)$$

CHAPTER FOUR

4.0 RESULTS AND DISCUSSION

4.1 Characterization of Adsorbents

Presented in Table 4.1 are the physicochemical properties of RHAC, RHAC-ZnO-NC, PPAC and PPAC-ZnO-NC. Physicochemical characterization carried out includes the bulk Density, pH, pH_{pzc}, percentage moisture content and ash content, Boehm titration and iodine number determination

Table 4.1: Physicochemical parameters of Adsorbents

Property	**Adsorbents**			
	RH-AC	RHAC-ZnO-NC	PP-AC	PPAC-ZnO-NC
pH	6.83	6.53	6.72	7.21
% Moisture content	8.45	7.32	9.21	7.54
% Ash content	18.45	16.23	14.21	12.18
% Volatile matter	32.31	30.42	35.64	31.48
Bulk density	0.481	0.88	0.37	0.65
pH_{pzc}	6.21	5.10	4.98	4.99
Surface area (Sears method)	195.8	256.6	199.0	205.2

The pH values of RHAC, PPAC, RHAC-ZnO, and PPAC-ZnO were found to be 6.83, 6.72, 6.53 and 7.21 respectively, which is within the range of acceptable limits. It has been reported that for most applications, carbon pH of 6–8 is acceptable (Dada *et al.*, 2013 ; Ekpete *et al.*, 2017). The point of zero charge (pH_{pzc}) which is the pH value at which the adsorbents possess a net neutral charge (null charge) on the surface was also determined using the salt addition method. Adsorbents have a negative charge at higher pH values than the pH_{pzc} and as such effective to adsorb cationic pollutants while adsorbents have a

positive charge at pH values less than pH_{pzc} and can adsorb anionic pollutants (Agboola, Akanji, & Bello, 2021; Mudyawabikwa, Mungondori, Tichagwa, & Katwire, 2017). The pH_{pzc} for RHAC, PPAC, RHAC-ZnO-NC, and PPAC- ZnO-NC were found to be 6.81, 6.73, 6.62, 7.03 respectively as shown in Figure 4.1.

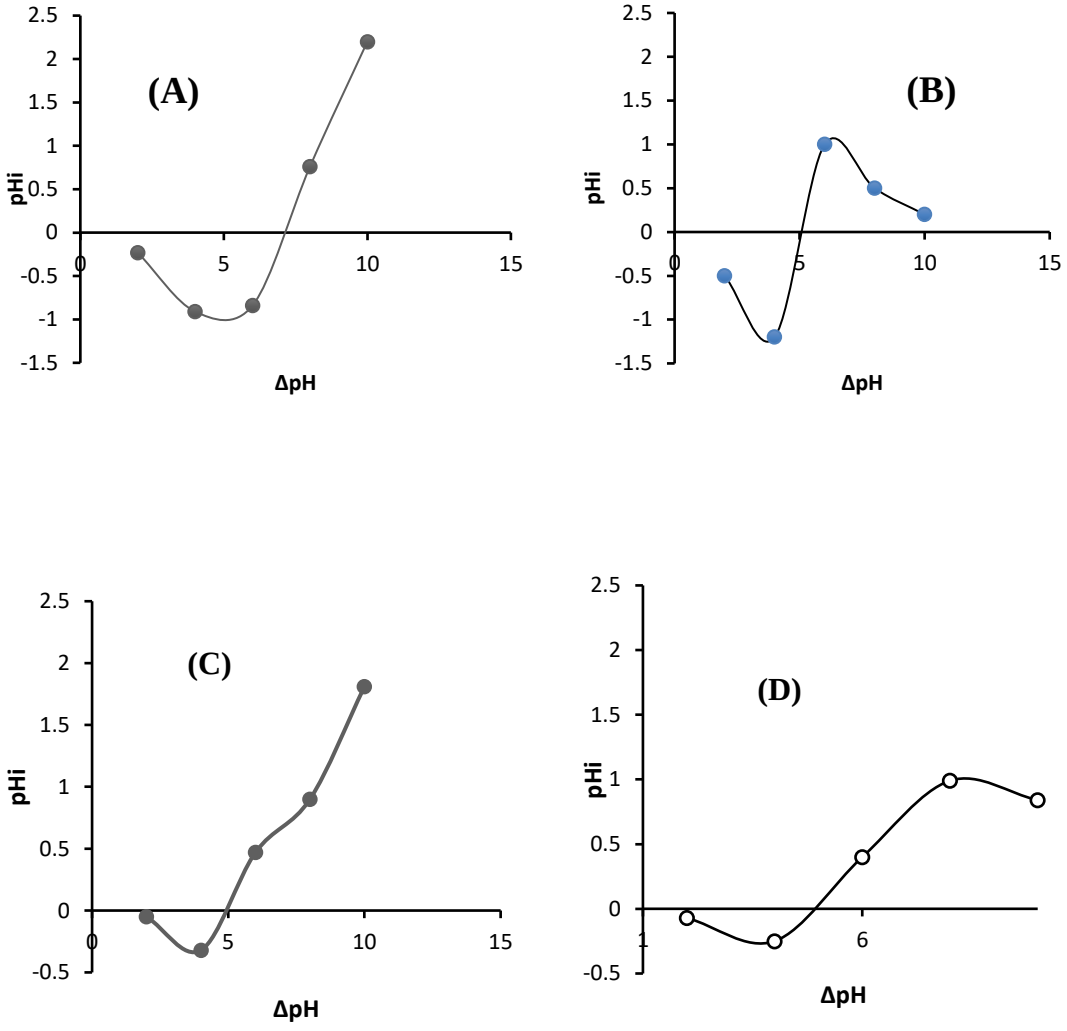

Figure 4.1: pH pzc for (A) RHAC (B) RH-ZnO-NC (C) PPAC (D) PP- ZnO-NC.

The moisture content for the RHAC, PPAC, RHAC-ZnO-NC, and PPAC-ZnO_NC were obtained. As shown in Table 4.1, low amount of moisture (in percentage) was calculated

for all adsorbents. The zinc oxide nanocomposites were observed to have lower moisture content values than the activated carbon. This could be attributed to the calcination step in the zinc oxide nanocomposites synthesis. The ash content is an important parameter to determine as it affects the efficiency of the adsorbents. A high amount of ash content reduces the effectiveness of the adsorbents. Hence, lower ash content values are preferred. As observed in Table 4.1, PPAC-ZnO-NC had lowest ash content of 12.18 % followed by PPAC with 14.21 %. Higher percentage ash content was observed in RHAC and RHAC-ZnO with 17.45 % and 15.23 % respectively.

Low amount of volatile matter (as shown in table 4.1) was obtained for all adsorbents and this implies that the adsorbents possess small particle density and that the prepared activated carbon and its nanoparticles would be an excellent materials for use as adsorbents (Ekpete et al., 2017b). Surface area is a parameter of utmost importance in adsorption studies. It is expected that adsorbent with higher surface area would have better adsorption capacity. As can be seen in Table 4.1, the surface area obtained for the nanocomposites was higher in comparison to the surface area of the activated carbon. This shows that incorporating nanoparticles into the activated carbon may increase the surface area. This observation is supported by the findings of (Sonawane, Patil, & Sonawane, 2018; Zeng & Xue, 2019).

4.1.1 Determination of Oxygen containing Functional groups (Boehm Titration)

The oxygen containing functional groups on all investigated adsorbents (PPAC, RHAC, PPAC-ZnO-NC and RHAC-ZnO-NC) were investigated using the Boehm titration method. Results as presented in Table 4.2 shows that the surfaces of all adsorbents, were predominantly acidic except the RHAC which had almost similar values for both acidic and basic sites. These values obtained were in agreement with the pH pzc values of each adsorbent which was more in the acidic region. And as such the uptake of cationic species will be favoured (Gündüz & Bayrak, 2017). A similar trend was observed by Mudyawabikwa *et al.,* (2017) which prepared activated carbon from tobacco stems.

Table 4.2: Oxygen Containing Functional groups

Groups	**RHAC**	**RHAC-ZnO-NC**	**PPAC**	**PPAC-ZnO-NC**
Carboxylic (meq/g)	0.07	0.5	0.6	0.5
Phenols (meq/g)	0.12	0.2	0.3	0.4
Lactones (meq/g)	0.03	0.6	0.7	0.3
Total Acidic sites	0.22	1.3	1.6	1.2
Total Basic sites (meq/g)	0.21	0.8	1.3	0.9

4.1.2 Iodine number determination

This physicochemical parameter gives a measure of the porosity and adsorptive capacity of adsorbents. The iodine number also gives an estimated surface area value for the adsorbents. A high iodine number value suggests the presence of large pores and large surface area. (Abdullah, Abdullah, Amin, and Zainol, 2018). Table 4.3 outlines the results of iodine adsorbed by 0.5g of sample.

Table 4.3: Iodine adsorption Values

	RHAC	RHAC-ZnO-NC	PPAC	PPAC-ZnO-NC
Iodine number	553.72	660.4	584.20	614.68
% Iodine	66	68	64	65.6
S_{BET} from iodine ($m^2.g^{-1}$)	545.96	651.15	576.02	606.07

4.1.3 Fourier Transform Infrared Analysis (FTIR)

FTIR analysis was performed to identify the existing functional groups on the adsorbents surface. Figure 4.2 and Figure 4.3 respectively show the FTIR spectra of RHAC, RHAC-ZnO-NC, PPAC and PPAC-ZnO-NC.

FTIR spectrum of RHAC showed notable peaks at 3317.3 cm^{-1} corresponding to the OH stretch indicating the intermolecular bond of OH group. Peaks at 2978 corresponds to the C-H aliphatic stretch. Peaks between 2100-2140cm^{-1} corresponds to C≡C stretch of alkynes. Peaks between 1770 and 1800 cm^{-1} represents C=O stretch. Notable peaks at 1028 and 790 cm^{-1} may be due to C-F and C-Cl stretch respectively. Shifting and disappearance of peaks were noticed for RHAC-ZnO-NC as shown in Figure 4.2 and Table 4.4.

Presented in Figure 4.3 are the FTIR spectra of PPAC and PPAC-ZnO-NC respectively. Table 4.5 shows the various band assignments of both PPAC and PPAC-ZnO-NC. Notable peaks were observed between 3300-3500 cm^{-1} corresponding to OH stretch of alcohols. The C-H aliphatic stretch at 2978 cm^{-1} was also observed, peaks at 1650-1740 cm^{-1} indicates presence of C=O of the lignin aromatic group. Similarly, loading of ZnO nanoparticles led to the shifting and disappearance of peaks. Cruz *et al.*, (2020) loaded ZnO nanoparticles onto biochars and noticed similar trends in peak and band assignments.

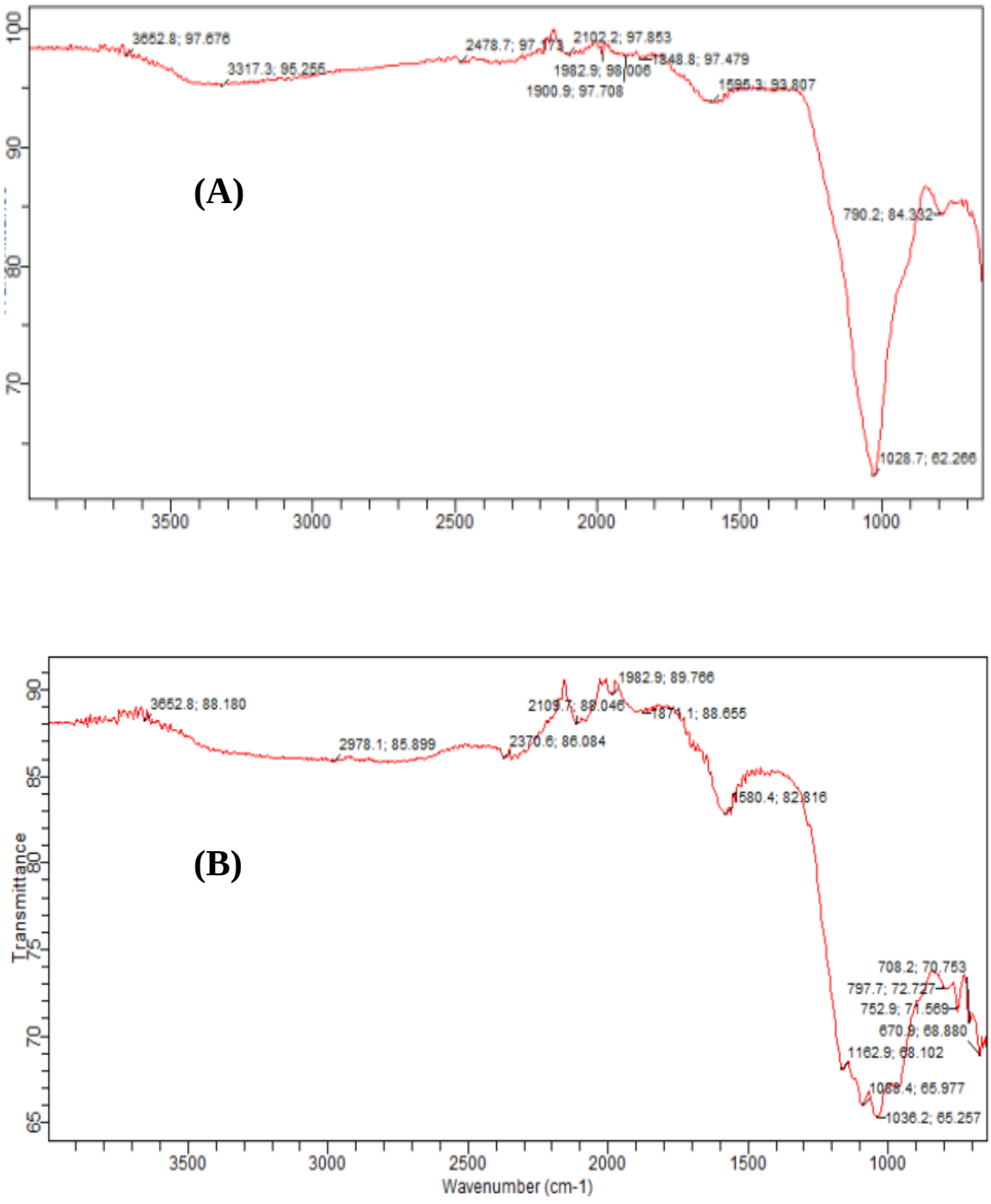

Figure 4.2: FTIR spectra of (a) RHAC (b) RHAC-ZnO-NC

Table 4.4: FTIR bands of RHAC and RHAC-ZnO-NC and their possible functional groups

IR Peak	**RHAC (cm^{-1})**	**Band Assignment**	**RHAC/ZnO**	**Band Assignment**
1	3662.8	O-H stretch	3652.8	O-H stretch
2	3317.3	O-H stretch	-	
3	-		2978.1	C-H aliphatic stretch
4	2478.7	H-C=O stretch	2370.6	C=N stretch
5	2102.2	C≡C stretch	2109.7	C≡C stretch
6	1982.9	C=O symmetric stretch	1982.9	C=O symmetric stretch
7	1900.9	C=O stretch	-	
8	1848.8	C=O stretch	1871.1	C=O stretch
9	1595.3	N-H bend	1580.4	N-H bend
10	-		1162.9	C-O stretch
11	1028.7	C-O stretch	1036.2	C-O stretch
12	790.2	=C-H bend	797.7	=C-H bend

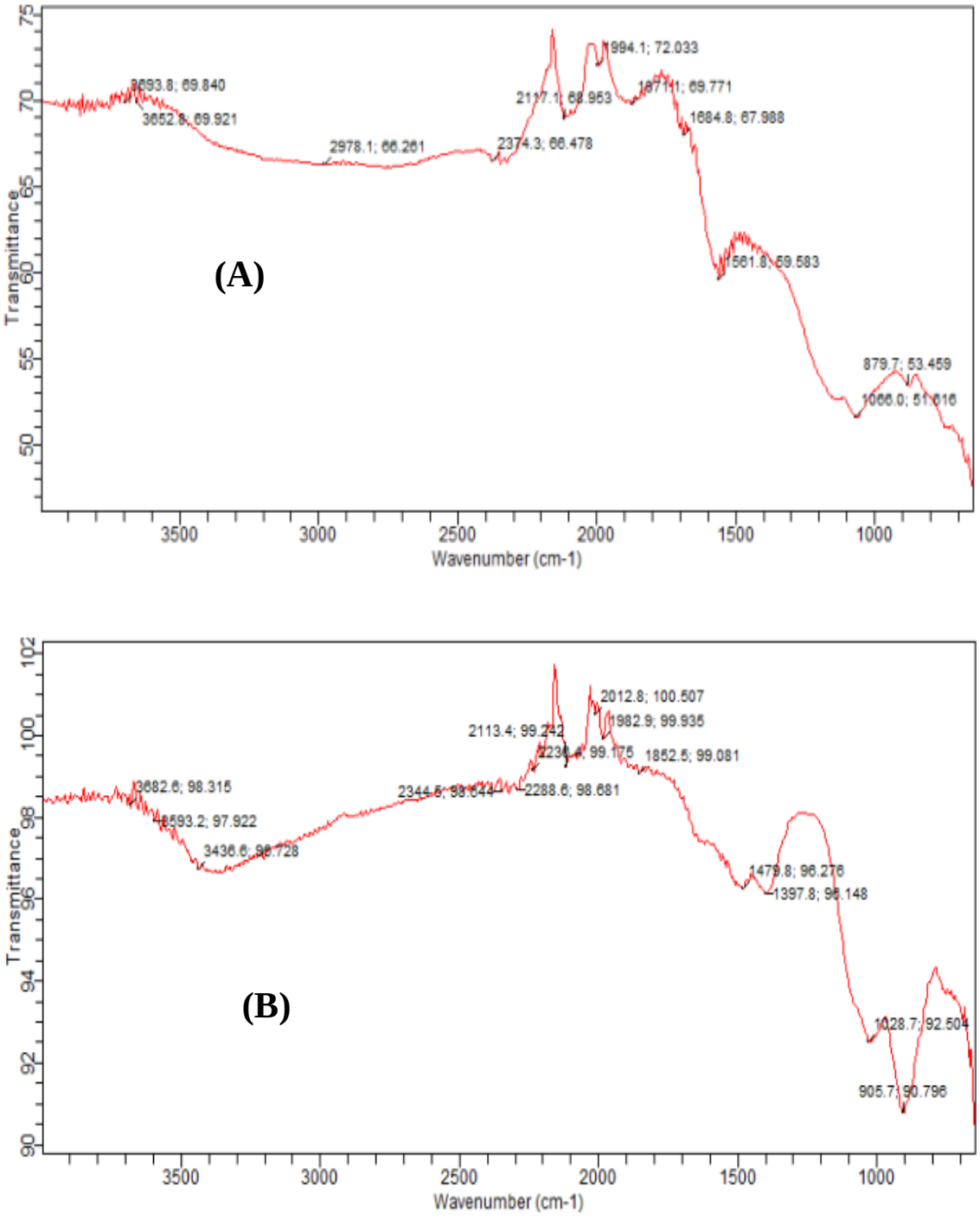

Figure 4.3: FTIR spectra of (a) PPAC and (b) PPAC-ZnO-NC

Table 4.5: FTIR bands of PPAC and PPAC-ZnO-NC and their possible functional groups.

IR Peaks	PPAC (cm^{-1})	Band Assignment	PPAC/ZnO	Band Assignment
1	3693.8	O-H stretch	3593.2	O-H stretch
2	3652.8	O-H stretch	3436.6	O-H stretch
3	2978.1	C-H stretch	-	
4	2374.3	C=N stretch	2344.5	C=N stretch
5	-		2288.6	C=N stretch
6	2117.1	C≡C stretch	2113.4	C≡C stretch
7	1994.1	C=O asymmetric stretch	2012.2	C≡C stretch
8	1684.8		-	
9	1561.8	N-O symmetric	1479.8	
10	1066.0		1028.7	=C-O-C symmetric
11	879.9	C-H	905.5	C-H bend

4.1.4 Scanning Electron Microscopic (SEM) Analysis.

Scanning Electron Microscopy identifies the surface characteristics, morphology and distribution of adsorbents as depicted on the SEM micrographs.

4.1.4.1 Scanning Electron Microscopic (SEM) studies on RHAC

Figure 4.4 shows the SEM micrograph of RHAC. The surface morphology revealed various pores suitable for trapping pollutants and enhancing the flow of adsorbate during adsorption. The raw RH was subjected to acid treatment and thermal modification which accounts for the presence of pores which serve as active sites for adsorption. SEM images revealed trapezonal, coarse, rough and cracked surface. Bello *et al.*, (2019) previously reported creation of pores due to acid modification of agro wastes.

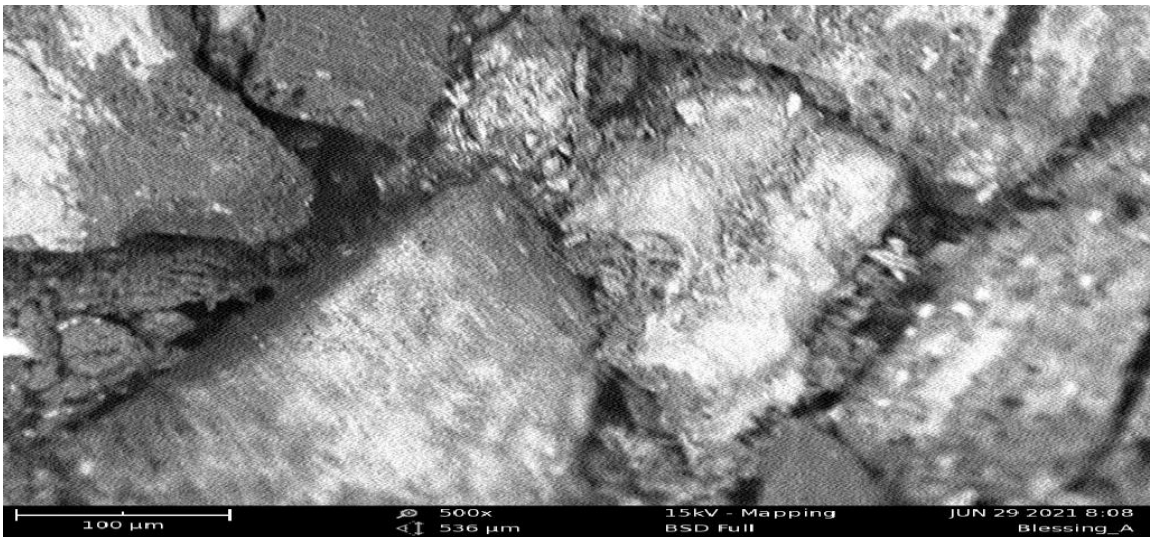

Figure 4.4: Scanning Electron Micrograph of RHAC (x500 magnification)

4.1.4.2 Scanning Electron Microscopic studies on RHAC-ZnO-NC

SEM micrograph of RHAC-ZnO-NC is shown in Figure 4.5. Image revealed presence of more pores and increase in cracks with capacity to trap pollutants and thus increase its adsorption capacity. This could be attributed to the loading of ZnO nanoparticles onto the RHAC matrix. Previous reports on increased porosity due to loading of ZnO nanoparticles have been reported (Steplin *et al.*, 2018 ; Mohammed *et al.*, 2019).

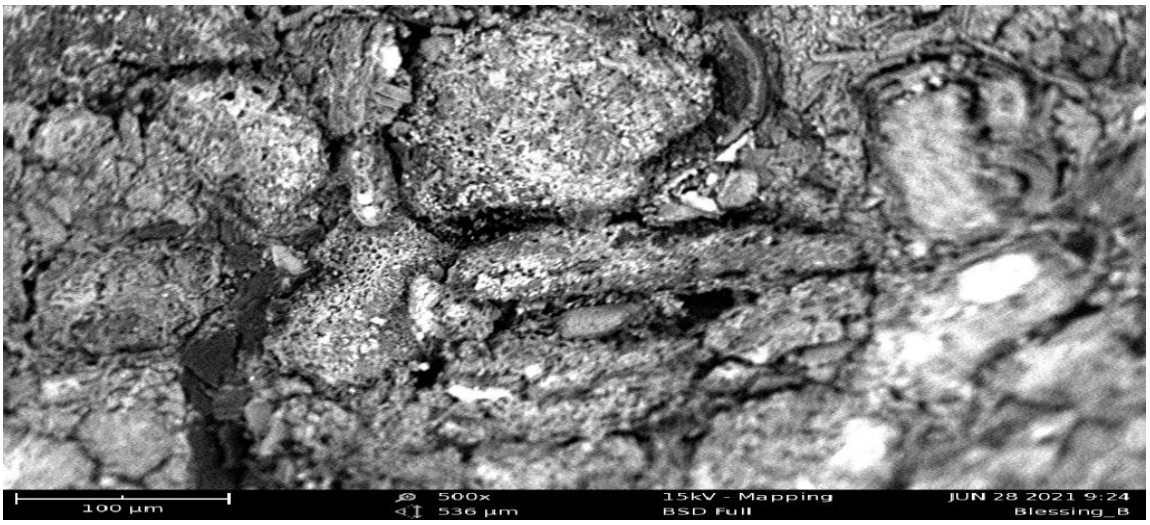

Figure 4.5: Scanning Electron Micrograph of RHAC-ZnO-NC (x500 magnification)

4.1.4.3 Scanning Electron Microscopic studies on PPAC

The surface morphology of PPAC is shown in Figure 4.6, SEM image revealed various pores of different shapes and sizes with fine surface texture. Theses pores could be due to the chemical modification of the plantain peel followed by thermal activation. These pores would serve as sites for the uptake of pollutants.

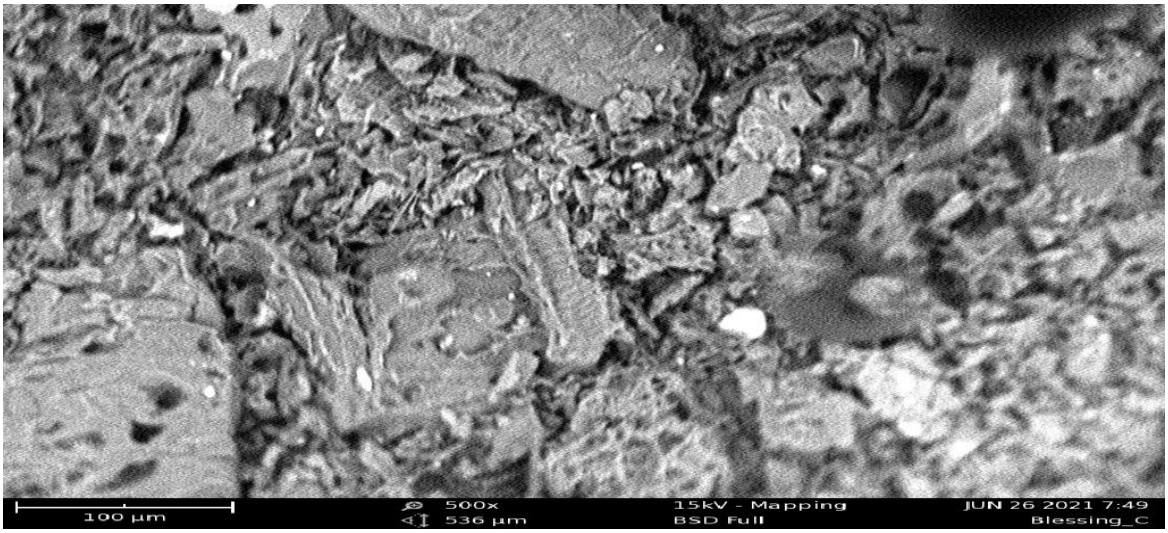

Figure 4.6: Scanning Electron Micrograph of PPAC (x500 magnification)

4.1.4.4 Scanning Electron Microscopic studies on PPAC-ZnO-NC

The surface morphology of PPAC revealed closely packed, spherical crumbled surface as shown in Figure 4.7. The loading of ZnO onto PPAC may have led to the increase in pores, thereby, providing a large surface area for adsorption.

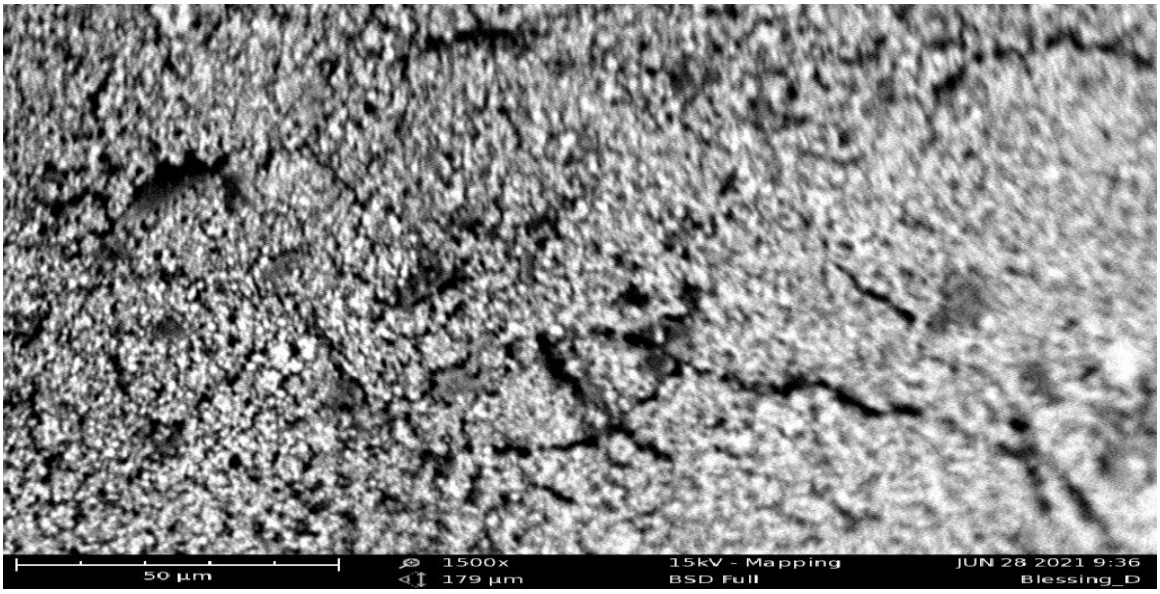

Figure 4.7: Scanning Electron Micrograph of PPAC-ZnO-NC (x500 magnification)

4.1.5 XRD analysis on Nano Composites

Analysis of nanocomposites using the X-ray Diffraction (XRD) method was carried out to investigate and examine the material structure of the zinc oxide nanocomposites. Thereby confirming the loading of ZnO onto the activated carbon derived from rice husk and plantain peel.

The XRD pattern of RHAC-ZnO-NC is shown in Figure 4.8. The plots show that a high percentage (71%) of Zinc Oxide (Zincate) was loaded onto the RHAC. Figure 4.9 shows the XRD pattern of PPAC-ZnO-NC and plots also show a high percentage (71%) of Zinc Oxide (Zincate) was loaded onto the PPAC.

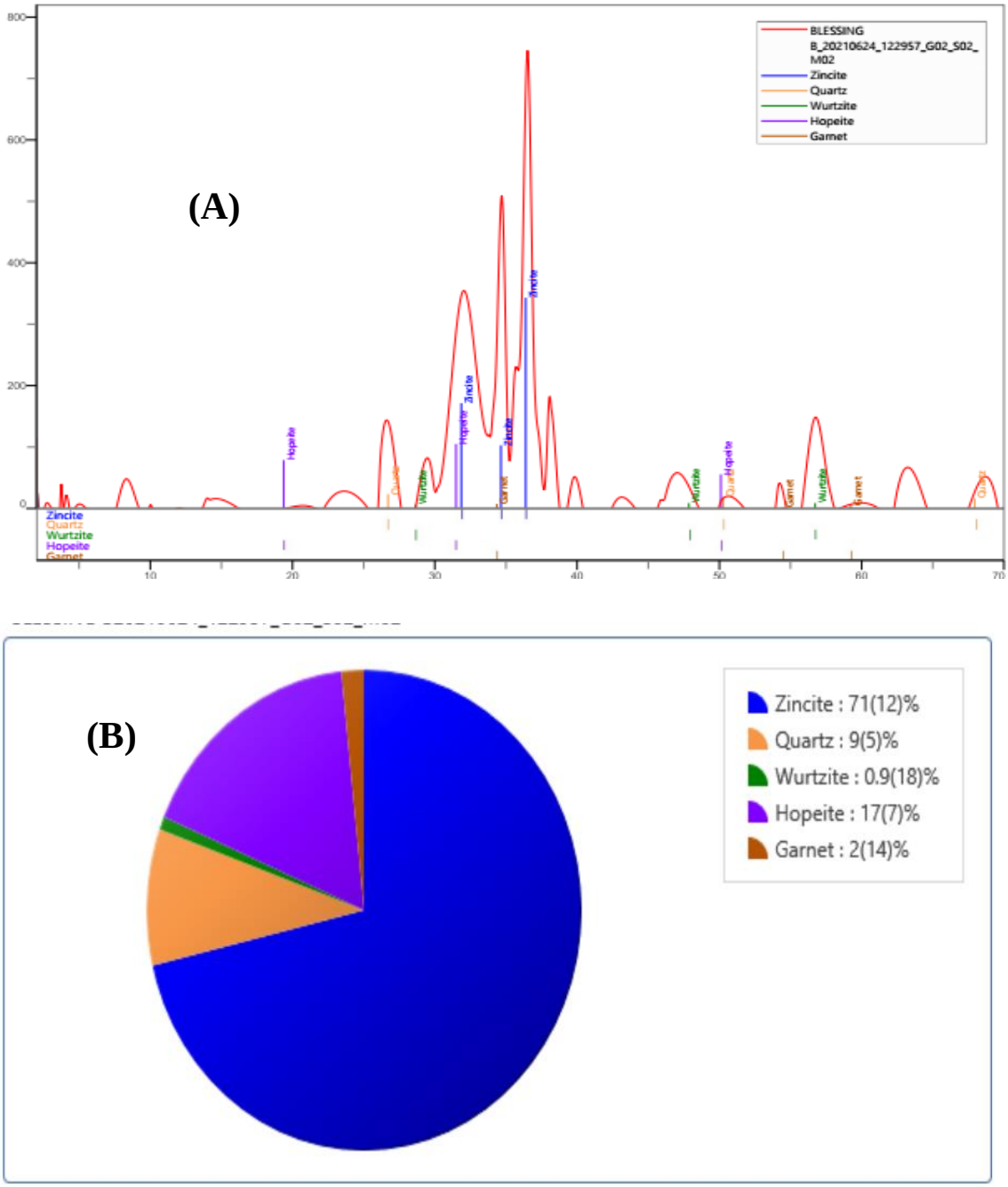

Figure 4.8 (A & B): (A) XRD pattern and (B) pie chart distribution of RHAC-ZnO-NC.

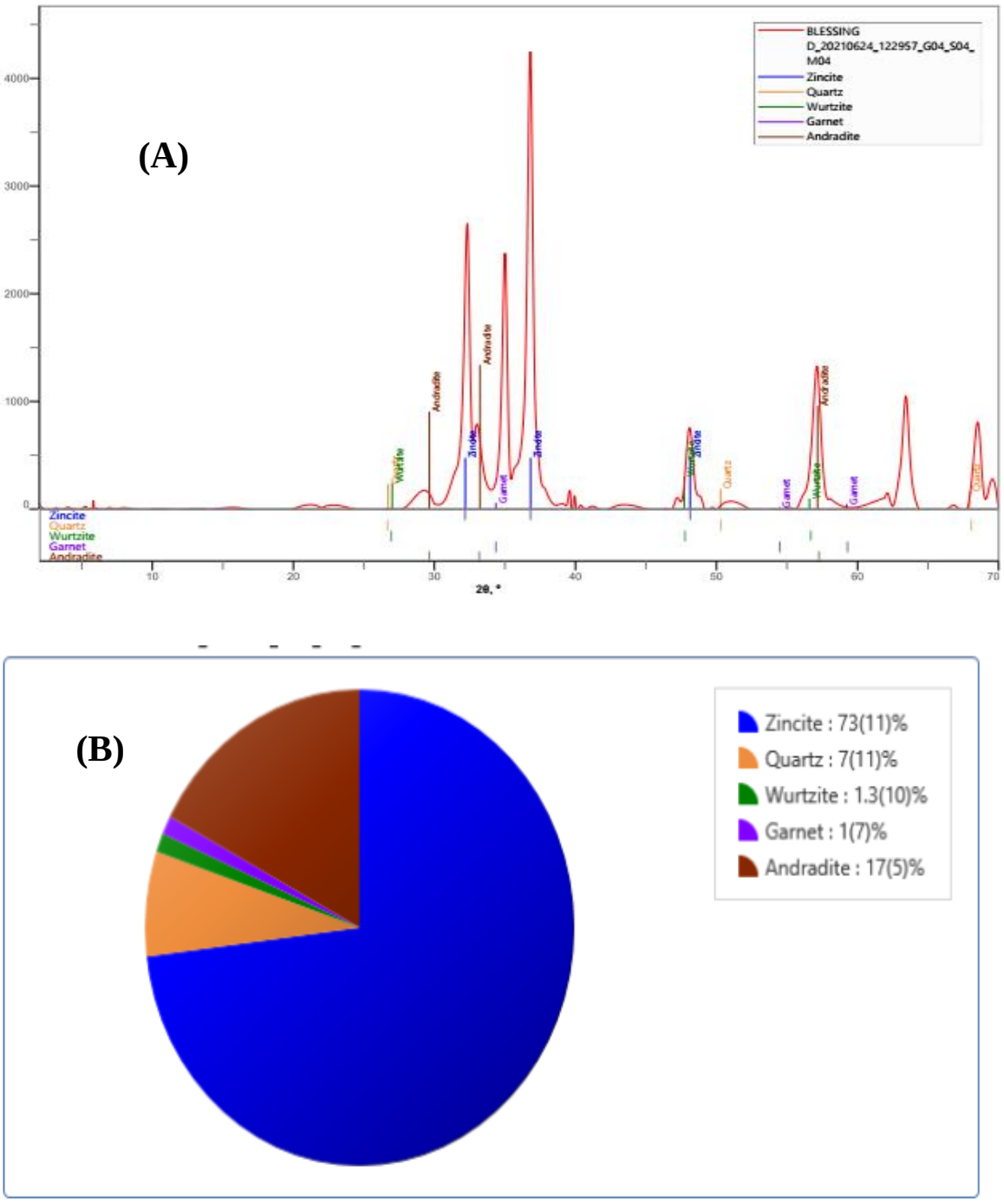

Figure 4.9 (A & B): (A) XRD pattern and (B) pie chart distribution of PPAC-ZnO-NC.

4.2 Chloroquine Adsorption Studies

4.2.1 Maximum Adsorption wavelength for Chloroquine

The maximum absorption peak of chloroquine pharmaceutical is shown in the Figure 4.10. This peak was obtained when a known concentration of CQ solution was scanned between 100 – 400 nm. The maximum absorbance was obtained at 299 nm and as such, the residual concentration after each adsorption was determined at this wavelength.

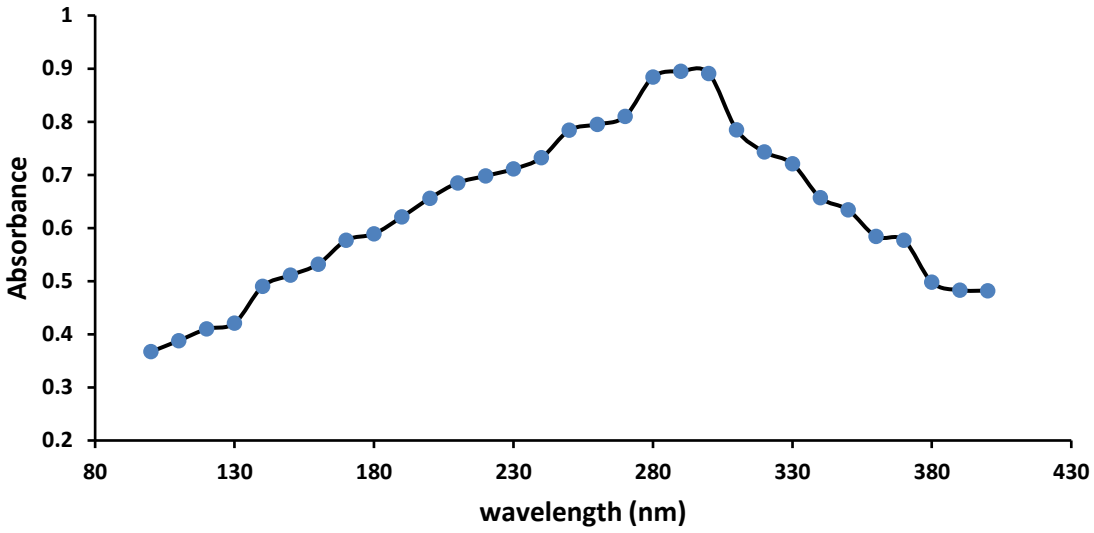

Figure 4.10: Absorbance Spectrum of Chloroquine (λ_{max}=299 nm)

4.2.2 Calibration Curve for Chloroquine

The Figure 4.11 shows the calibration curve for CQ. This was obtained by preparing various concentration of CQ from 10 to 50 mg/L and the absorbance checked at a constant wavelength of 299 nm. A plot of absorbance versus concentrations was done and the R^2 (correlation coefficient) value obtained implies the linearity of the calibration curve. The equation of the plot obtained was used to calculate the residual concentrations of the CQ pharmaceutical during the adsorption process.

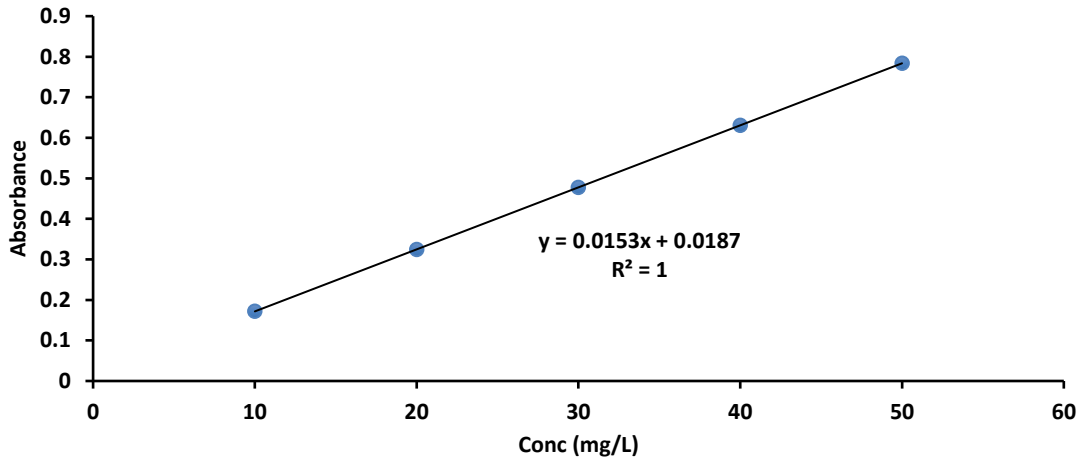

Figure 4.11: Calibration Curve for CQ adsorption

4.2.3 Adsorption Studies of Chloroquine onto RHAC, PPAC, RHAC-ZnO-NC and PPAC-ZnO-NC.

4.2.3.1 Effects of Contact Time, Initial Concentration, and Temperature

The effects of initial adsorbate concentration and agitation time for the sorption of CQ was observed and is shown in Figures 4.12-4.15. For uptake of CQ onto RHAC and PPAC, the adsorption process was fast for the first 40 minutes while for RHAC-ZnO-NC and PPAC-ZnO-NC, rapid uptake occurred within the first 20 minutes. This trend observed could be on account of the presence of more active adsorption sites at the initial stages. The uptake then gradually became slower until equilibrium was attained. This decline could be as a result of adsorbent-adsorbate interferences thereby making adsorbent sites unavailable for adsorption.

Also, for all adsorption systems, as the initial concentration increased, it was observed that the quantity adsorbed at specific time (Q_t) increased. This could be attributed to the fact that higher initial CQ concentrations increased the initial concentration gradient. This led to an increase in the driving force which helped to overcome mass transfer resistance thereby increasing the uptake of CQ molecules. At equilibrium point, the amount of CQ adsorbed by RHAC, RHAC-ZnO-NC, PPAC and PPAC-ZnO-NC at initial concentration of 10 mg/L was 8.6 mg/L, 9.3 mg/L, 9.5 mg/L and 8.7 mg/L respectively, while at initial concentration of 50 mg/L, amount of CQ adsorbed was 32.20 mg/L, 38.41 mg/L, 38.01

mg/L and 31.09 mg/L respectively. Similar trend was observed by Agboola *et al.*, (2021) for the uptake of lumefantrine onto functionalized banana stalk.

The percentage removal however decreased as the initial adsorbate concentration increased. Percentage removal of 86.07% was observed for initial CQ concentration of 10 mg/L and 64.4% removal for initial CQ concentration of 50 mg/L. Similar trend was observed for all other adsorption systems. This decrease could be due to the increase in competition for pores by CQ molecules at higher initial concentrations.

For all adsorption systems, increase in temperature generally led to an increase in uptake of CQ molecules (as shown in Figure 4.16). This trend can be attributed to the availability of more adsorption sites at higher temperatures.

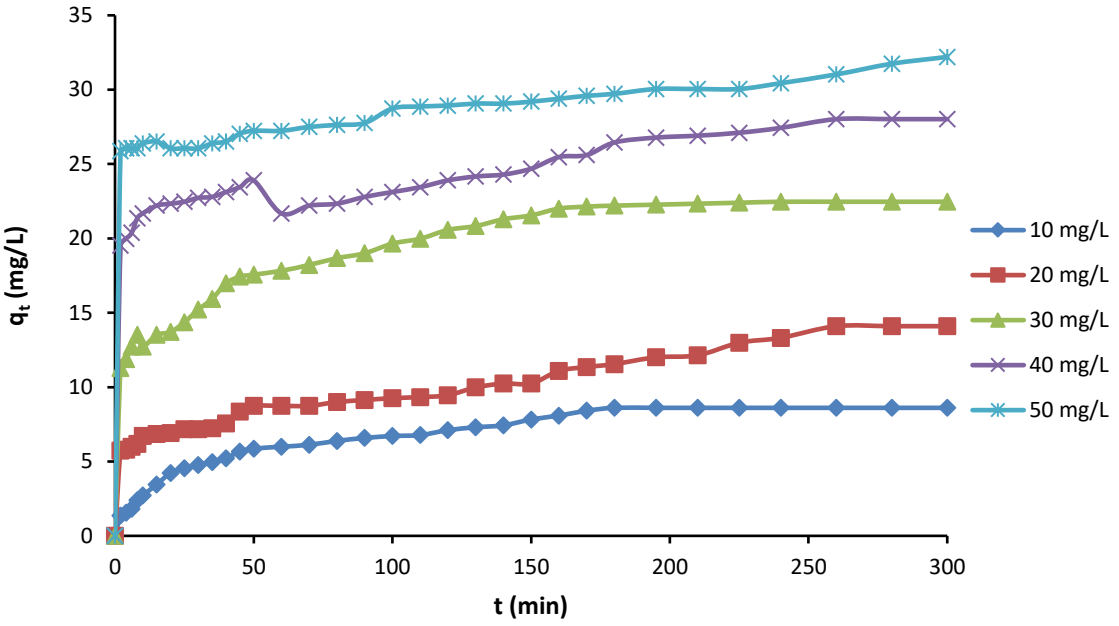

Figure 4.12: Effects of Concentration and Contact time for CQ-RHAC system

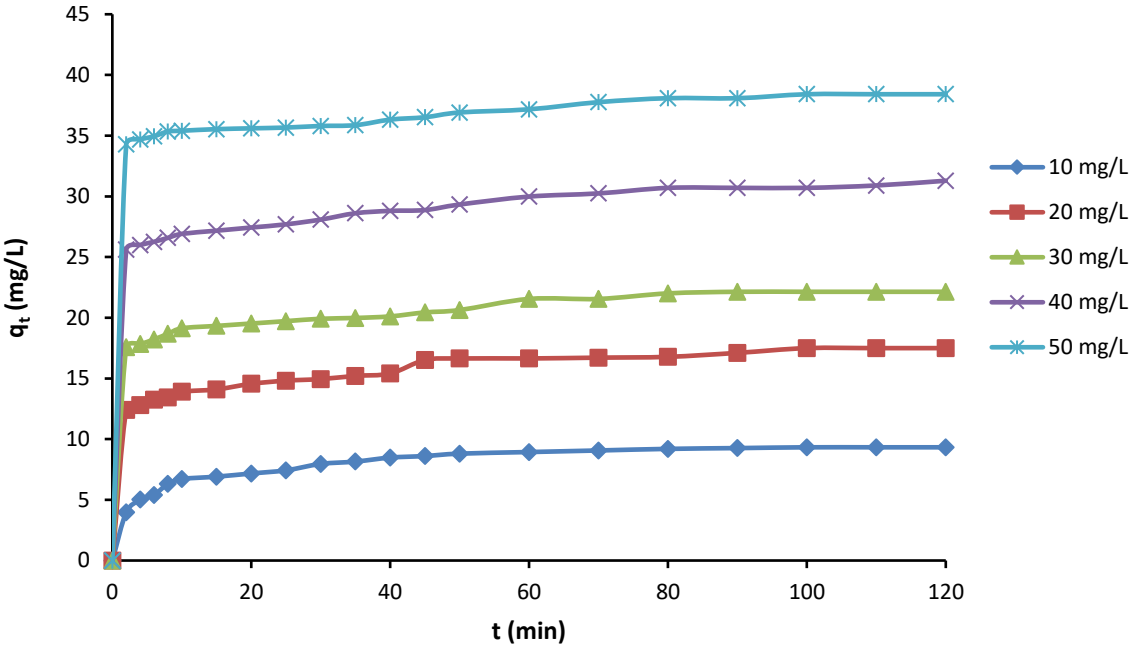

Figure 4.13: Effects of Initial Concentration and Contact time on CQ uptake unto RHAC-ZnO-NC

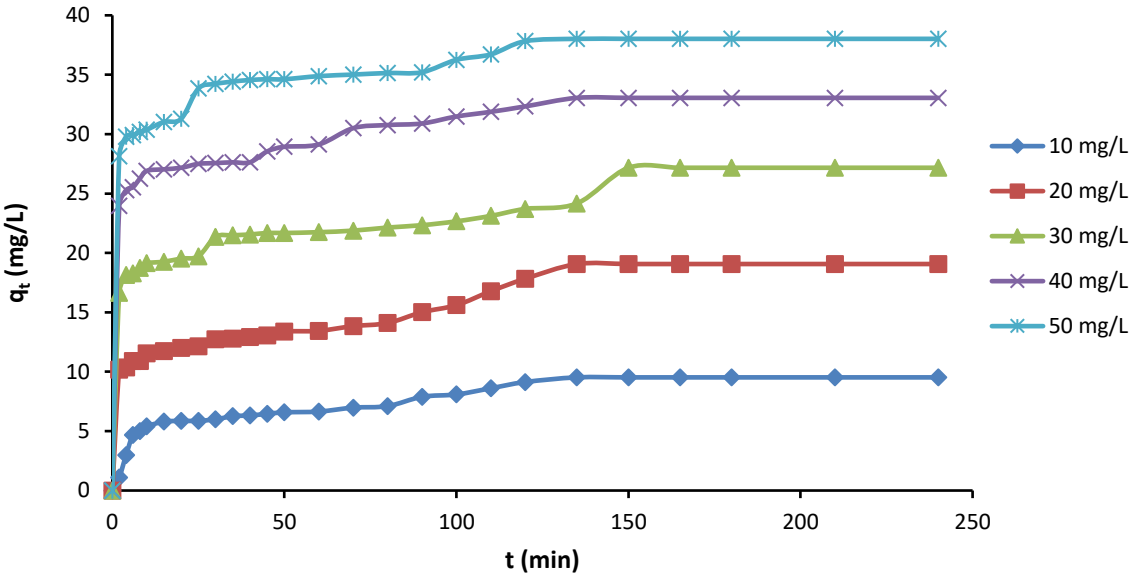

Figure 4.14: Effect of concentration and contact time for uptake of CQ onto PPAC

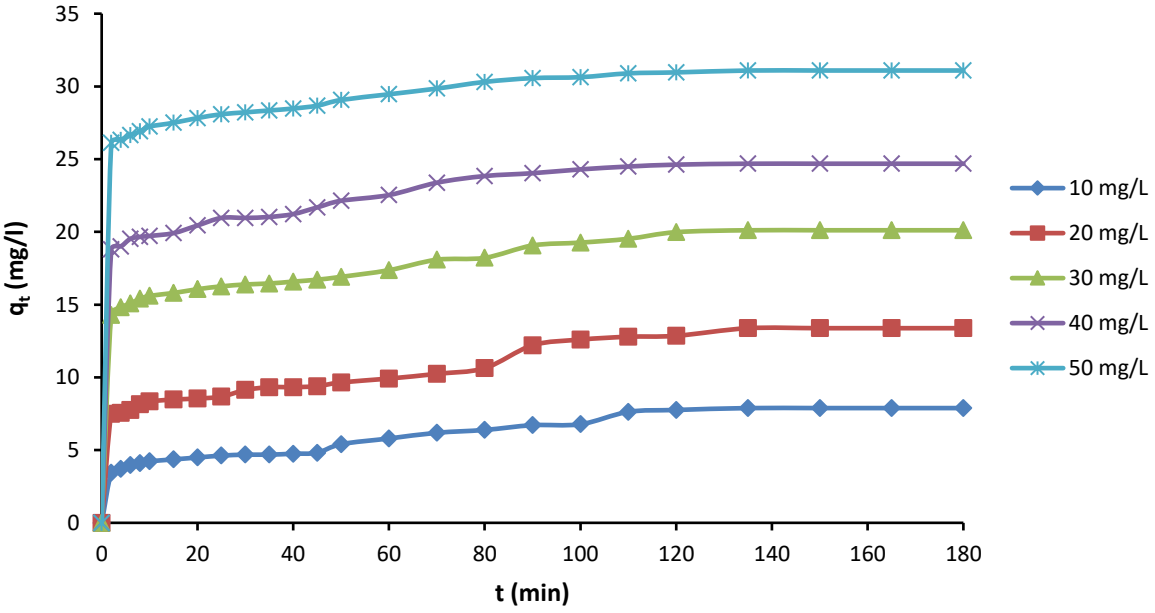

Figure 4.15: Effect of concentration and contact time for uptake of CQ onto PPAC-ZnO-NC

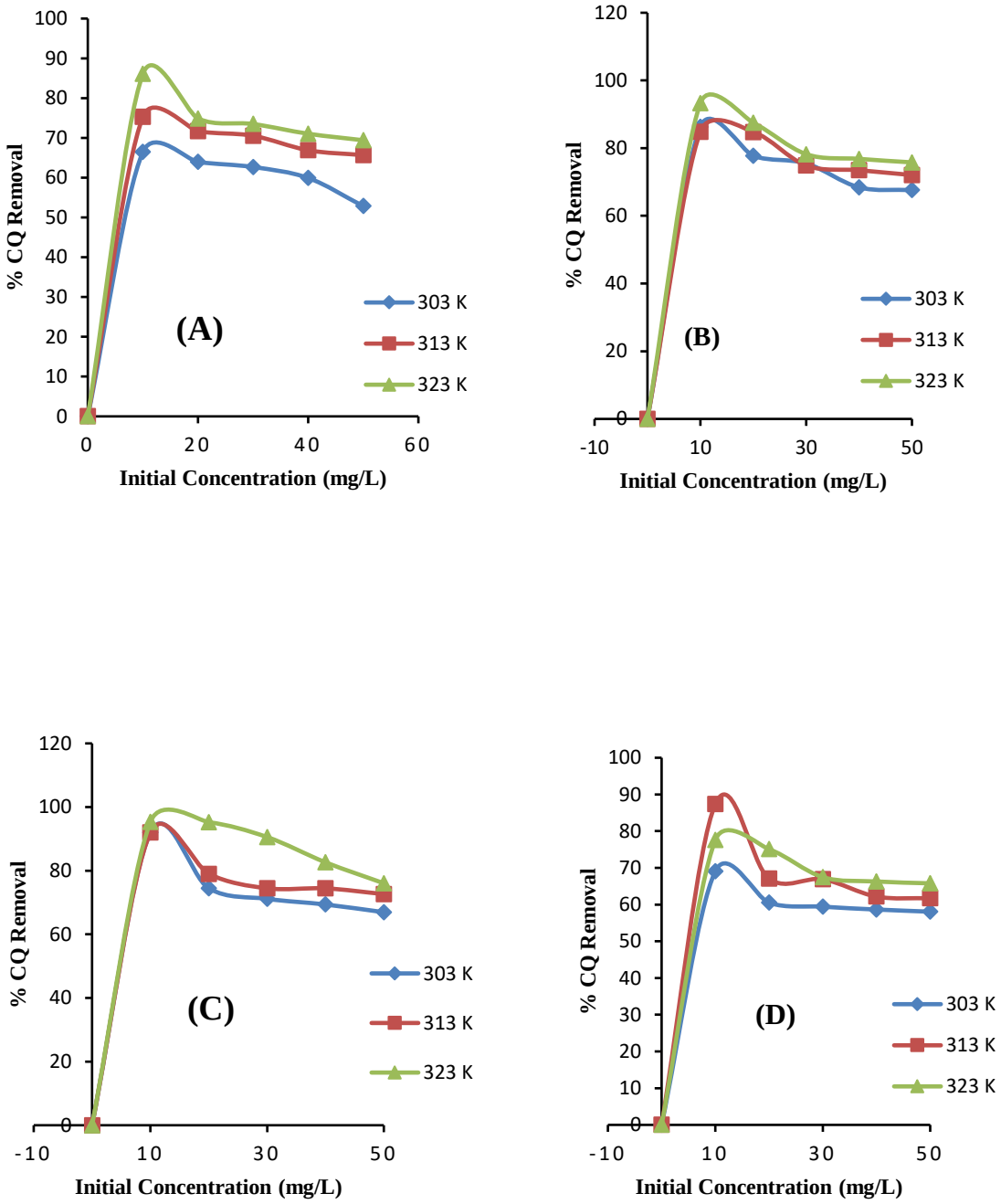

Figure 4.16: Effect of temperature on the uptake of CQ onto (A)RHAC (B)RHAC-ZnO-NC (C)PPAC (D)PPAC-ZnO-NC.

4.2.3.2 Effects of pH

Figure 4.17 shows the effect solution pH has on the uptake of CQ by all adsorbents. This was determined at pH values ranging from pH 3-11 to observe which has the best percentage removal. In solution form, most CQ molecules are cationic and as such form positively charged ions in solution.

For all adsorbents, the highest percentage removal was observed between pH 5 and 7. RHAC had 50.9 % removal at pH 7 while for RHAC-ZnO-NC, 81.7 % removal was observed at pH 7, PPAC however had 81.7 % at pH 5 while PPAC-ZnO-NC had 84.5 % removal at pH 5. Since these values are higher than the pH_{pzc}, the pH of highest percentage removal could be as a result of negative charges on the adsorbents surface at higher pH values than pH_{pzc} resulting to the attraction between adsorbent surface and CQ molecules.

At values of pH lower than the $pH_{pzc,}$ the surface of the adsorbent becomes positively charged which causes a repulsion between CQ molecules and adsorbent surfaces, thereby reducing the CQ uptake in this region as can be observed in Figure 4.17. Similar trend was observed by Ferreira *et al.*, (2015) who reported on the uptake of paracetamol by coconut mesocarp.

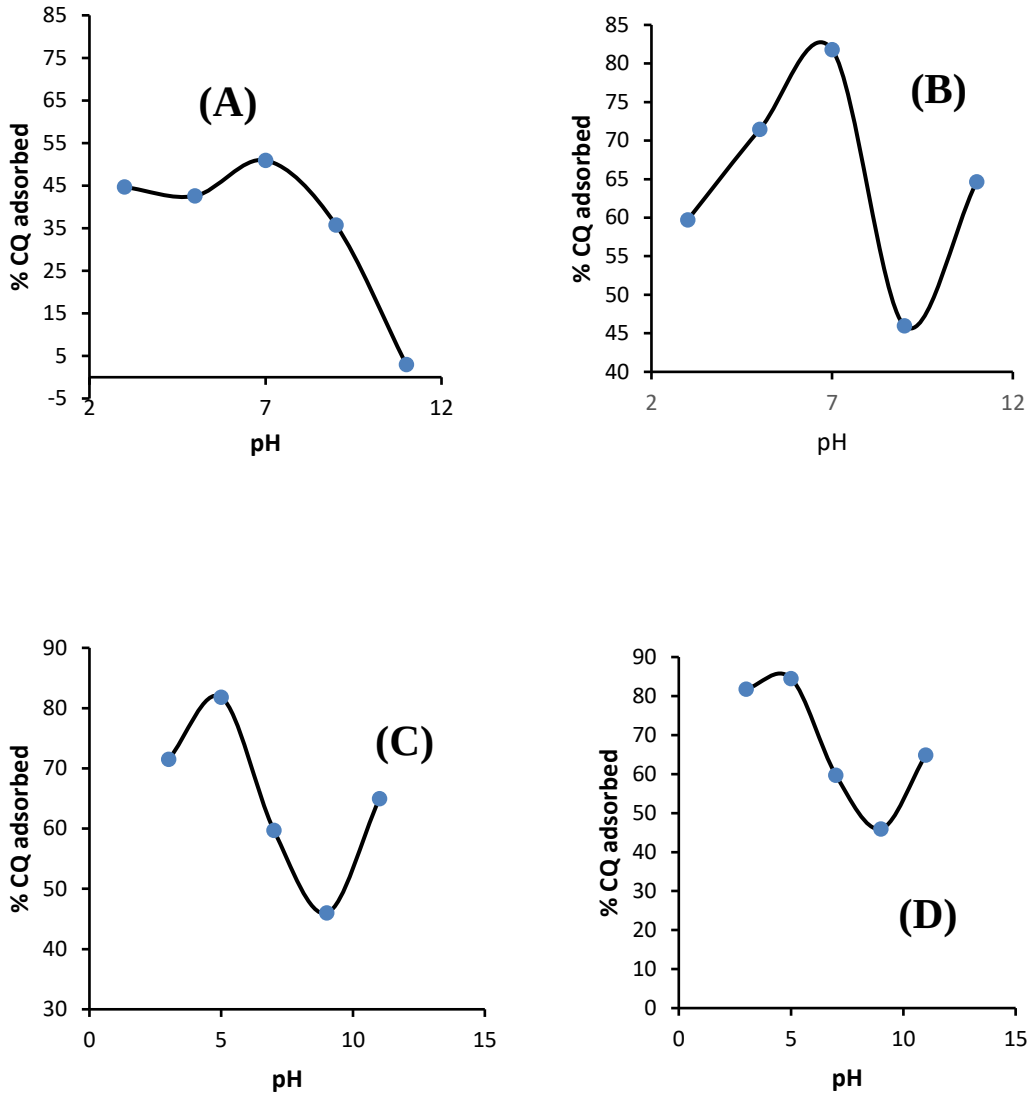

Figure 4.17: Effects of pH on uptake of CQ onto (A) RHAC (B) RHAC-ZnO-NC (C) PPAC and (D) PPAC-ZnO-NC.

4.2.3.3 Isotherm Studies

Isotherm studies were carried out to further understand the nature of the adsorbent-adsorbate interactions for all adsorption systems. The various data obtained from the isotherm models (Langmuir, Freundlich, Temkin and Dubunin-Radushkelvich) considered in this study are shown in Figures 4.18 - 4.21 and outlined in Tables 4.6 - 4.9.

4.2.3.3.1 RHAC-CQ Adsorption System

The adsorption data for sorption onto RHAC was analysed using the Freundlich, Langmuir, Temkin and D-R isotherms as shown in Table 4.6 and Figure 4.18. The Langmuir isotherm plot and parameters are shown in Figure 4.18a and Table 4.6 respectively. At 323 K, R^2 value of 0.76 was obtained while the separation factor (R_L) value of less than 1 (0.14) suggesting its favourability was obtained (Ahmad et al., 2020; Muinde *et al.,* 2020). The q_{max} however was calculated as 54.05 mg/g. Shown in Figure 4.18 is the Freundlich isotherm plot of log q_e versus log C_e. R^2 value of 0.93 was obtained while the K_F of 7.2 suggests the Freundlich adsorption capacity. Based on the evaluated parameters, adsorption isotherm data best fitted the Freundlich isotherm model. Across temperatures, the n value indicating adsorption intensity was in the range of (1.64-2.2). The value of n being less than 10 suggests a favourable adsorption. This was in line with the findings of Dada et al., (2020). Temkin isotherm was considered by plotting q_e versus ln C_e (Figure 4.18c). High b_t value (257.09) was obtained, K_t value of 1.32 was obtained and the R^2 value (0.86) showed that the Temkin isotherm could describe the nature of the sorption process. The D-R plot of ln q_e versus E^2 was also made. The Q_{max} obtained was low (29.22) in comparison to the Langmuir q_{max}. The R^2 value of 0.88 was obtained however, the E value (0.85 kJ/mol) suggests physiosorption (Lazim *et al.*, 2021).

4.2.3.3.2 RHAC-ZnO-NC-CQ system

From the adsorption data obtained, a plot of C_e/q_e against C_e was made for the Langmuir isotherm (as shown in figure 4.19). The maximum adsorption capacity of 169.49 mg/g was obtained for uptake of CQ onto RHAC-ZnO-NC at 323 K with R^2 value of 0.76. The separation factor (R_L) value of less than 1 (0.68) was obtained for all temperatures investigated and this suggests the favourability of the sorption process (Dada *et al.,* 2020; Inyinbor *et al.,* 2016). The Freundlich Isotherm (as shown in Table 4.7) however has an R^2 value of 0.99 and the n values calculated at all temperatures were greater than 1 which suggests that the interaction is favourable, simple and physical. The high R^2 (0.968) obtained from the Temkin isotherm suggests its usability for describing the sorption process. The positive B_T values across all temperatures describes the nature of the heat of

adsorption as endothermic. All E values of the D-R isotherm were less than 8 KJ/mol which suggests physio sorption. However, the q_m values obtained from the D-R plot were low (29.4 mg/g) compared to those obtained from the Langmuir plot and therefore cannot be used to describe the sorption process (Gündüz & Bayrak, 2017).

4.2.3.4.3 PPAC-CQ system

Figure 4.20 and Table 4.9 shows the Isotherm plots and parameters. The R_L value from the Langmuir Isotherm was found to be 0.07 (less than 1) which implies that the uptake of CQ onto PPAC is favourable. The maximum adsorption capacity (monolayer) (q_{max}) was found to be 39.68 mg/g with 0.96 as the R^2 value. The Freundlich adsorption Isotherm had an R^2 value of 0.96, therefore implying that heterogenous adsorption took place. All n values were greater than 1 implying that the uptake is physical and favourable. For the Temkin isotherm, the closeness of the R^2 value to 1 (0.92) suggests the presence of adsorbate-adsorbent interaction in the sorption process. The D-R plot gave an R^2 value (0.76). The adsorption Energy lower than 8 kJ/mol was obtained showing that the sorption CQ was physio-sorption. Similar trend of results were observed and reported by (Gupta, Kushwaha, & Chattopadhyaya, 2016)

4.2.3.4.4 PPAC-ZnO-NC-CQ system

For the PPAC-ZnO-NC-CQ system, Langmuir Isotherm plot and parameters are shown in Table 4.10 and Figure 4.21(A). The R_L value was found to be 0.19 (less than 1) this implies that the adsorptive uptake of CQ onto PPAC-ZnO-NC is favourable. The maximum monolayer adsorption capacity (q_{max}) was found to be 50.50 mg/g. The Freundlich adsorption Isotherm (as shown in Figure 4.18b), best fitted the adsorption data with a high R^2 value of 0.98, therefore implying that heterogenous adsorption took place. All n values were also greater than 1 supporting the fact that the adsorption is favourable. As shown in Figure 4.21c, the Temkin Isotherm plot obtained an R^2 value of 0.99. the closeness of this value to 1 suggests the presence of adsorbate-adsorbent interaction in the sorption process. The D-R plot gave an R^2 value of 0.91. However, the adsorption Energy of 0.7 kJ/mol (lower than 8 KJ/mol) shows that the sorption of CQ onto PPAC was physio-sorption. Ekpete, Marcus, & Osi, (2017a) reported a similar trend.

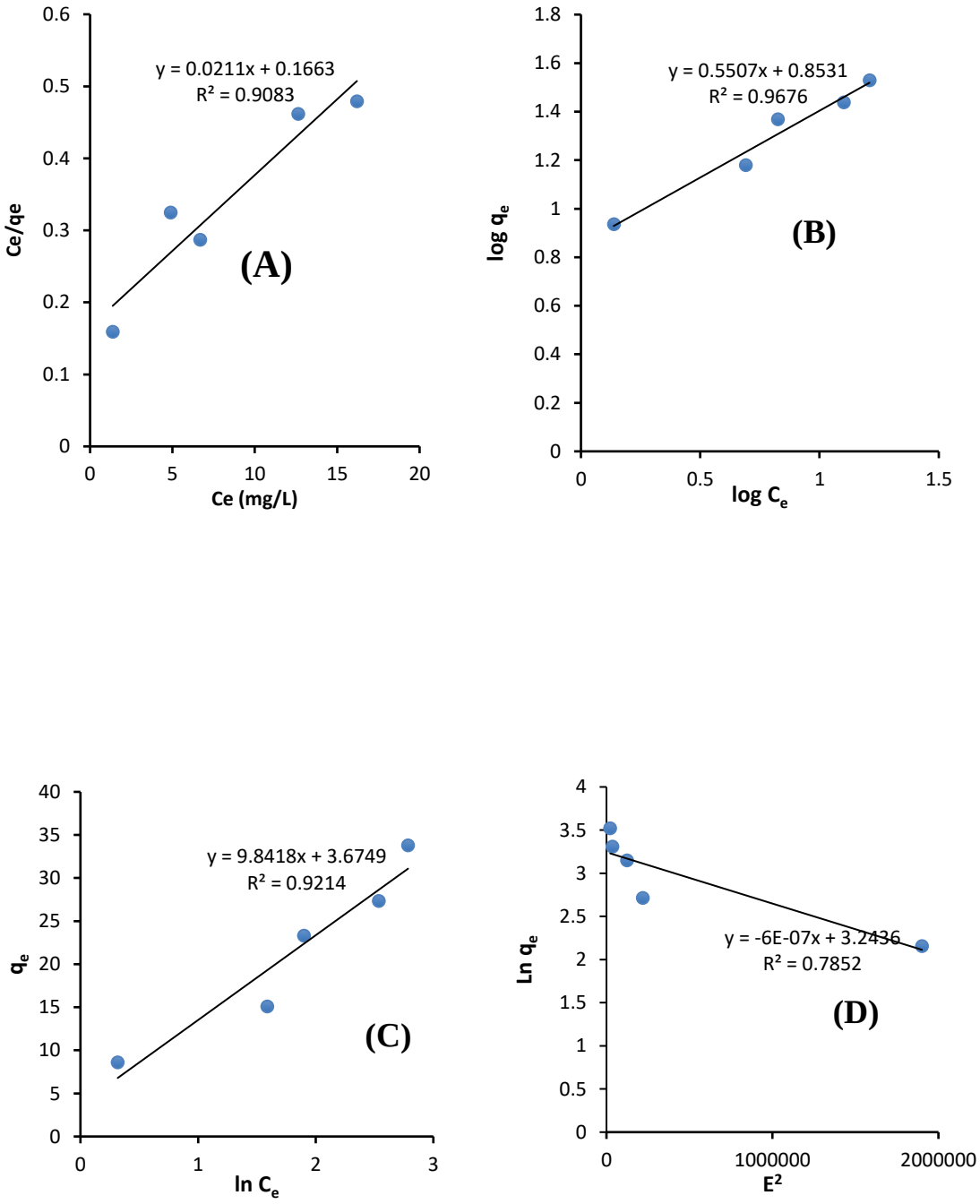

Figure 4.18: (A)Langmuir (B) Freundlich (C)Temkin and (D) D-R linear Isotherm plots for RHAC-CQ System.

Table 4.6: Adsorption Isotherm Parameters for uptake of CQ using RHAC at Different Temperatures

	Parameters	303K	313 K	323 K
Langmuir	q_m (mg/g)	43.29	47.39	54.05
	K_L (l/mg)	0.27	0.13	0.12
	R_L	0.06	0.14	0.14
	R^2	0.81	0.91	0.76
Freundlich	K_f (mg/g(L/mg))$^{1/n}$	11.18	7.13	7.17
	n	2.22	1.81	1.64
	R^2	0.94	0.96	0.93
Temkin	B_T	319.73	255.96	227.09
	K_t	3.56	1.45	1.32
	R^2	0.84	0.92	0.87
D-R	E_a (kJ/mol)	1.58	0.91	0.85
	q_m (mg/g)	27.73	25.63	29.22
	R^2	0.79	0.79	0.88
	β x10^{-7}($Mol^2.kJ^{-2}$)	2.0	6.0	7.0

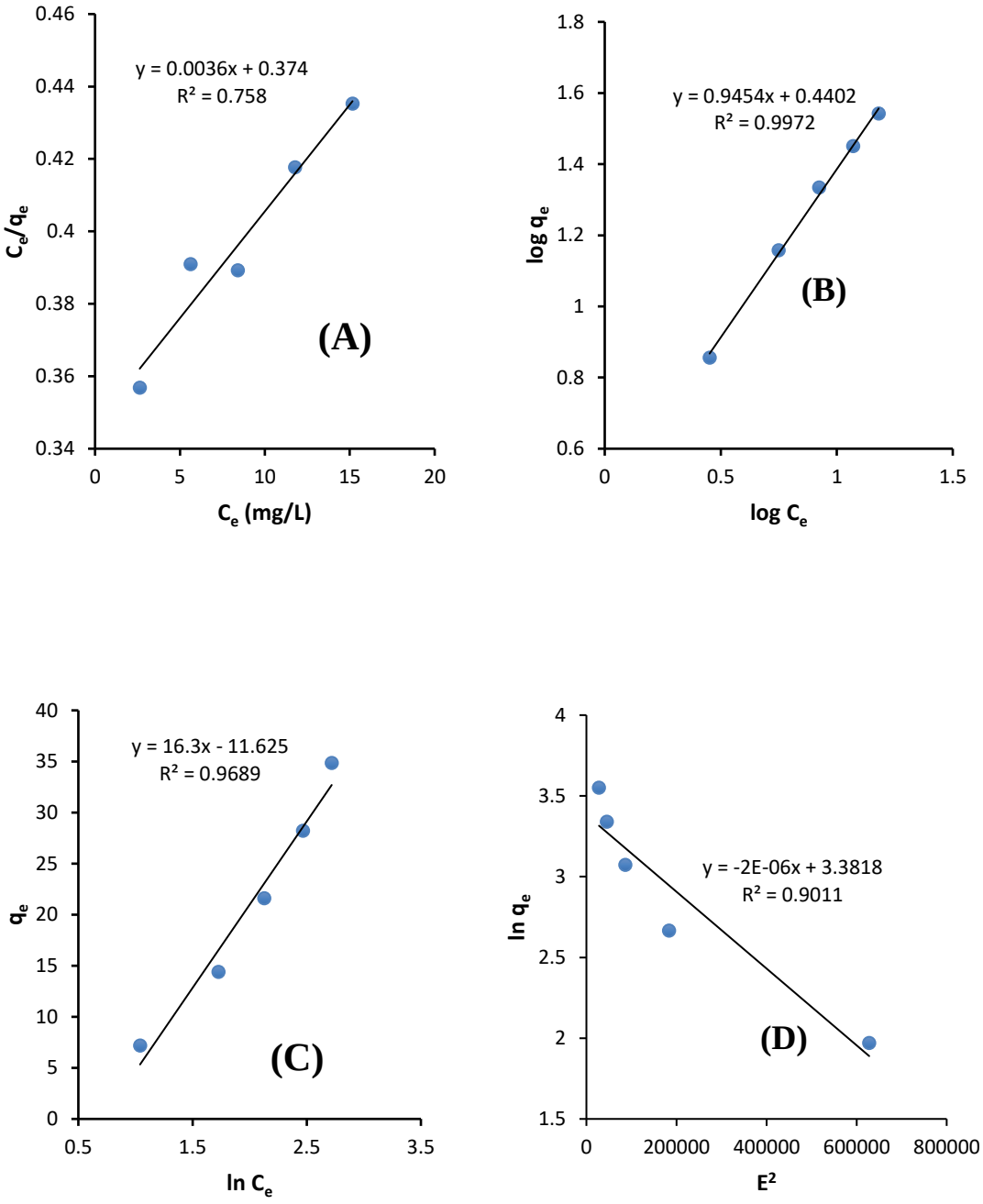

Figure 4.19: (A)Langmuir (B) Freundlich (C)Temkin and (D) D-R linear Isotherm plots for RHAC-ZnO-NC-CQ System.

Table 4.7: Adsorption Isotherm Parameters for uptake of CQ using RHAC-ZnO-NC at Different Temperatures

	Parameters	303 K	313 K	323 K
Langmuir	q_m (mg/g)	51.02	149.24	169.49
	K_L (l/mg)	0.109	0.01	0.0096
	R_L	0.154	0.59	0.675
	R^2	0.911	0.86	0.758
Freundlich	K_f (mg/g(L/mg))$^{1/n}$	6.849	2.75	2.256
	n	1.756	1.13	1.058
	R^2	0.991	0.99	0.997
Temkin	B_T	246.926	159.65	197.704
	K_t	1.34	2.37	2.040
	R^2	0.924	0.94	0.968
D-R	E_a (kJ/mol)	91.3	5.0	40.8
	q_m (mg/g)	25.65	24.78	29.423
	R^2	0.78	0.86	0.90
	β x 10^{-6}($Mol^2.kJ^{-2}$)	6.0	3.0	2.0

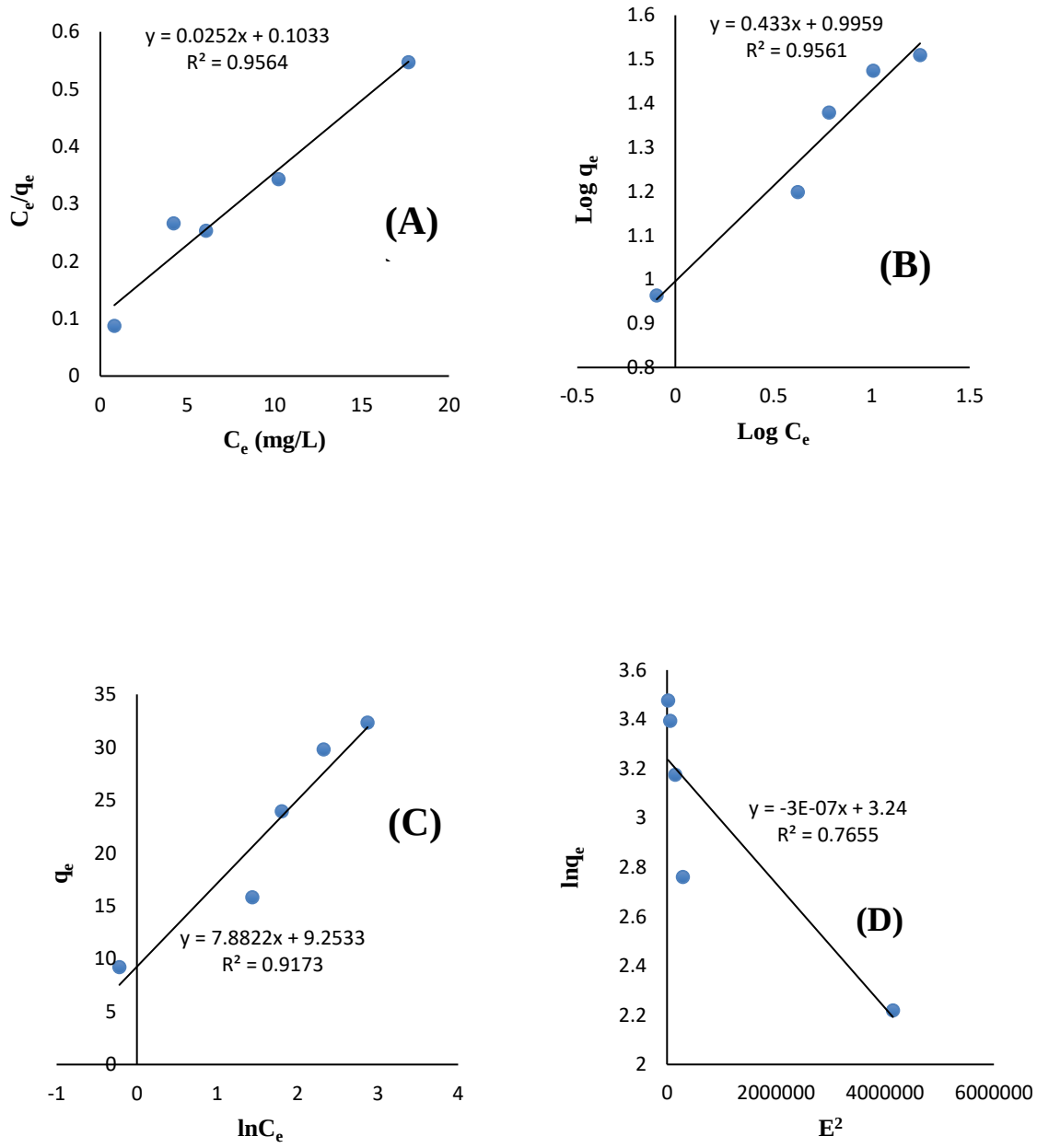

Figure 4.20: (A)Langmuir (B) Freundlich (C)Temkin and (D) D-R linear Isotherm plots for PPAC-CQ System

Table 4.8: Adsorption Isotherm Parameters for uptake of CQ using PPAC at Different Temperatures

	Parameters	303 K	313 K	323 K
Langmuir	q_m (mg/g)	31.9488	34.6020	39.6825
	K_L (l/mg)	0.9072	0.7083	0.2439
	R_L	0.0215	0.0274	0.0757
	R^2	0.9369	0.9909	0.9564
Freundlich	K_f (mg/g(L/mg))$^{1/n}$	16.6839	14.7672	9.9060
	n	4.6728	3.3704	2.3094
	R^2	0.7697	0.8681	0.9561
Temkin	B_T	649.6255	452.0204	319.5988
	K_t	83.6935	16.2498	3.2347
	R^2	0.7719	0.9368	0.9173
D-R	E_a (kJ/mol)	3162.2776	2236.0679	1290.9944
	q_m (mg/g)	28.1937	29.2447	25.5337
	R^2	0.8675	0.9554	0.7655
	β x 10 $^{-7}$(Mol^2.kJ^{-2})	5.0	1.0	3.0

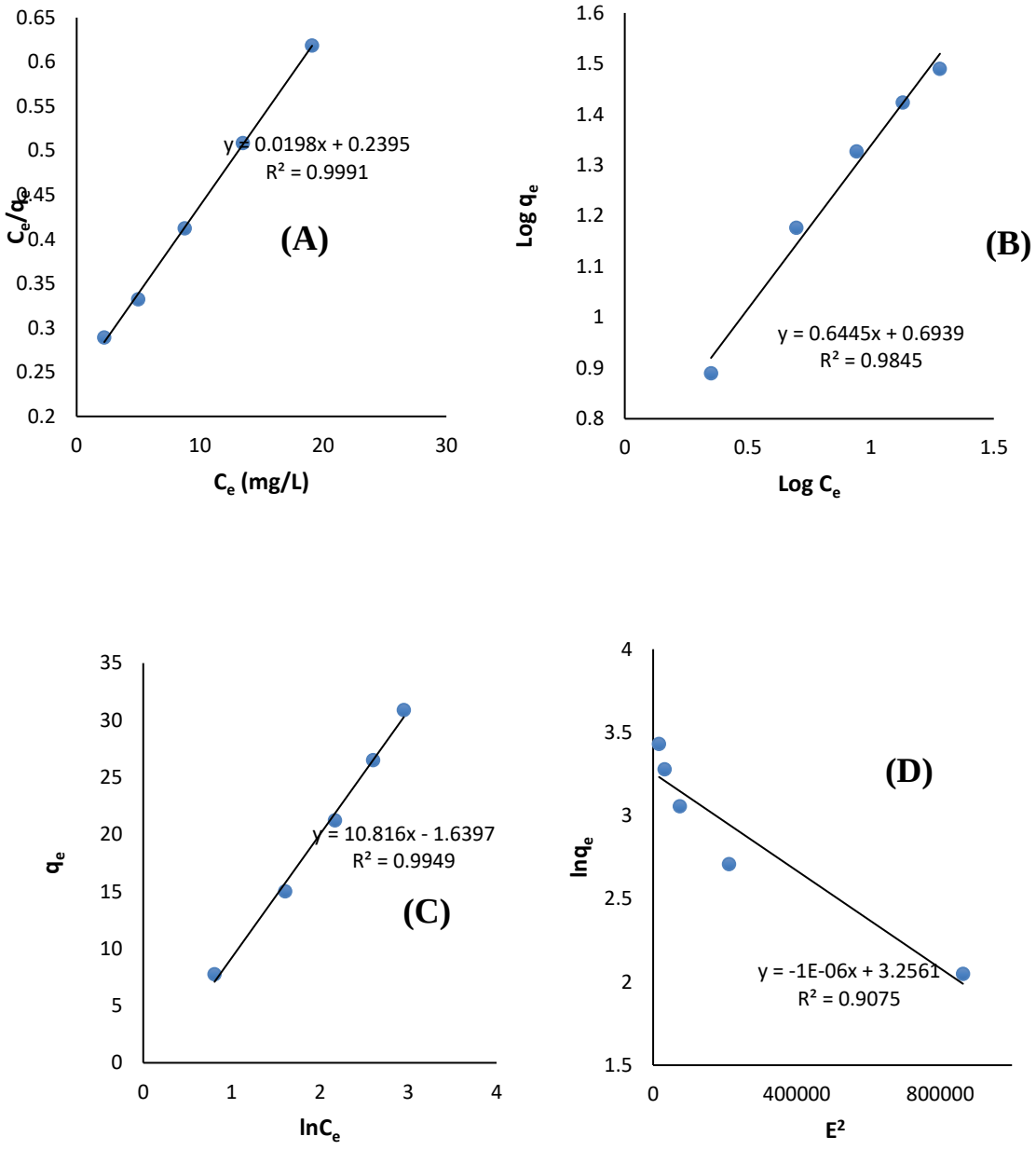

Figure 4.21: (A)Langmuir (B) Freundlich (C)Temkin and (D) D-R linear Isotherm plots for PPAC-ZnO-NC-CQ System

Table 4.9: Adsorption Isotherm Parameters for uptake of CQ using PPAC-ZnO-NC at Different Temperatures.

	Parameters	303 K	313 K	323 K
Langmuir	q_m (mg/g)	35.84	39.52	50.50
	K_L (l/mg)	0.14	0.12	0.08
	R_L	0.12	0.14	0.19
	R^2	0.89	0.98	0.99
Freundlich	K_f (mg/g(L/mg))$^{1/n}$	6.66	5.79	4.94
	n	2.13	1.85	1.55
	R^2	0.94	0.97	0.98
Temkin	B_T	352.46	296.23	232.91
	K_t	1.57	1.15	0.86
	R^2	0.90	0.99	0.99
D-R	E_a (kJ/mol)	0.79	0.71	0.71
	q_m (mg/g)	23.07	24.38	25.95
	R^2	0.86	0.92	0.91
	$B\ x10^{-6}$ ($Mol^2.kJ^{-2}$)	8.0	1.0	1.0

Table 4.10: Maximum Monolayer Adsorption Capacity of Adsorbents in this study in comparison with other agrowastes and nanocomposites for pharmaceutical Uptake.

Pharmaceutical Pollutant	Adsorbent	Q_{max} (mg/g)	Reference
Lumefantrine	Banana Stalk Activated Carbon	102.1	Agboola, Akanji, and Bello, (2021)
Ciprofloxacin	Pomegranate peel	2.353	Elhag-Elhussien, (2017)
Paracetamol	Moringa Olifera Seed pod	17.48	Quesada *et al.*, (2019)
Ciprofloxacin	Potato Stem and Leaves	11.5	Li *et al.*, (2018)
Ibuprofen	Acid modified kolanut husk	39.22	Bello *et al.*, (2021)
Chloroquine	RHAC	54.05	This study
Chloroquine	RHAC-ZnO-NC	169.49	This study
Chloroquine	PPAC	39.68	This study
Chloroquine	PPAC-ZnO-NC	50.50	This study

4.2.3.4 Kinetic Studies

Kinetic studies were carried out in order to investigate the rate of adsorption as well as the adsorbent-adsorbate interactions. Kinetic model plots of the pseudo first order (PFO), pseudo second order (PSO), and Elovich were made as shown in Figures 4.22-4.25. Kinetic model parameters were calculated and outlined in Tables 4.11-4.14. The correlation coefficients R^2 values, sum of square error (SSE) and chi square (X^2) values were used to determine which of the Kinetic models best fit the adsorption process. Also, the closeness of the q_e calculated and q_e experimental values were further used to determine the model of best fit.

The PSO was the kinetic model of best fit for all adsorption systems. The pseudo first order plot of ln q_e-q_t versus time was made. As shown in Tables 4.11-4.14, low SSE values, lower X^2 values and the negligible difference between the q_e calculated and q_e experimented value for all adsorption systems. The R^2 values across all concentrations for the PSO kinetic model was closer to unity than all other kinetic models. R^2 values ranged from 0.98-0.99 across all concentrations. The values of β decreases as concentration increases and the values of α which relates to chemisorption rate was noticed to increase as concentration increases. This indicates that more than one mechanism may govern the uptake. The lower R^2 values obtained for Elovich and PFO kinetic models along with the higher SSE values and higher X^2 values along with the large difference between the q_e calculated and q_e experimental values makes the Elovich and PFO kinetics models not fit for explaining the adsorption data. The kinetic models of best fit therefore followed the order PSO >Elovich > PFO. Similar trend was reported by Spessato *et al.,* (2019) who utilized modified Jatoba seeds for the uptake of paracetamol.

4.2.3.4.1 The Intraparticle Diffusion Model (IPD) Mechanism

The intraparticle diffusion model parameters and plots are shown in Figures 4.22-4.25 and Tables 4.11-4.14. The data of intraparticle diffusion models were deduced from the line equation of the plot of q_t against $t^{1/2}$. Across all initial adsorbate concentrations, the IPD plots did not pass through the origin as can be seen from the non-zero intercept (C) values outlined in Tables 4.11-4.14. The non-zero intercept obtained for nearly all adsorbent-adsorbate interactions suggests that the rate-limiting step is determined by the IPD but apparently may not be the only mechanistic explanation for the CQ uptake (Kumar & Kumaran, 2005; Li *et al.,* 2012). The increase in values of C as concentration increases shows that there was an increase in boundary layer effect as initial concentration increases.

The boundary layer diffusion is another likely mechanism for the diffusion of the pharmaceutical molecules into the adsorbent materials. The values obtained for boundary layer thickness (C) and K_{diff} were observed to increase generally as initial adsorbate concentration increased suggesting a consequent increase in the boundary layer effect. The

capacity of adsorbent material to adsorb or retain CIP and LUMF in solution is greatly influenced by these parameters (Bello *et al.*, 2019).

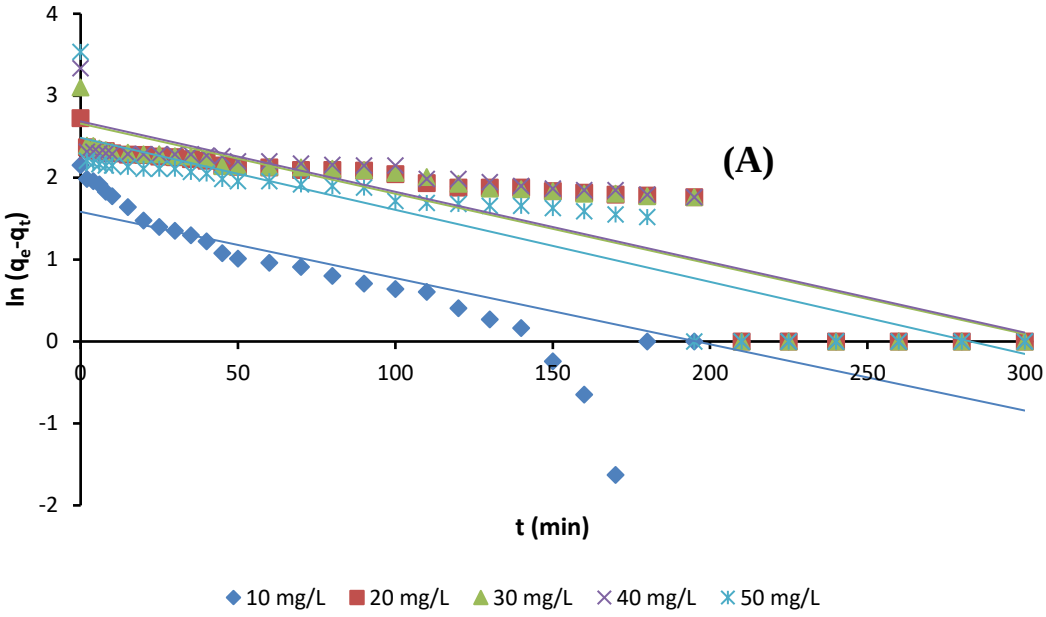

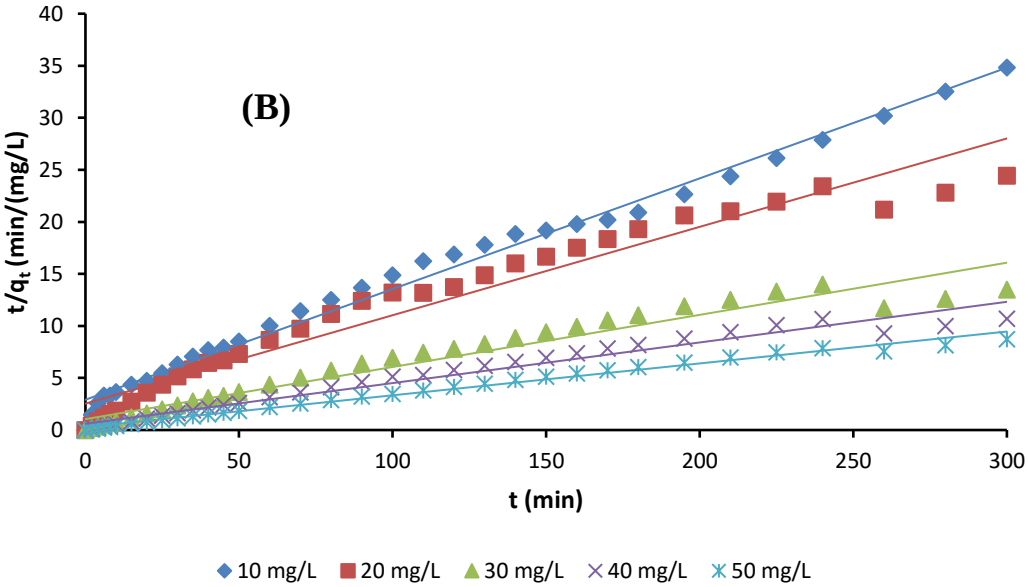

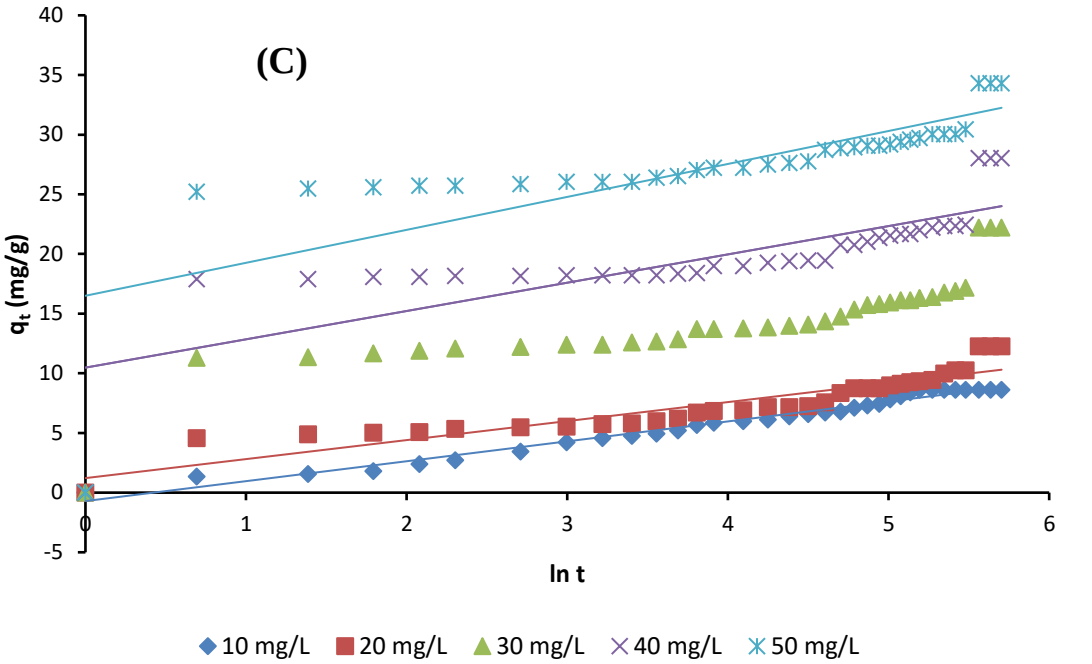

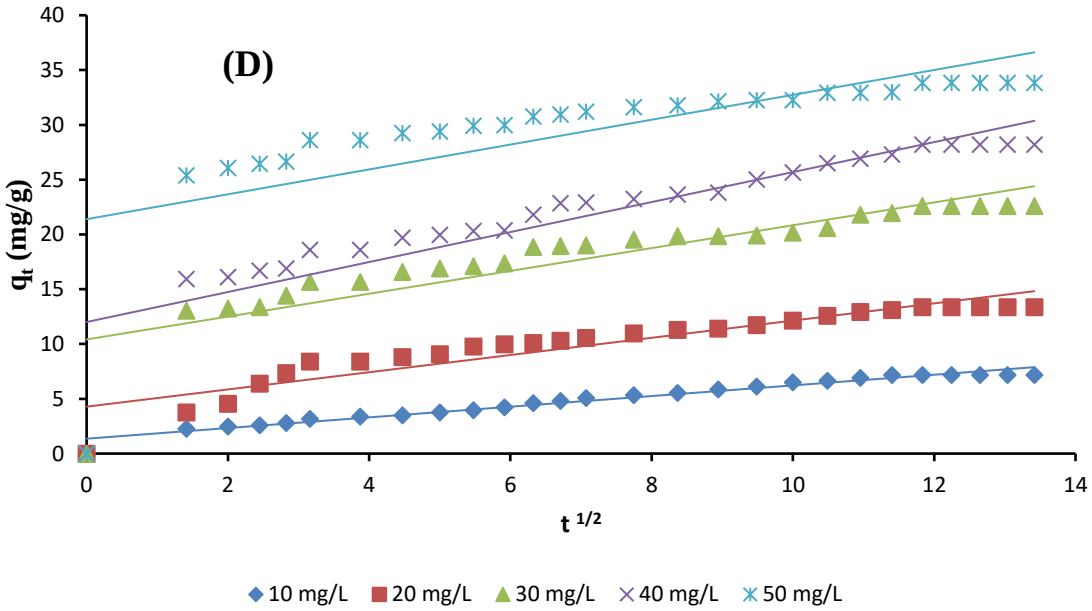

Figure 4.22: Plot of (A) PFO (B) PSO (C) Elovich and (D) IPD for RHAC-CQ system

Table 4.11: Parameters of Kinetic Model for CQ Uptake using RHAC

Model	**Initial CQ concentration (mg/L)**				
	10	20	30	40	50
PFO					
$q_{e(exp)}$(mg/L)	7.169	13.379	22.595	28.216	33.836
$q_{e(cal)}$(mg/L)	4.236	6.526	9.001	13.289	7.023
k_1(min^{-1})	0.012	0.015	0.015	0.017	0.014
R^2	0.723	0.789	0.888	0.789	0.804
SSE (%)	8.606	46.955	184.774	222.781	718.965
X^2	2.031	7.194	20.526	16.763	102.372
PSO					
$q_{e(exp)}$(mg/L)	7.169	13.379	22.594	28.216	33.836
$q_{e(cal)}$(mg/L)	7.861	14.006	23.094	29.069	34.129
k_2($gmg^{-1}min^{-1}$)	0.006	0.006	0.006	0.003	0.009
R^2	0.981	0.994	0.9949	0.993	0.999
SSE (%)	0.478	0.392	0.249	0.729	0.085
X^2	0.061	0.028	0.010	0.025	0.002
Elovich					
B	0.748	0.433	0.324	0.253	0.276
A	1.449	4.888	29.385	28.465	363.861
R^2	0.948	0.975	0.867	0.879	0.641
Intraparticle-Diffusion					
C_1	1.357	4.284	10.418	12.006	21.392
k_{diff}	0.486	0.785	1.042	1.368	1.134
R^2	0.965	0.867	0.761	0.81	0.484

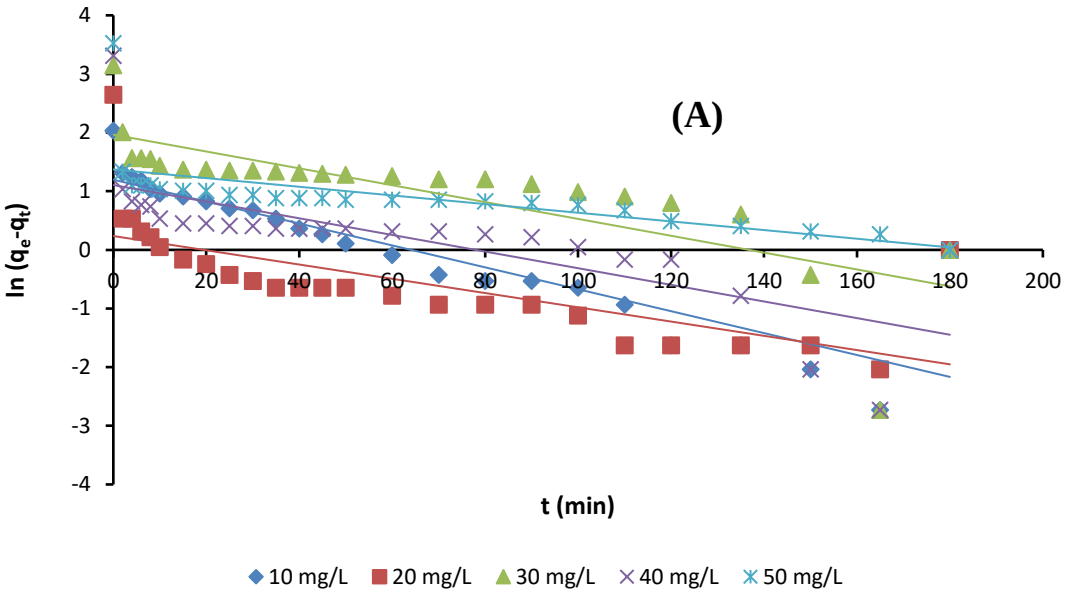
(A)
ln (qe-qt)
t (min)
10 mg/L
20 mg/L
30 mg/L
40 mg/L
50 mg/L

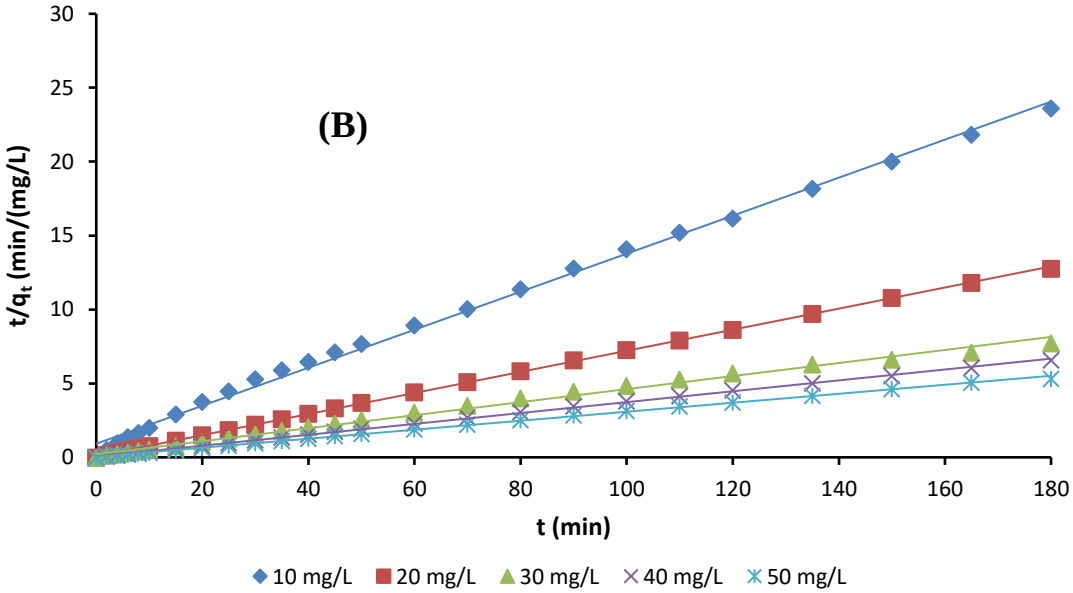
(B)
t/qt (min/(mg/L)
t (min)
10 mg/L
20 mg/L
30 mg/L
40 mg/L
50 mg/L

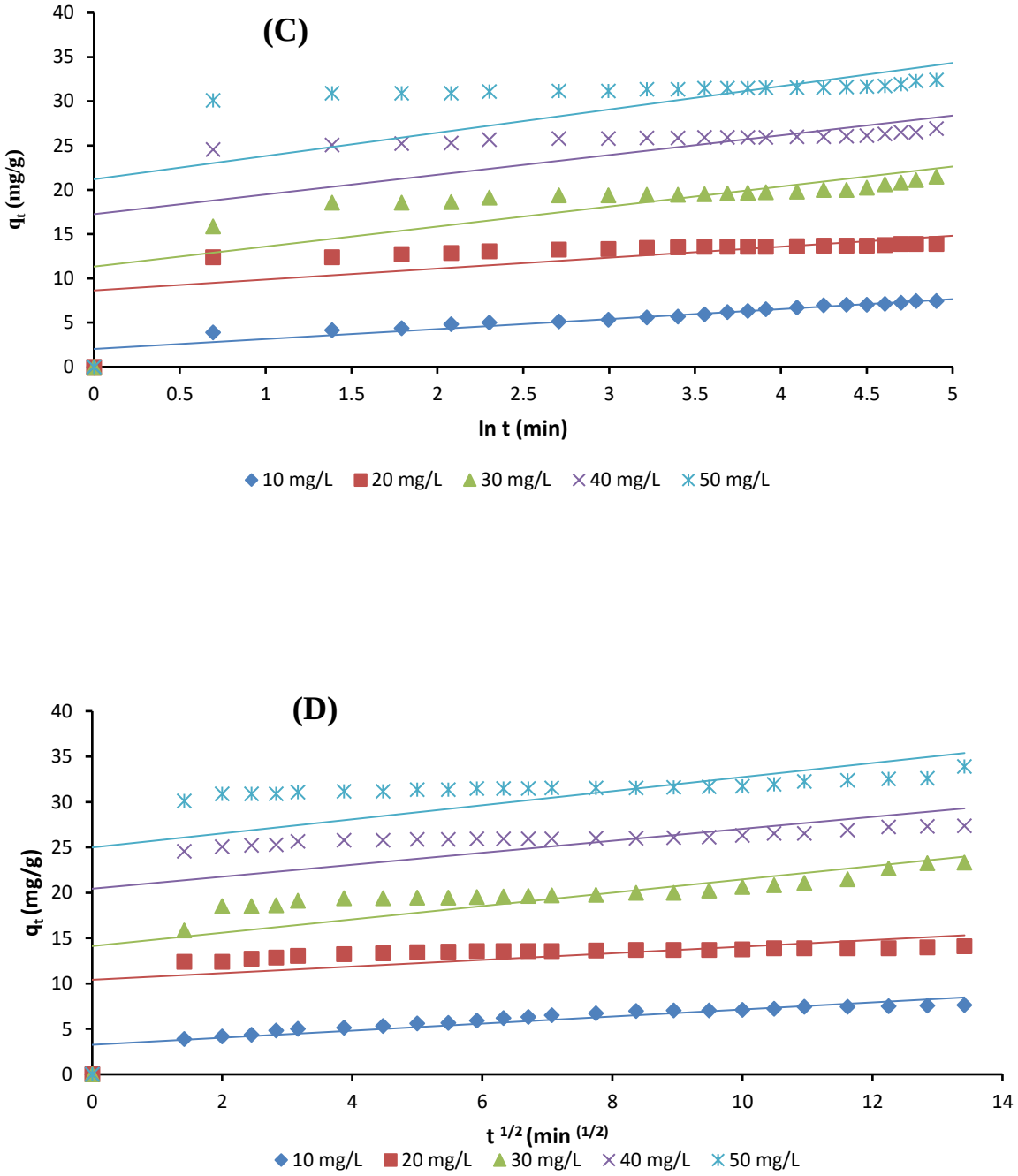

Figure 4.23: Plot of (a) PFO (b) PSO (c) Elovich and (d) IPD for RHAC-CQ system.

Table 4.12: Parameters of Kinetic Model for CQ Uptake using RHAC-ZnO-NC

Model	**Initial CQ concentration (mg/L)**				
	10	20	30	40	50
PFO					
$q_{e(exp)}$(mg/L)	7.627	14.098	23.313	27.366	33.902
$q_{e(cal)}$(mg/L)	3.311	1.266	7.135	3.022	3.942
k_1(min^{-1})	0.018	0.012	0.014	0.014	0.007
R^2	0.785	0.482	0.611	0.554	0.431
SSE (%)	18.624	164.637	261.731	592.604	897.572
X^2	5.623	129.949	36.679	196.061	227.669
PSO					
$q_{e(exp)}$(mg/L)	7.627	14.098	23.314	27.366	33.902
$q_{e(cal)}$(mg/L)	7.776	14.025	22.675	27.173	32.894
k_2($gmg^{-1}min^{-1}$)	0.017	0.069	0.009	0.025	0.021
R^2	0.997	0.999	0.993	0.999	0.999
SSE (%)	0.022	0.005	0.407	0.036	1.014
X^2	0.002	0.0004	0.017	0.001	0.031
Elovich					
B	0.888	0.809	0.442	0.449	0.380
A	6.793	1346.141	339.684	5169.736	8375.086
R^2	0.907	0.415	0.5641	0.366	0.3476
Intraparticle-Diffusion					
C	3.255	10.416	14.125	20.447	24.989
k_{diff}	0.389	0.364	0.734	0.659	0.775
R^2	0.786	0.263	0.432	0.233	0.219

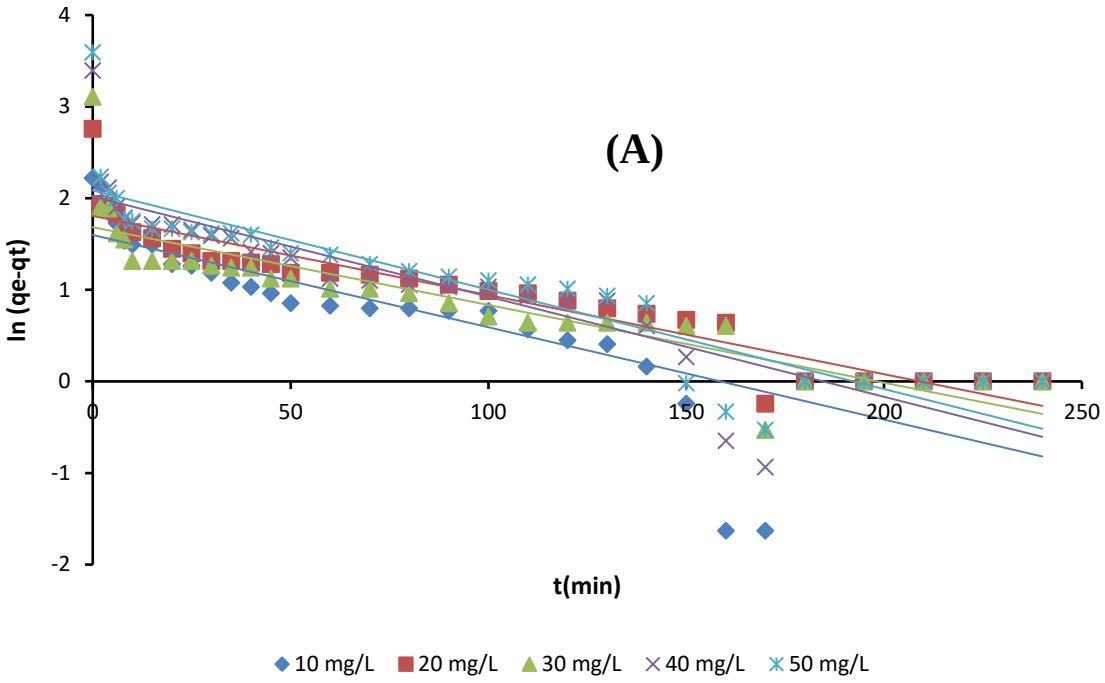
(A)
ln (qe-qt)
t(min)
10 mg/L
20 mg/L
30 mg/L
40 mg/L
50 mg/L

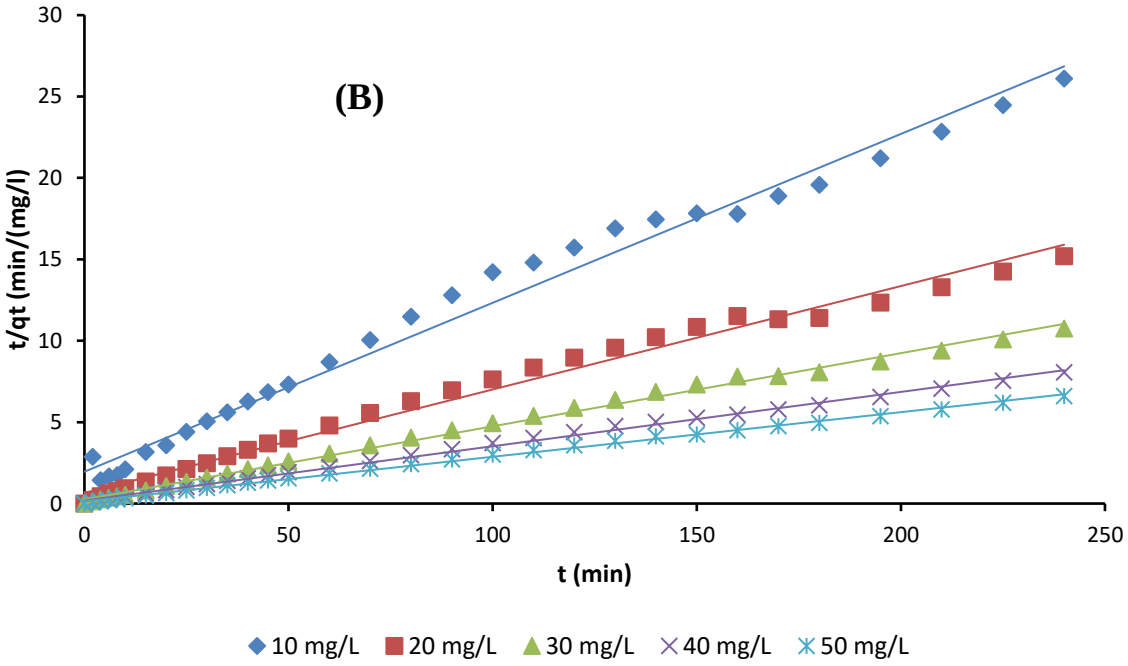
(B)
t/qt (min/(mg/l)
t (min)
10 mg/L
20 mg/L
30 mg/L
40 mg/L
50 mg/L

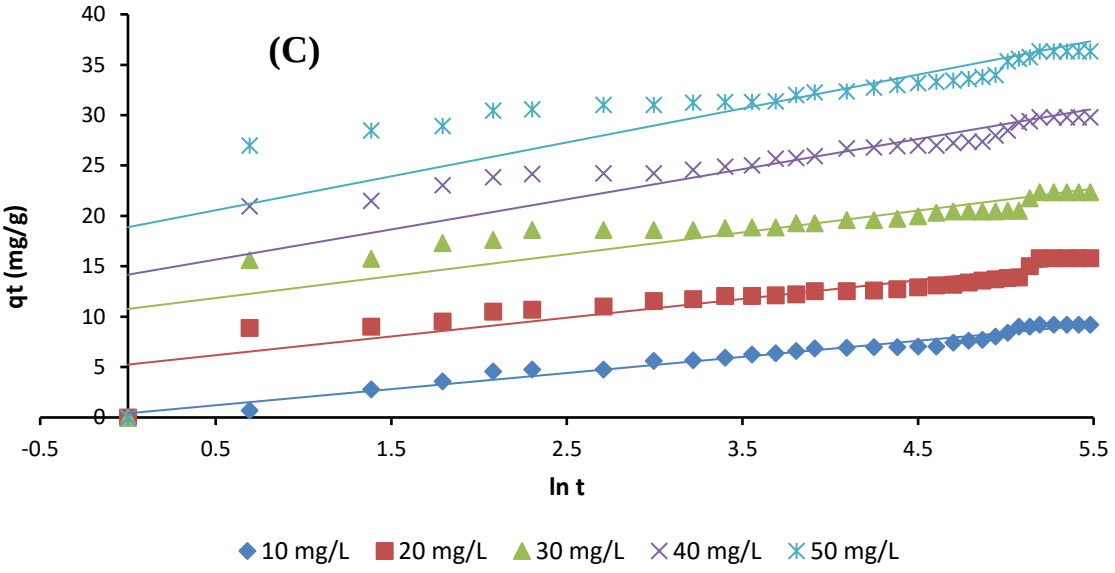

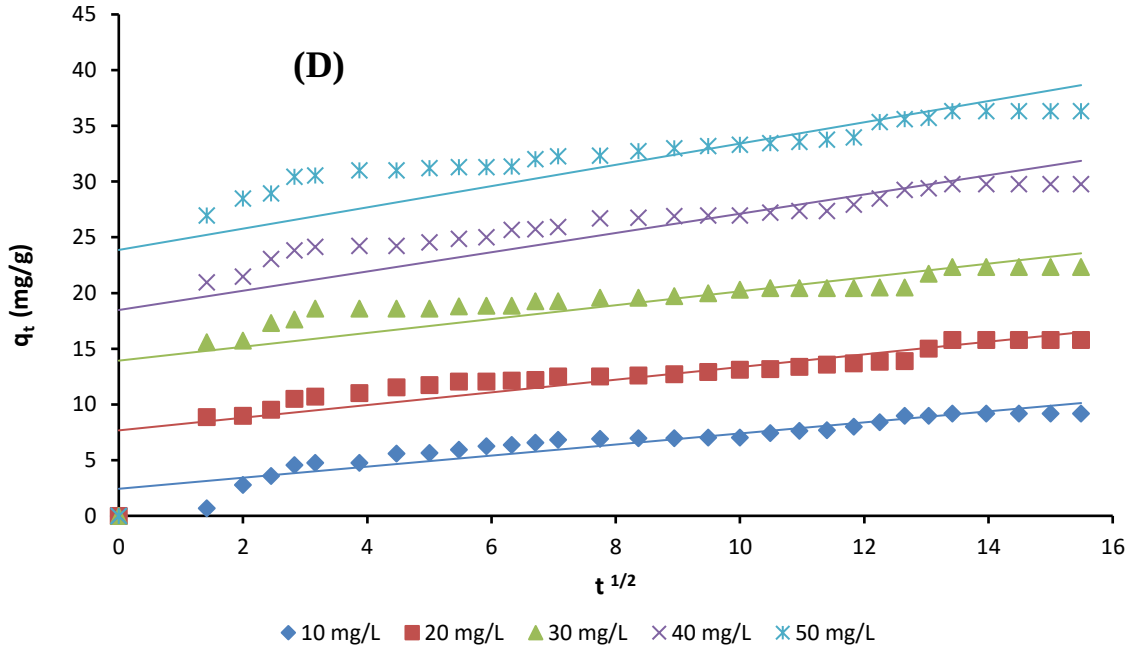

Figure 4.24: Plot of PFO, PSO, Elovich and intraparticle diffusion for PPAC-CQ system.

Table 4.13: Parameters of Kinetic Model for CQ Uptake using PPAC

Model	**Initial CQ concentration (mg/L)**				
	10	20	30	40	50
PFO					
$q_{e(exp)}$(mg/L)	9.196	15.797	22.333	29.784	36.320
$q_{e(cal)}$(mg/L)	4.950	6.091	5.386	7.529	8.050
k_1(min^{-1})	0.010	0.009	0.009	0.011	0.011
R^2	0.688	0.869	0.776	0.797	0.810
SSE (%)	18.028	94.203	287.194	495.293	799.195
X^2	3.642	15.464	53.317	65.781	99.276
PSO					
$q_{e(exp)}$(mg/L)	9.196	15.797	22.333	29.784	36.320
$q_{e(cal)}$(mg/L)	9.643	15.748	20.040	29.940	36.496
k_2($gmg^{-1}min^{-1}$)	0.005	0.006	0.009	0.006	0.0057
R^2	0.984	0.988	0.996	0.997	0.997
SSE (%)	0.199	0.002	5.259	0.024	0.031
X^2	0.021	0.0002	0.262	0.0008	0.0008
Elovich					
B	0.625	0.537	0.461	0.334	0.297
α	2.069	31.278	311.259	341.263	921.245
R^2	0.970	0.823	0.647	0.671	0.594
Intraparticle-Diffusion					
C	2.428	7.669	13.929	18.473	23.867
k_{diff}	0.496	0.568	0.621	0.864	0.954
R^2	0.875	0.720	0.497	0.544	0.447

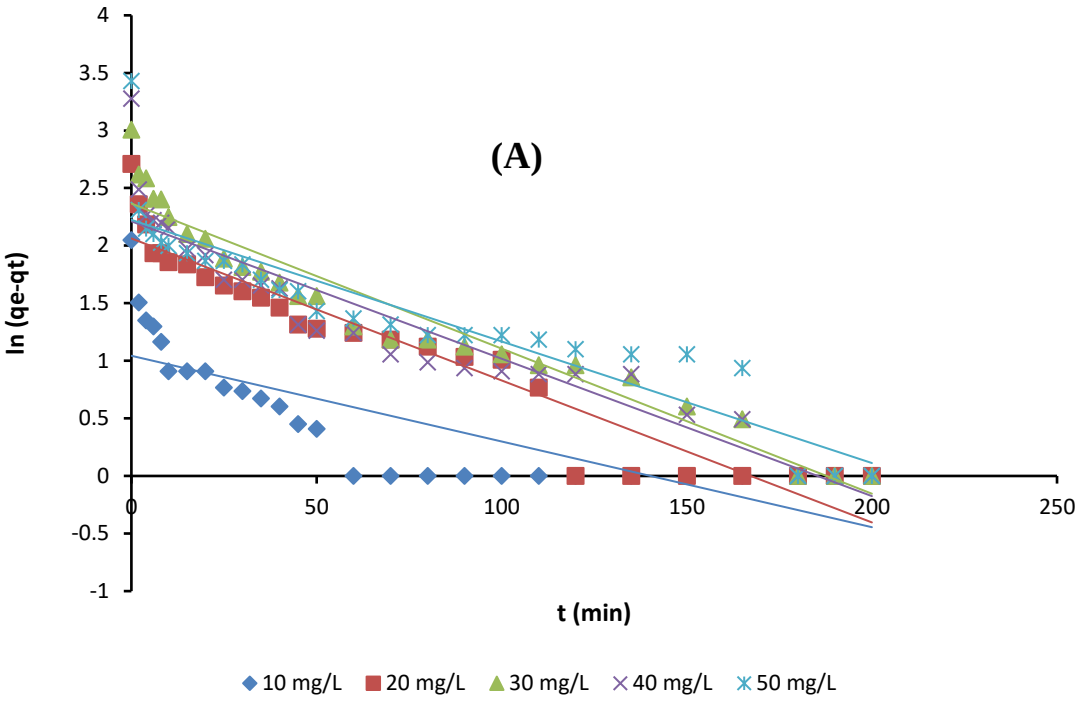
(A)
ln (qe-qt)
t (min)
10 mg/L
20 mg/L
30 mg/L
40 mg/L
50 mg/L

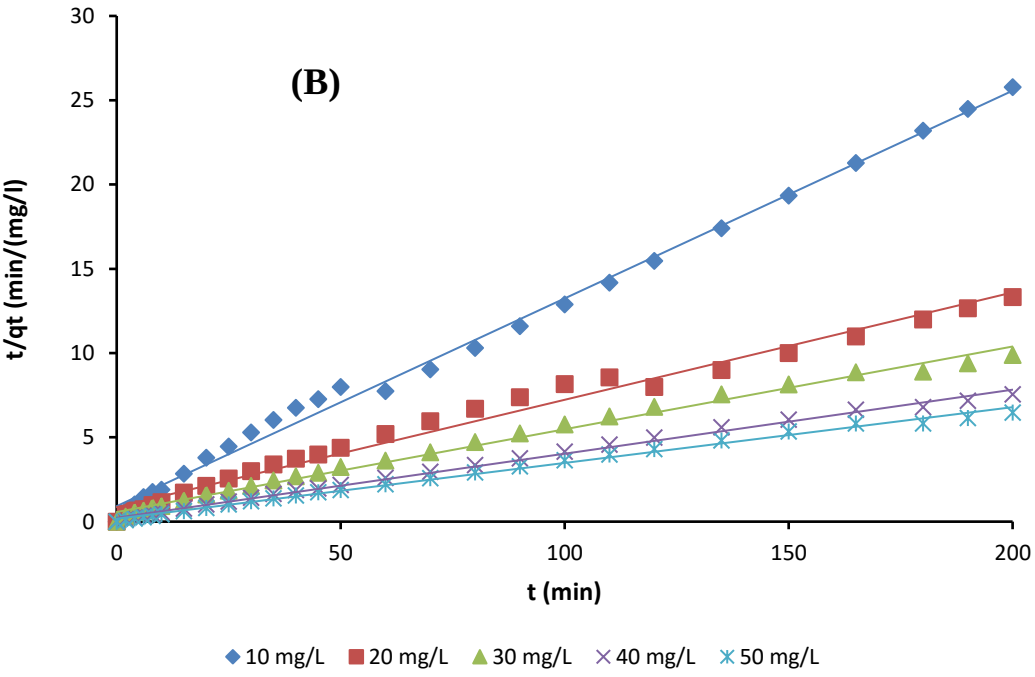
(B)
t/qt (min/(mg/l)
t (min)
10 mg/L
20 mg/L
30 mg/L
40 mg/L
50 mg/L

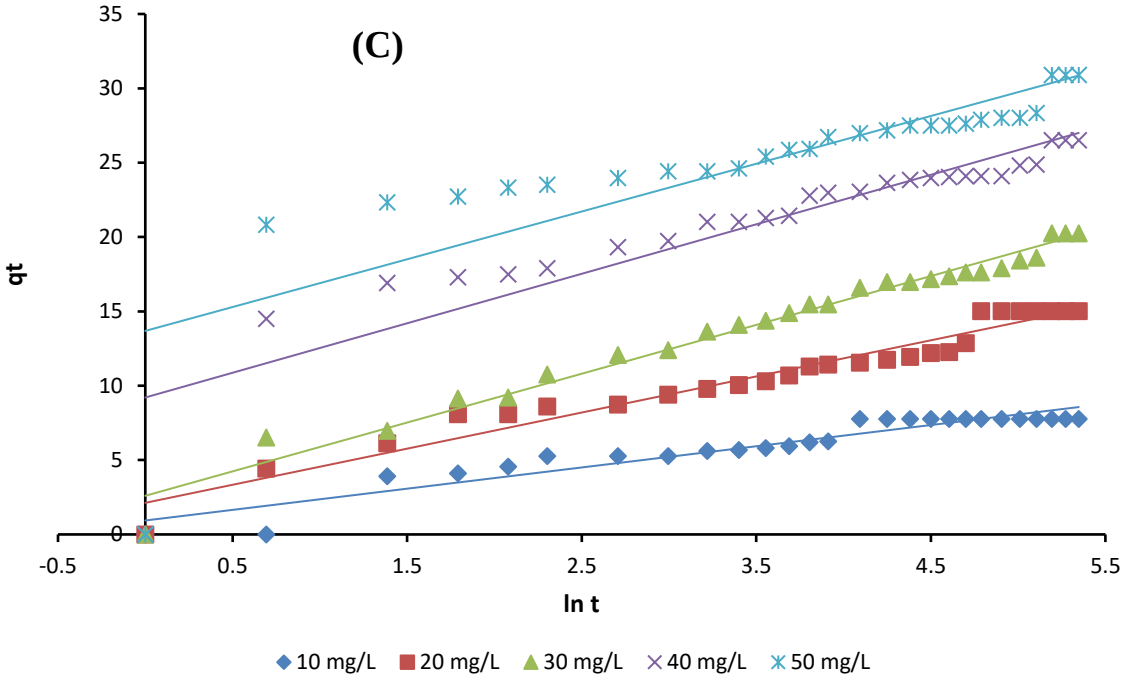

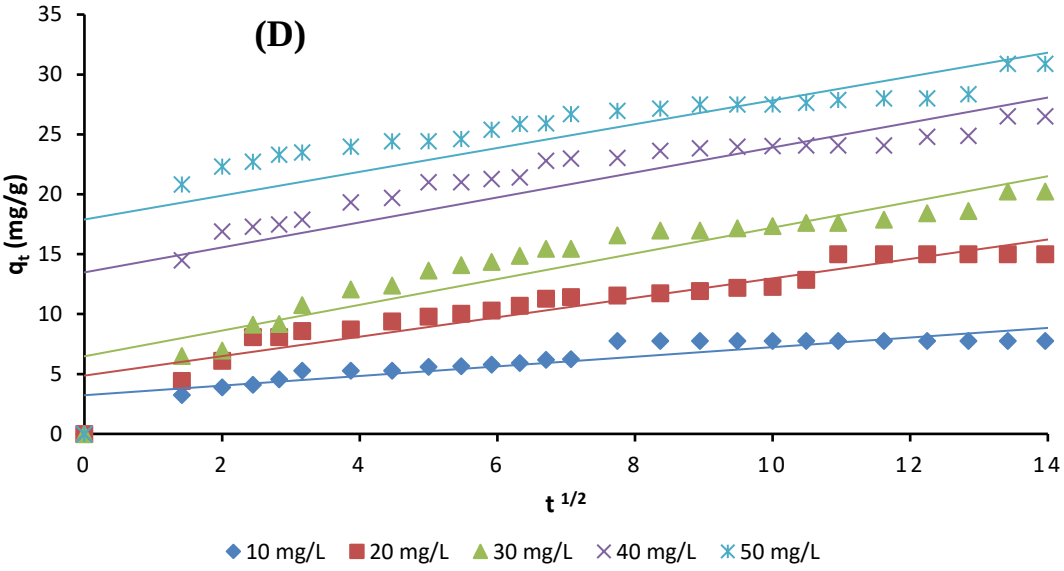

Figure 4.25: Plot of (a)PFO (b)PSO (c) Elovich and (d) Intraparticle diffusion for PP-ZnO-NC-CQ system

Table 4.14: Parameters of Kinetic Model for CQ Uptake using PPAC-ZnO-NC

Model	**Initial CQ concentration (mg/L)**				
	10	20	30	40	50
PFO					
$q_{e(exp)}$(mg/L)	7.758	15.013	20.241	26.516	30.895
$q_{e(cal)}$(mg/L)	2.839	7.865	10.649	9.126	9.241
k_1(min^{-1})	0.007	0.012	0.012	0.012	0.011
R^2	0.643	0.913	0.934	0.878	0.828
SSE (%)	24.196	51.086	92.015	302.401	468.894
X^2	8.522	6.494	8.640	33.134	50.738
PSO					
$q_{e(exp)}$(mg/L)	7.758	15.013	20.241	26.516	30.895
$q_{e(cal)}$(mg/L)	8.116	15.698	20.366	26.315	30.211
k_2($gmg^{-1}min^{-1}$)	0.016	0.005	0.004	0.006	0.006
R^2	0.995	0.985	0.992	0.996	0.994
SSE (%)	0.128	0.469	0.016	0.04	0.467
X^2	0.015	0.029	0.00076	0.0015	0.015
Elovich					
β	0.797	0.411	0.305	0.301	0.311
α	4.796	5.824	7.246	52.968	227.878
R^2	0.916	0.962	0.976	0.833	0.676
Intraparticle-Diffusion					
C_1	2.786	4.8652	6.477	13.48	17.893
k_{diff}	0.444	0.8113	1.073	1.042	0.994
R^2	0.724	0.8741	0.860	0.674	0.535

4.2.3.5 Thermodynamic Studies

Thermodynamic studies were carried out to further understand the feasibility, nature and spontaneity of the adsorption. The enthalpy, entropy and Gibbs free energy were calculated. Thermodynamic parameters were evaluated using the ΔG, ΔH and ΔS values as shown in Figure 4.26 and Table 4.15-4.18. the Enthalpy values (ΔH) values give an idea of the nature of the adsorption, the entropy values (ΔS) give an idea on the feasibility while the Gibbs free energy values (ΔG) give an idea on the spontaneity of the adsorption. The amount of CQ removed by RHAC, RHAC-ZnO-NC, PPAC and PPAC-ZnO-NC between temperatures 303 K – 323K were obtained from the linear plot of $ln\ K_L$ against the reciprocal of temperature T (K). Figure 4.26 shows the Van't Hoff plot where the thermodynamic parameters were calculated from.

For all adsorption systems, negative ΔG values were obtained showing that all adsorption processes were spontaneous. The observed increase in the value of ΔG with increase in temperature implies that temperature rise has a significant impact on the thermodynamics. Positive values were obtained for ΔS which indicates that there was an increase in randomness at the adsorbent-adsorbate interface. The positive ΔH values however indicated that the adsorption processes were endothermic in nature. Similar trend in thermodynamic parameters was observed by Quesada *et al.,* (2019) who reported on the uptake of acetaminophen onto modified *Moringa Olifera* Seed Husk.

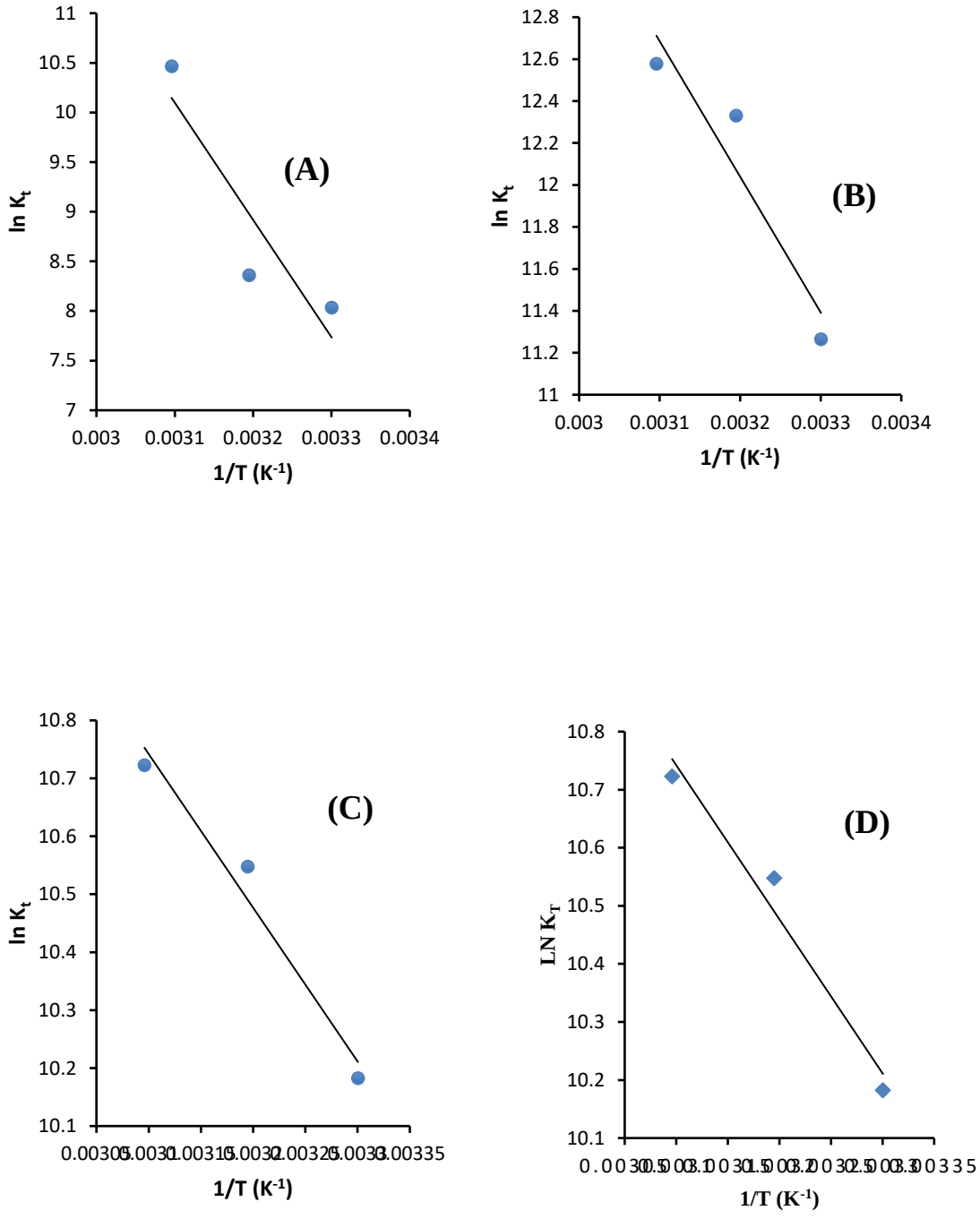

Figure 4.26: Van't Hoff Plot for (a) RHAC-CQ System and (b) RHAC/ZnO-CQ System (C) PPAC-CQ and (D) PPAC-ZnO-NC

Table 4.15: Outlined Thermodynamics Data for the Adsorption of CQ onto RHAC

Temp(*K*)	**ΔG(kJ/mol)**	**ΔH(kJ/mol)**	**ΔS(J/mol)/K)**	**E_a (kJ/mol)**
303	-20.234	98.188	388.338	100.707
313	-21.754			100.790
323	-28.103			100.873

Table 4.16: Outlined Thermodynamics Data for the Adsorption of CQ onto RHAC-ZnO-NC

Temp(*K*)	**ΔG(kJ/mol)**	**ΔH(kJ/mol)**	**ΔS (J/mol)/K)**	**E_a (kJ/mol)**
303	-26.583	33.721	198.031	36.240
313	-27.612			36.323
323	-30.585			36.407

Table 4.17: Outlined Thermodynamics Data for the Adsorption of CQ onto PPAC

Temp(*K*)	**ΔG(kJ/mol)**	**ΔH(kJ/mol)**	**ΔS(J/mol)/K)**	**E_a (kJ/mol)**
303	-28.377	53.773	272.167	56.292
313	-32.087			56.375
323	-33.777			56.458

Table 4.18: Outlined Thermodynamics Data for the Adsorption of CQ onto PPAC-ZnO-NC

Temp(*K*)	**ΔG(kJ/mol)**	**ΔH(kJ/mol)**	**ΔS(J/mol)/K)**	**E_a (kJ/mol)**
303	-25.651	22.057	157.691	24.577
313	-27.448			24.660
323	-28.795			24.743

4.3. Malachite Green Adsorption Studies.

4.3.1 Maximum Adsorption wavelength (λ_{max}) for Malachite Green

The maximum absorption peak of malachite green is shown in the Figure 4.27. This peak was obtained when a known concentration of MG solution was scanned between 400 - 800 nm. The maximum absorbance was obtained at 617 nm and as such, the residual concentration after each adsorption was determined at this wavelength.

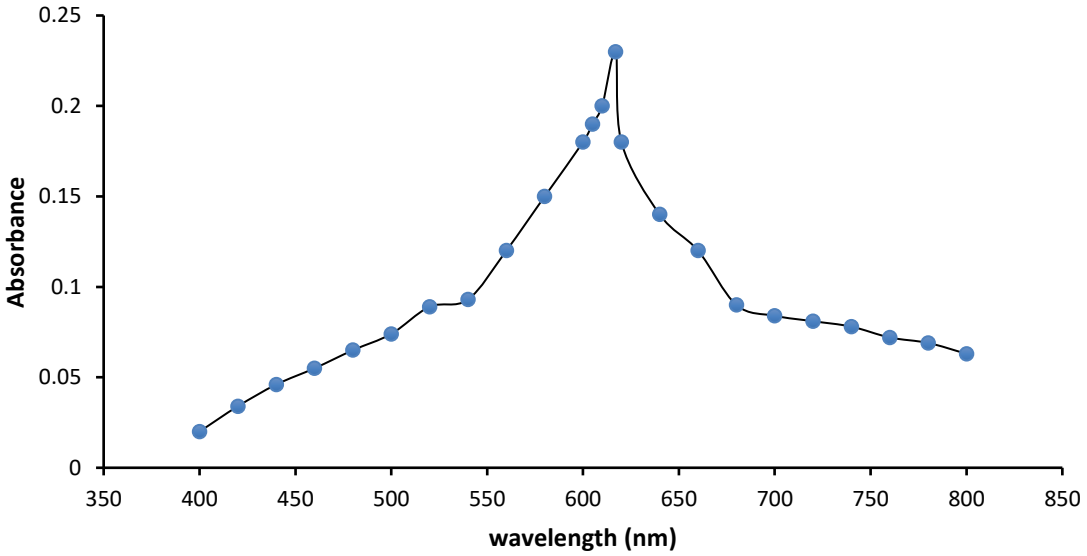

Figure 4.27: The absorbance spectrum of Malachite green (λmax= 617 nm)

4.3.2 Calibration Curve for Malachite Green

Shown in Figure 4.28 is the calibration curve for MG dye. This was obtained by varying dye concentrations from the dye from 10 to 50 mg/L at a constant wavelength of 617 nm. A plot of absorbance versus concentrations was constructed and the R^2 (Correlation Coefficient) value obtained implies the linearity of the calibration curve. The plot obtained was used to determine the residual concentrations of the MG dye during the adsorption process.

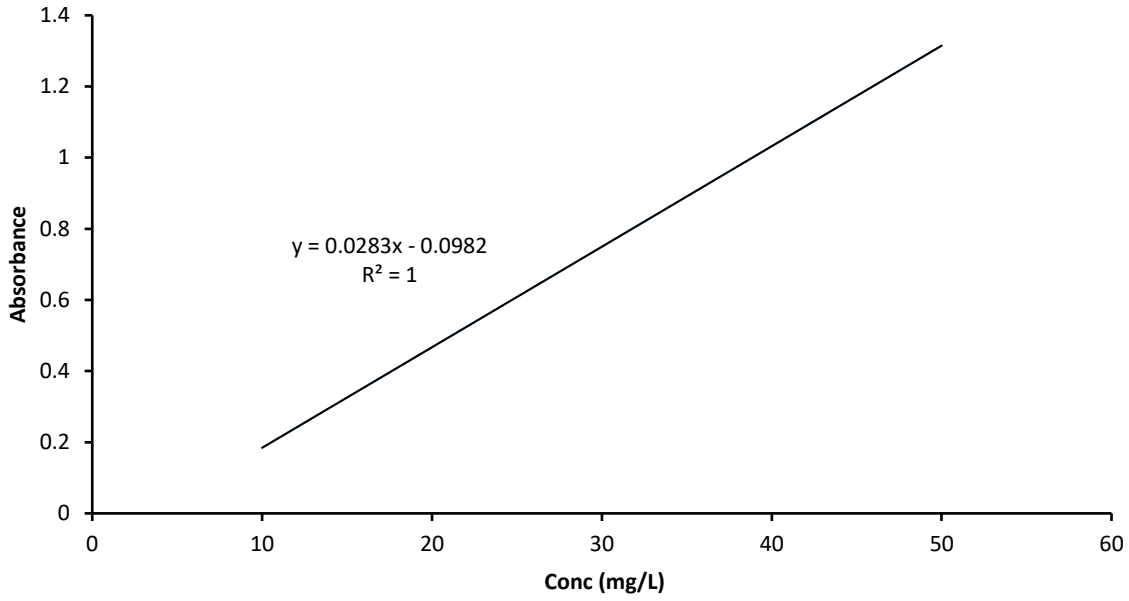

Figure 4.28: Calibration Curve for MG adsorption

4.3.3 Adsorption Studies of Malachite Green Dye onto RHAC, PPAC, RHAC-ZnO-NC and PPAC-ZnO-NC.

4.3.3.1 Effects of Contact Time, Initial Concentration and Temperature

The effects of initial concentration and contact time for the sorption of MG were observed and are shown in Figures 4.29-4.32. A plot of quantity adsorbed (qt) versus time (t) was made monitor the effects initial concentration and time has on the adsorption system. For uptake of MG onto RHAC, RHAC-ZnO-NC, PPAC and PPAC-ZnO-NC, the adsorption process was rapid for the first 40 minutes. This could be as a result of the presence of more active sites for adsorption at the initial stages. The uptake then gradually became slower until equilibrium was attained between 180-240 minutes. This decline could be as a result of adsorbent-adsorbate interferences thereby making adsorbent sites unavailable for adsorption.

Also, for all adsorption systems, as the initial concentration increased, it was observed that the quantity of MG dye adsorbed at specific time (Qt) increased. This could be as a result

of the increase in initial concentration gradient at higher initial MG concentration. Leading to an increase in the driving force which helped to overcome mass transfer resistance leading to rapid uptake of MG dye molecules. At equilibrium point, the amount of MG dye adsorbed by RHAC, RHAC-ZnO-NC, PPAC and PPAC-ZnO-NC at initial concentration of 10 mg/L was 6.3 mg/L, 6.0 mg/L, 6.3 mg/L and 6.4 mg/L respectively, while at initial concentration of 50 mg/L, amount of MG adsorbed was 33.6 mg/L, 35.5 mg/L, 36.2 mg/L and 32.1 mg/L respectively. Similar trend was reported by Ojediran *et al.,* (2020) which reported on the uptake of MG dye onto functionalized maize cob. For all adsorption systems, increase in temperature generally led to an increase in uptake of MG molecules as shown in Figure 4.33. This observed trend could be as a result of availability of more adsorption sites at higher temperatures. Guechi & Hamdaoui, (2016) observed a similar trend in the uptake of malachite green dye onto potato peel.

.

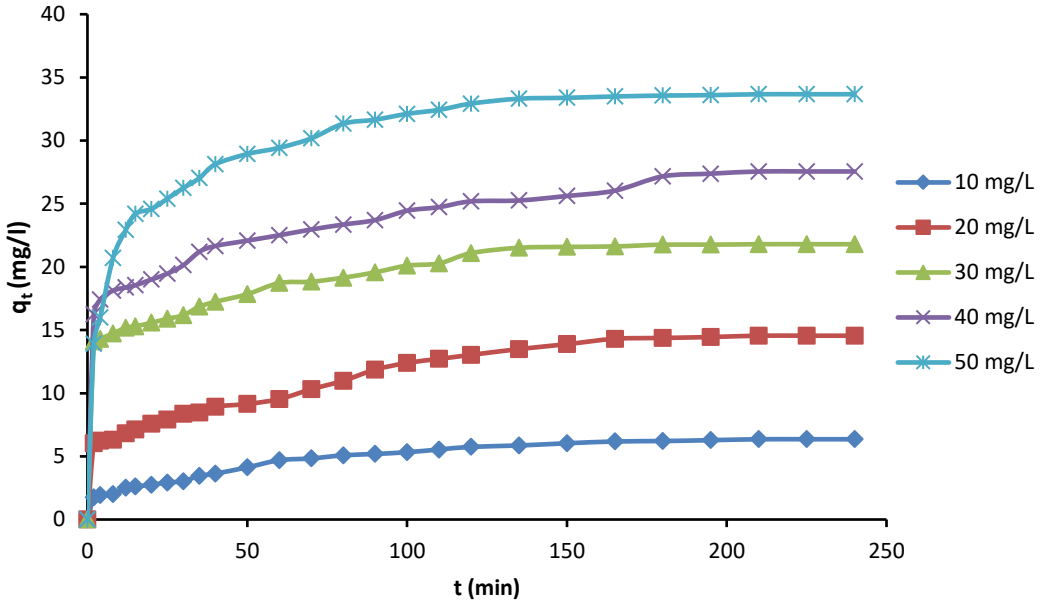

Figure 4.29: Effects of Concentration and Time for RHAC-MG adsorption System.

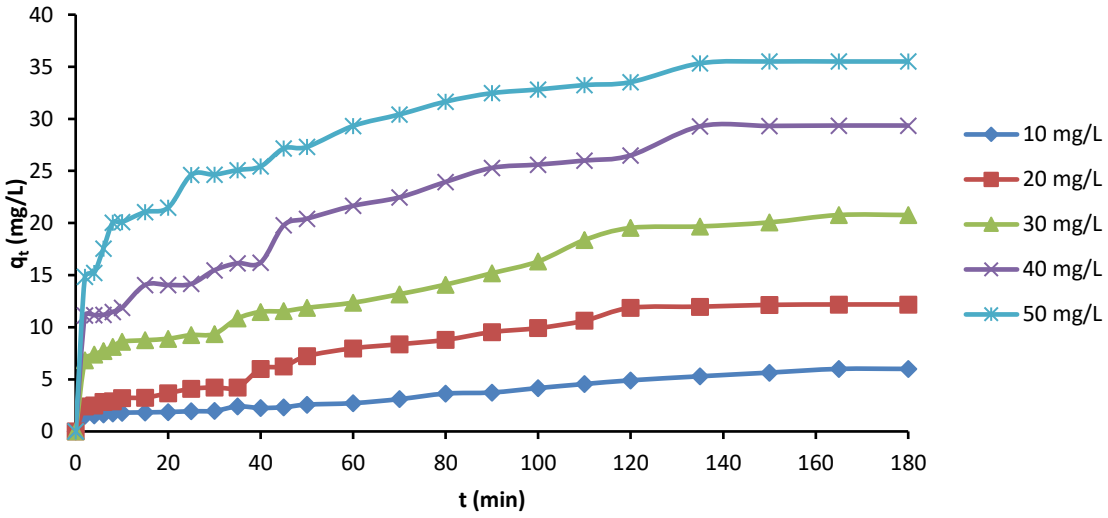

Figure 4.30: Effects of Concentration and Contact time for uptake of MG onto RHAC-ZnO

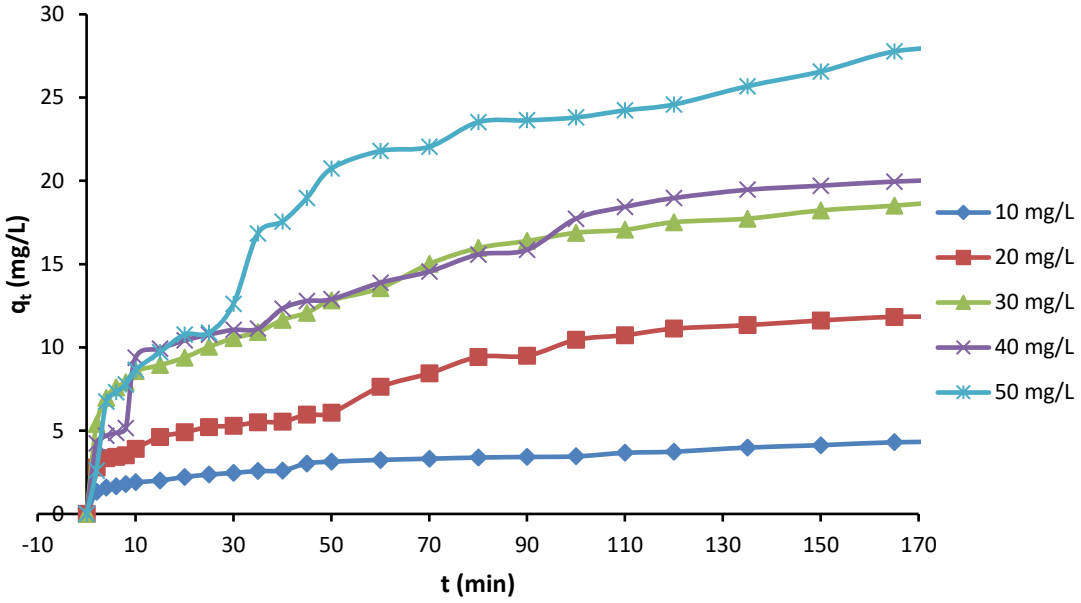

Figure 4.31: Effects of Concentration and Contact time on the uptake of MG by PPAC

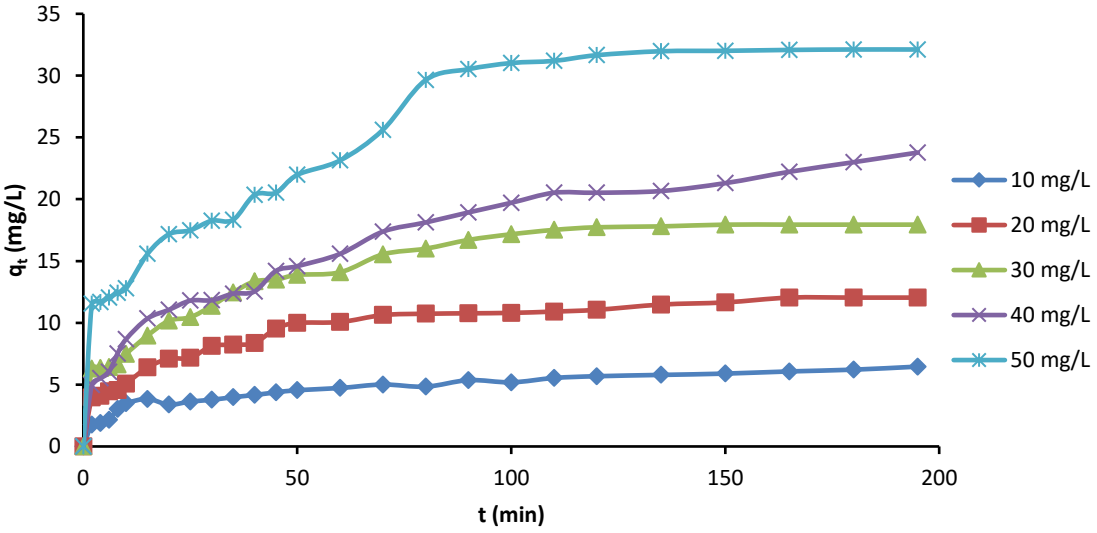

Figure 4.32: Effects of initial concentration and contact time for the uptake of MG onto PPAC-ZnO-NC

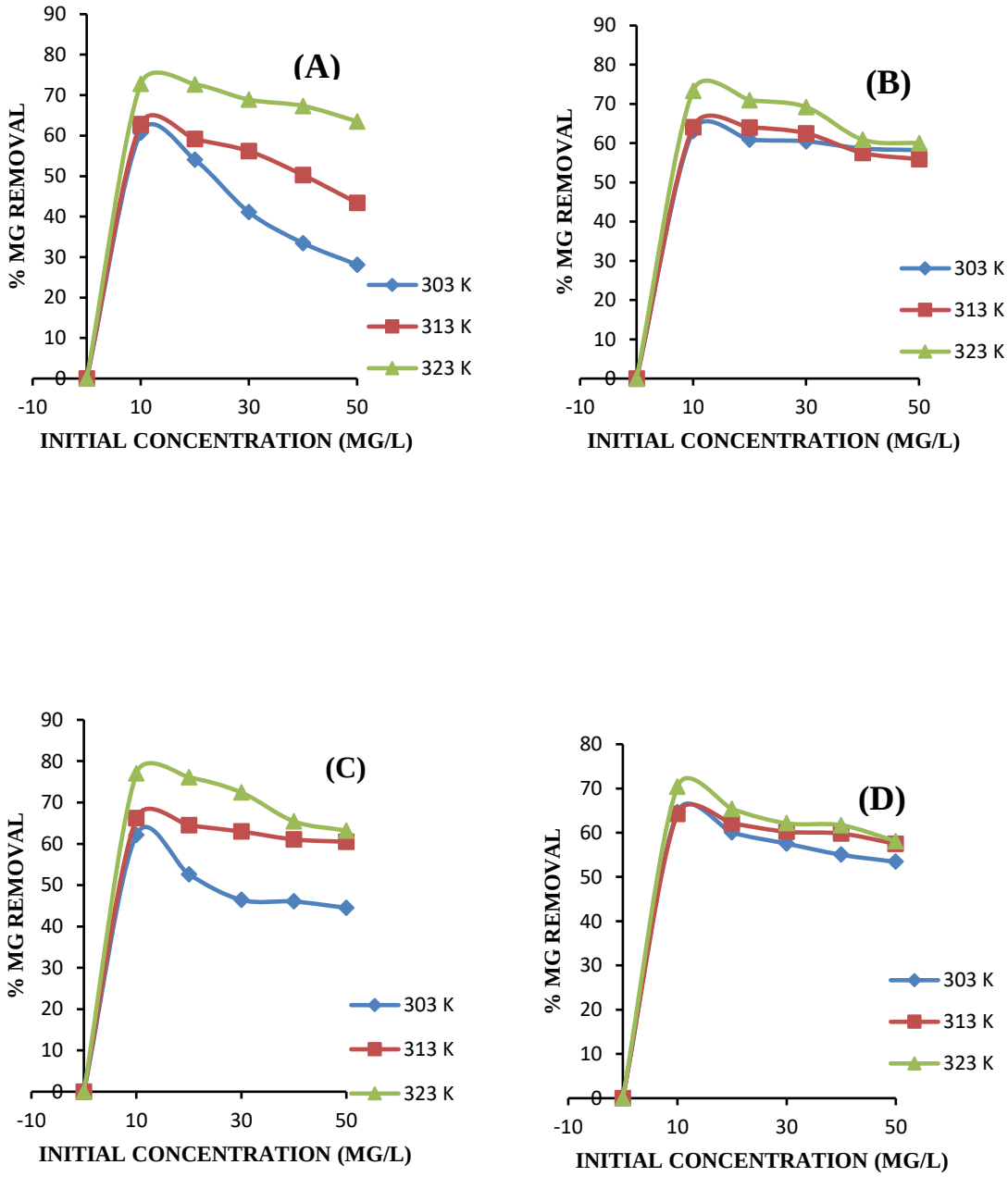

Figure 4.33: Effects of Temperature on MG uptake onto (A)RHAC (B)RHAC-ZnO-NC (C) PPAC (D)PPAC-ZnO-NC

4.3.3.2 Effects Of pH

Figure 4.34 shows the effect solution pH has on the uptake of MG by all adsorbents. This was carried out at pH values ranging from pH 3-11 to observe which has the best percentage removal. As a basic dye, MG forms cations in solution. Therefore as pH increases, the structural component and colour intensity of MG dye is pH dependent (Choudhary *et al.*, 2020).

RHAC and PPAC had the highest percentage removal of 84.2 % and 86.4 % at pH 9 while RHAC-ZnO-NC and PPAC-ZnO-NC had the highest percentage removal of 88.1 % and 87.9 % at pH 7. The pH of highest percentage removal could be as a result of the existence of negative charges on the surface of adsorbents at pH values are higher than pH_{pzc} which results in the attraction between adsorbent surface and MG molecules resulting in an increase in uptake at this region (Mudyawabikwa *et al.*, 2017). However, at pH values lower than the pH point of zero charge, the surface of the adsorbent becomes positively charged which causes a repulsion between MG molecules and adsorbent surfaces, thereby reducing the MG uptake in this region as can be observed in Figure 4.34. Wang *et al.*, (2017) observed and reported similar results on the adsorption of MG dye onto natural zeolite.

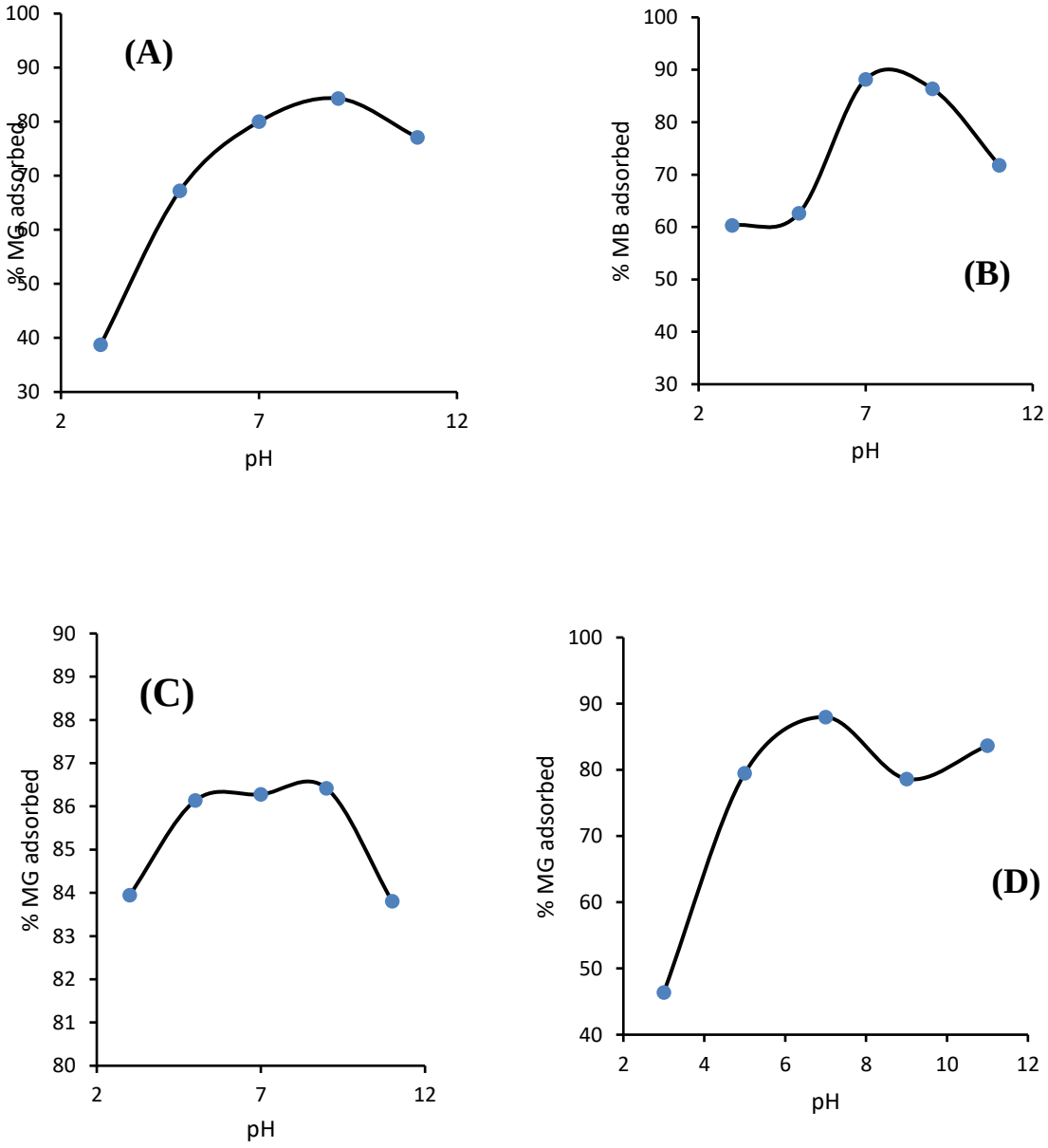

Figure 4.34: Percentage of MG Adsorbed by (A) RHAC (B) RHAC-ZnO-NC (C) PPAC and (D) PPAC-ZnO-NC at Different pH

4.3.3.3 Isotherm Studies

Isotherm studies were carried out to further understand the nature of the adsorbent-adsorbate interactions for all adsorption systems. The data obtained from the various

adsorption isotherm models (Freundlich, Langmuir, Temkin and Dubunin-Radushkelvich) considered in this study are shown in Figures 4.35 - 4.38 and outlined in Tables 4.19-4.22.

4.2.3.4.1 RHAC-MG Adsorption System

The adsorption data for sorption of MG onto RHAC was plotted using the Langmuir, Freundlich, Temkin and D-R isotherms as shown in Table 4.19 and Figure 4.35. The Langmuir isotherm plot and parameters are shown in Figure 4.32(A) and Table 4.19 respectively. R^2 value of 0.94 was obtained while the separation factor R_L value of less than 1 (0.16) suggesting its favourability was obtained (Ahmad *et al.,* 2020; Muinde *et al.,* 2020). The maximum monolayer adsorption (q_{max}) however was calculated as 58.14. The Freundlich isotherm was obtained by plotting a graph of log q_e versus log C_e. (As shown in Figure 4.35B). R^2 value of 0.99 was obtained while the K_F and n values of 2.4 and 1.3 respectively was obtained. These values suggest the favourability of the adsorption process. The adsorption data was also found to fit the Freundlich isotherm. Temkin isotherm was considered by plotting q_e versus ln C_e (Figure 4.35C). High b_t value (259.58) was obtained. The positive B_T values across all temperatures describes the nature of the heat of adsorption as endothermic. K_t value of 2.19 was obtained and the high R^2 value (0.97) showed that the Temkin isotherm could describe the nature of the sorption process. The D-R plot of ln q_e versus E^2 was also made. The Q_{max} obtained was low (21.47 mg/g) in comparison to the Langmuir q_{max}. The low R^2 value of 0.88 was obtained however, the E value (0.41 kJ/mol) which is less than 8 kJ/mool suggests physiosorption (Guechi & Hamdaoui, 2016).

4.2.3.4.2 RHAC-ZnO-NC-MG system

From the adsorption data obtained, a plot of C_e/q_e against C_e was made for the Langmuir isotherm (as shown in Figure 4.36A). The maximum adsorption capacity of 48.78 mg/g was obtained for uptake of CQ onto RHAC-ZnO-NC at 323 K with R^2 value of 0.93. The separation factor (R_L) value of less than 1 (0.17) was obtained for all temperatures investigated and this suggests the favourability of the sorption process (Dada *et al.,* 2020; Inyinbor *et al.,* 2016). The Freundlich Isotherm (as shown in Table 4.20) however has an R^2 value of 0.99 and the n values calculated at all temperatures were greater than 1 which suggests that the interaction is favourable, simple and physical (Bello *et al.,* 2019). The

higher R^2 obtained from the Temkin isotherm (0.94) suggests that adsorbate-adsorbent interaction may have participated in the uptake of MG by RHAC-ZnO-NC. The positive B_T values across all temperatures describes the nature of the heat of adsorption as endothermic. E values of the D-R isotherm were lower than 8 kJ/mol which suggests physio sorption. However, the q_m values obtained from the D-R plot were low compared to those obtained from the Langmuir plot and therefore cannot be used to describe the sorption process (Gündüz & Bayrak, 2017).

4.2.3.4.3 PPAC-MG system

Figure 4.37 and Table 4.21 shows the Isotherm plots and parameters for the uptake of MG onto PPAC. The R_L value from the Langmuir Isotherm was found to be 0.3 (less than 1) which implies that the uptake of CQ onto PPAC is favourable. The maximum monolayer adsorption capacity (q_{max}) was found to be 52.35 mg/g with a 0.99 as R^2 value. The Freundlich adsorption Isotherm had a high R^2 value of 0.98, therefore implying that heterogenous adsorption took place. All n values were greater than 1 implying that the uptake is physical and favourable. For the Temkin isotherm, the high R^2 value obtained (0.99) suggests the presence of adsorbate-adsorbent interaction in the sorption process. The D-R plot gave a low R^2 value (0.89). The adsorption Energy lower than 8 kJ/mol was obtained showing that the sorption CQ was physio-sorption.

4.2.3.4.4 PPAC-ZnO-NC-MG system

For the PPAC-ZnO-NC-CQ system, Langmuir Isotherm plot and parameters are shown in Table 4.22 and Figure 4.38A. The R_L value was found to be 0.25 (less than 1) this implies that the adsorption of CQ onto PPAC-ZnO-NC is favourable. The maximum monolayer adsorption capacity (q_{max}) was found to be 77.51 mg/g. The Freundlich adsorption Isotherm (as shown in Figure 4.35B), best fitted the adsorption data with 0.99 as high R^2 value, therefore implying that heterogenous adsorption took place. The physical nature and favourability of the adsorption was expressed by the n values (greater than 1). As shown in Figure 4.35C, the Temkin Isotherm plot obtained an R^2 value of 0.95 suggesting the presence of adsorbate-adsorbent interaction in the sorption process. The D-R plot gave a

low R^2 value (0.86). However, the adsorption Energy of 0.71 kJ/mol (lower than 8 kJ/mol) shows that the sorption of CQ onto PPAC-ZnO-NC was physio-sorption.

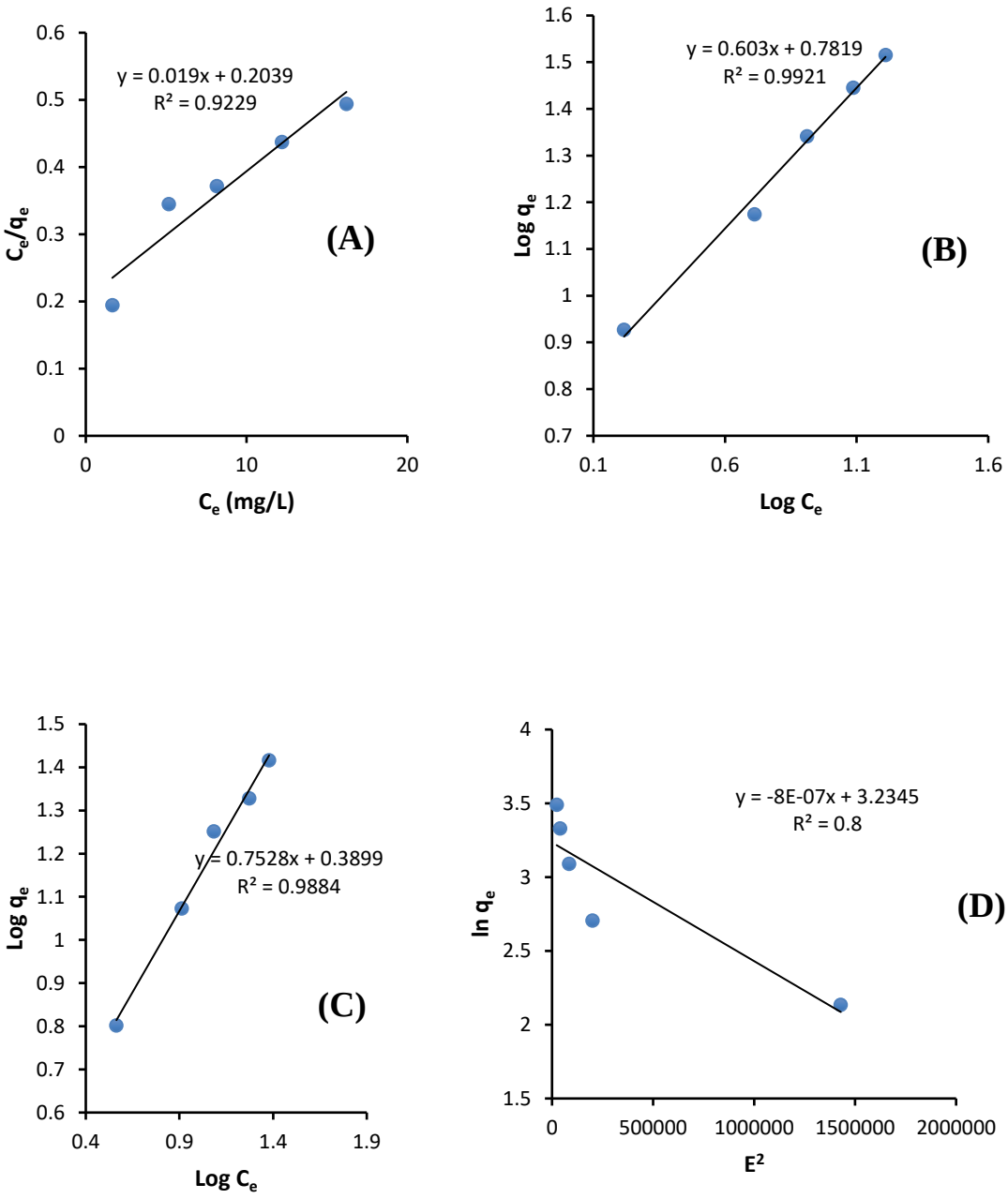

Figure 4.35: (A)Langmuir (B) Freundlich (C)Temkin and (D) D-R linear Isotherm plots for MG-RHAC System

Table 4.19: Adsorption Isotherm Parameters for uptake of MG using RHAC at Different Temperatures

	Parameters	303 K	313 K	323 K
Langmuir	q_m (mg/g)	33.67	52.632	58.139
	K_L (l/mg)	0.179	0.114	0.103
	R_L	0.101	0.149	0.162
	R^2	0.986	0.923	0.941
Freundlich	K_f(mg/g(L/mg))$^{1/n}$	6.055	6.052	2.454
	n	2.089	1.658	1.328
	R^2	0.959	0.992	0.988
Temkin	B_T	341.834	238.894	259.586
	K_t	1.276	1.112	2.197
	R^2	0.986	0.939	0.971
D-R	E_a (kJ/mol)	707.107	790.569	408.248
	q_m (mg/g)	22.940	25.343	21.471
	R^2	0.932	0.8	0.878
	$Bx10^{-6}$ ($Mol^2.KJ^{-2}$)	1.0	8.0	3.0

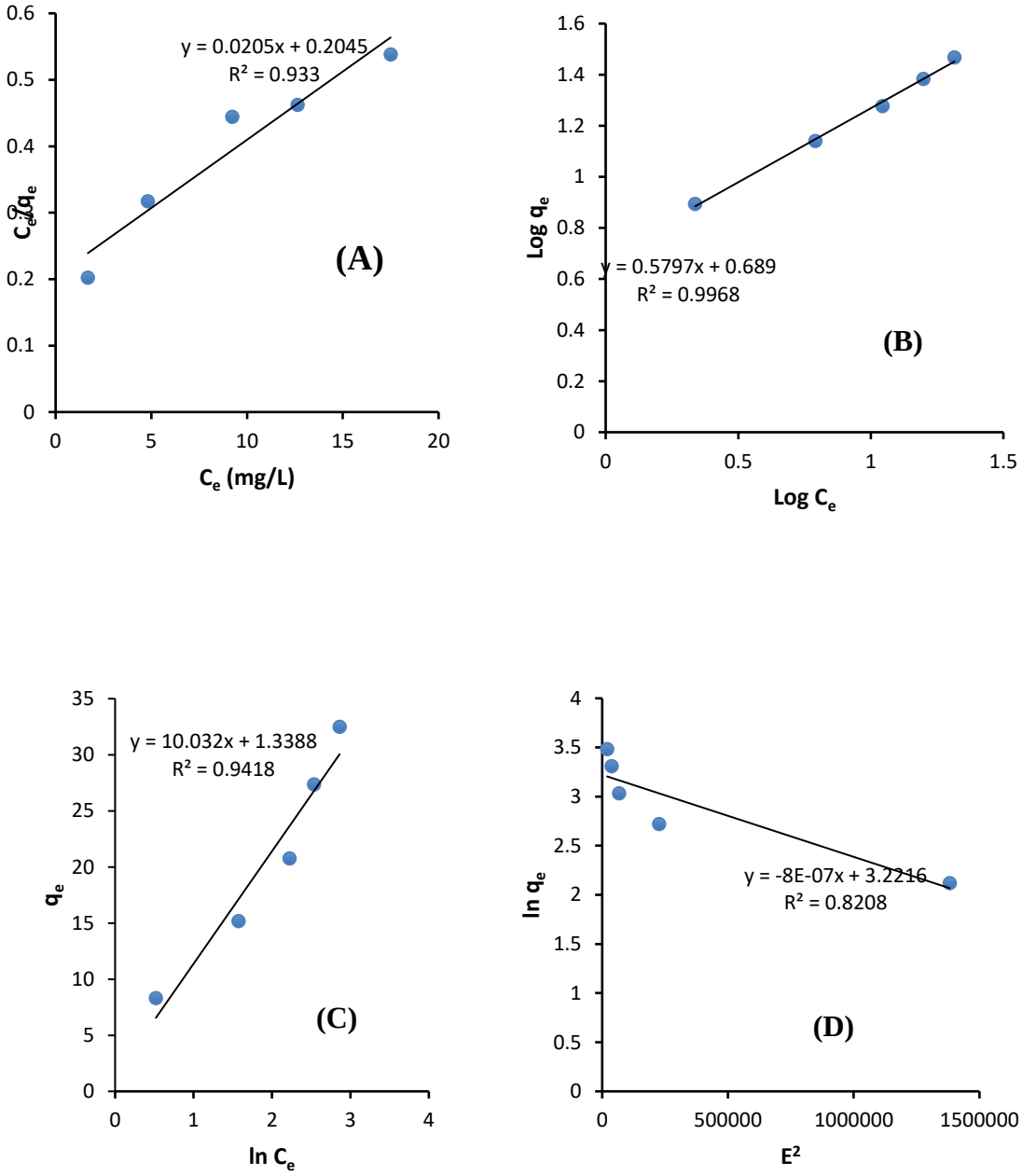

Figure 4.36: (A)Langmuir (B) Freundlich (C)Temkin and (D) D-R linear Isotherm plots for MG-RHAC-ZnO-NC System

Table 4.20: Adsorption Isotherm Parameters for uptake of MG using RHAC-ZnO-NC at Different Temperatures.

	Parameters	303 K	313 K	323 K
Langmuir	q_m (mg/g)	44.444	46.082	48.780
	K_L (l/mg)	0.0798	0.076	0.1
	R_L	0.2	0.206	0.166
	R^2	0.929	0.9115	0.933
Freundlich	K_f(mg/g(L/mg))$^{1/n}$	4.886	4.708	6.086
	n	1.725	1.655	1.724
	R^2	0.997	0.99	0.995
Temkin	B_T	293.536	270.763	251.110
	K_t	1.106	1.179	1.142
	R^2	0.939	0.9313	0.941
D-R	E_a (kJ/mol)	707.106	707.106	790.569
	q_m (mg/g)	22.522	23.027	25.068
	R^2	0.8109	0.8205	0.820
	β x10^{-6}($Mol^2.KJ^{-2}$)	1.0	1.0	80.0

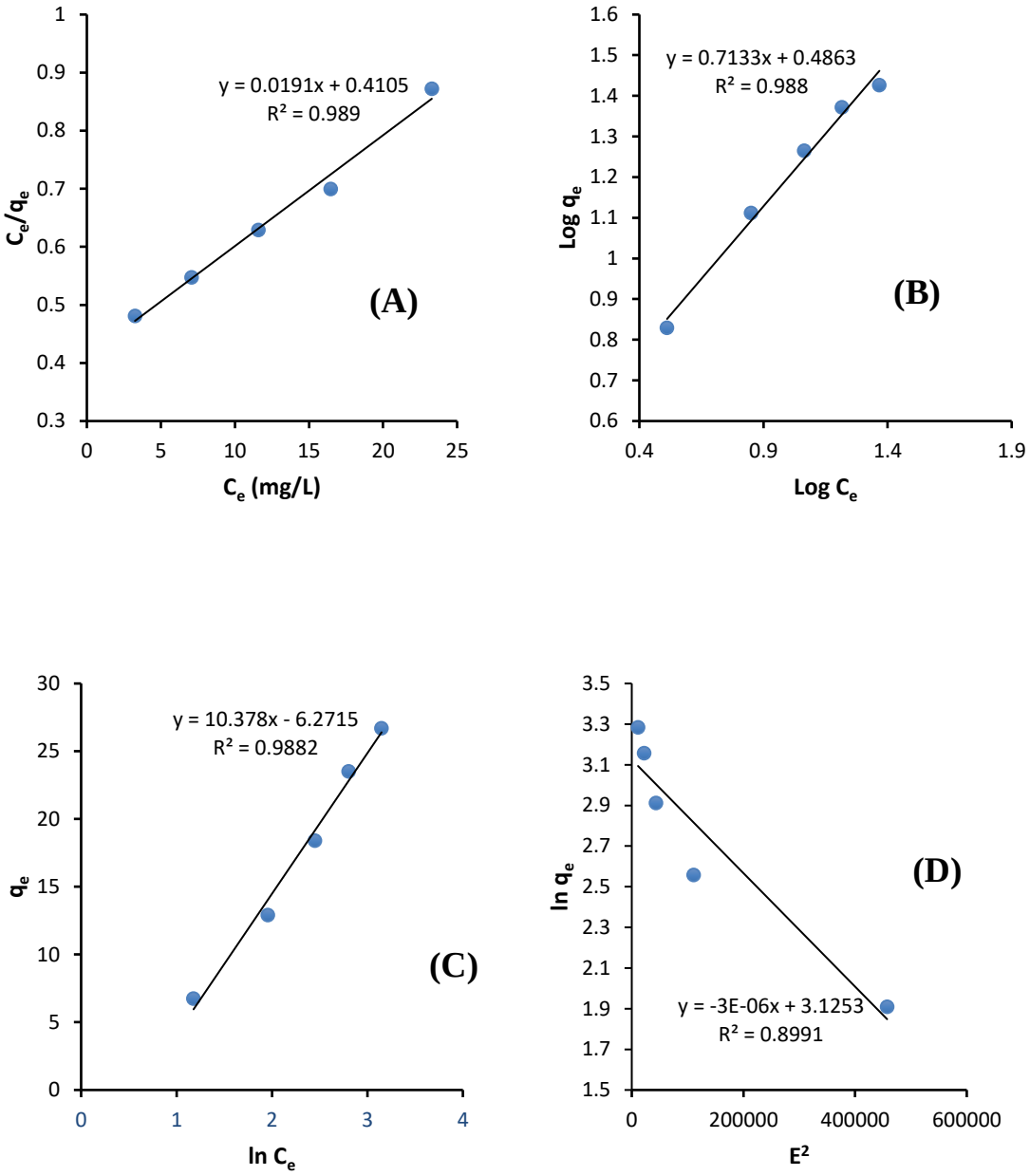

Figure 4.37: (A)Langmuir (B) Freundlich (C)Temkin and (D) D-R linear Isotherm plots for MG-PPAC System

Table 4.21: Adsorption Isotherm Parameters for uptake of MG using PPAC at Different Temperatures

	Parameters	303 K	313 K	323 K
Langmuir	q_m (mg/g)	35.587	50.251	52.356
	K_L (l/mg)	0.201	0.063	0.0465
	R_L	0.091	0.24	0.3006
	R^2	0.927	0.918	0.989
Freundlich	K_f(mg/g(L/mg))$^{1/n}$	9.427	4.167	3.0640
	n	2.73	1.547	1.4019
	R^2	0.961	0.991	0.988
Temkin	B_T	419.492	247.435	258.761
	K_t	4.052	1.380	1.829
	R^2	0.883	0.9434	0.988
D-R	E_a (kJ/mol)	1581.138	500	408.248
	q_m (mg/g)	22.607	23.509	22.766
	R^2	0.7165	0.861	0.899
	β x10^{-6}($Mol^2.KJ^{-2}$)	2.0	2.0	3.0

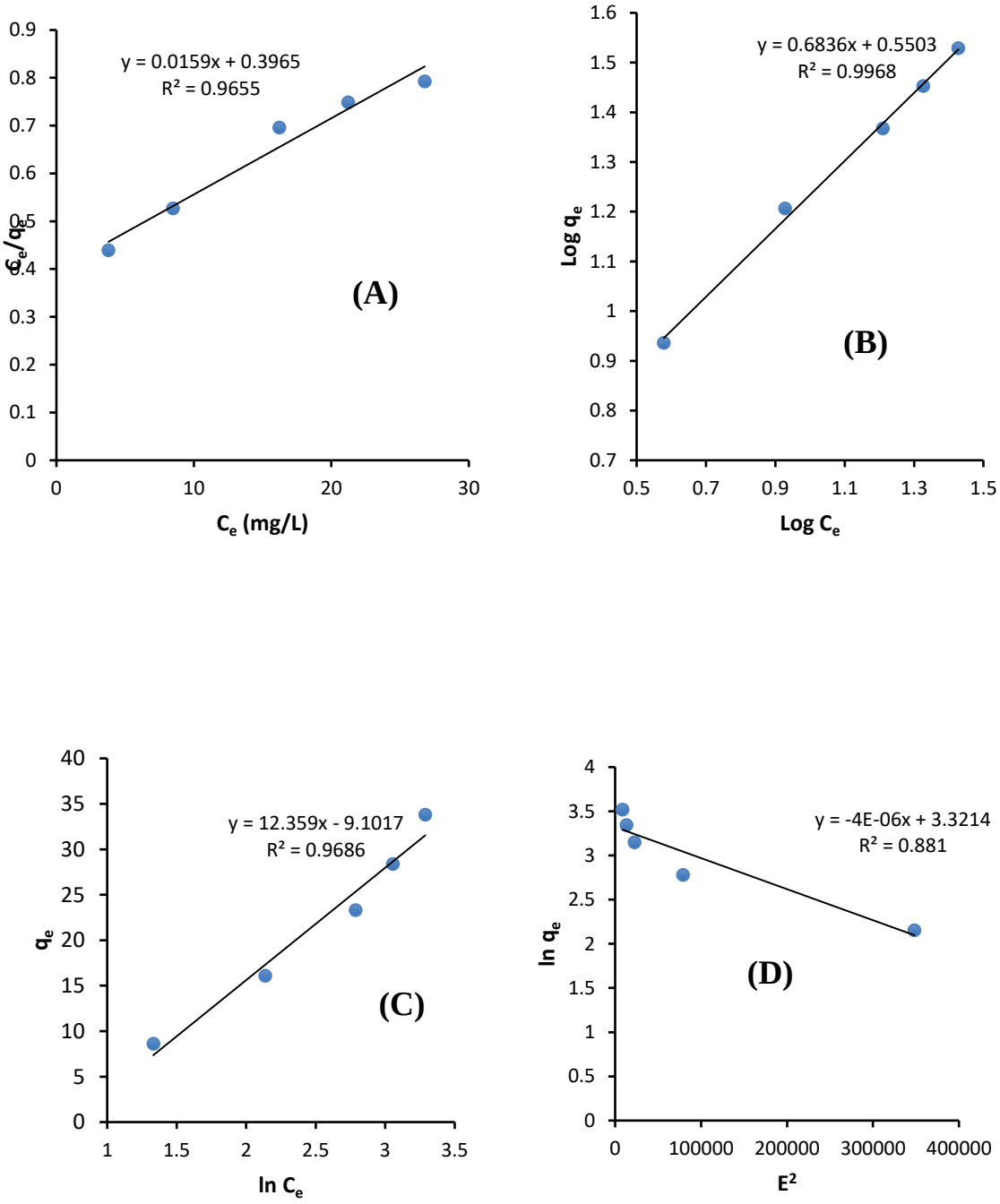

Figure 4.38: (A)Langmuir (B) Freundlich (C)Temkin and (D) D-R linear Isotherm plots for MG-PPAC-ZnO-NC System.

Table 4.22: Adsorption Isotherm Parameters for uptake of MG using PPAC-ZnO-NC at Different Temperatures

	Parameters	303 K	313 K	323 K
Langmuir	q_m (mg/g)	57.803	62.893	77.519
	K_L (l/mg)	0.053	0.04	0.057
	R_L	0.272	0.332	0.257
	R^2	0.986	0.965	0.958
Freundlich	K_f (mg/g(L/mg))$^{1/n}$	3.961	3.55	4.994
	n	1.456	1.462	1.339
	R^2	0.9991	0.996	0.9982
Temkin	B_T	228.11	217.284	193.333
	K_t	1.597	2.088	1.128
	R^2	0.975	0.968	0.9513
D-R	E_a (kJ/mol)	500	353.553	707.106
	q_m (mg/g)	24.818	27.699	27.560
	R^2	0.8654	0.881	0.8593
	β x10^{-6}($Mol^2.KJ^{-2}$)	2.0	4.0	1.0

Table 4.23: Maximum Monolayer Adsorption Capacity of Adsorbents in this study in comparison with other agrowastes and nanocomposites for MG Dye uptake.

DYE	Adsorbent	Qmax (mg/g)	Reference
Malachite green	Tamarind fruit shell	1.95	(Saha, Chowdhury, Gupta, Kumar, & Kumar, 2010)
Malachite green	Leaves of Solanum tuberosum	33.3	(Gupta, Kushwaha, & Chattopadhyaya, 2016)
Malachite green	Corn Cob (unfunctionalized)	35.34	(Gan, Leow, & Ong, 2017)
Malachite green	Wood Apple Shell	34.56	(Sartape *et al.*, 2017)
Malachite green	Pomegranate peel	31.5	(Gündüz & Bayrak, 2017)
Malachite Green	RHAC	58.14	This study
Malachite Green	RHAC-ZnO-NC	48.78	This study
Malachite Green	PPAC	52.35	This study
Malachite Green	PPAC-ZnO-NC	77.51	This study

4.3.3.4 Kinetic Studies.

Kinetic studies were carried out in order to investigate the rate of adsorption as well as the adsorbent-adsorbate interactions. Plots of the pseudo second order (PSO), pseudo first order (PFO) and Elovich were made as shown in Figure 4.39-4.42. Kinetic model parameters were calculated and outlined in Tables 4.24-4.27. The correlation coefficients R^2 values, chi square (X^2) and sum of square error (SSE) values were used to determine which of the Kinetic models best fit the adsorption process. Also, the closeness of the q_e calculated and q_e experimental values were further used to determine the model of best fit.

The PSO was the kinetic model of best fit for all adsorption systems. The pseudo first order plot of ln q_e-q_t versus time was made. As shown in Tables 4.24-4.27, low SSE values, lower X^2 values and the negligible difference between the q_e calculated and q_e experimented value for all adsorption systems for the removal of MG. The R^2 values across all concentrations for the PSO kinetic model was closer to unity than all other kinetic models. R^2 values ranged from 0.97-0.99 across all concentrations for all adsorption systems. The values of β decreases as concentration increases and the values of α which relates to chemisorption rate was noticed to increase as concentration increases. This indicates that more than one mechanism may govern the uptake. The lower R^2 values obtained for Elovich and PFO kinetic models along with the higher SSE values and higher X^2 values along with the larger difference between the q_e calculated and q_e experimental values makes the Elovich and PFO kinetics models not fit for explaining the adsorption data. The kinetic models of best fit therefore followed the order PSO > Elovich> PFO. Similar trend was reported by Sartape *et al.,* (2017) who sequestered MG using wood apple shell.

4.2.3.5.1 The Intraparticle Diffusion Model (IPD) Mechanism

The intraparticle diffusion model parameters and plots are shown in Figures 4.39-4.42 (D). The data of intraparticle diffusion models were deduced from the line equation of the plot of q_t versus $t^{1/2}$. For all initial adsorbate concentrations, the IPD plots did not pass through the origin as can be seen from the non-zero intercept (C) values outlined in Tables 4.24-4.27. The non-zero intercept obtained for nearly all adsorbent-adsorbate interactions suggests that the rate-limiting step is determined by the IPD but apparently may not be the

only mechanistic explanation for the MG uptake (Kumar & Kumaran, 2005; Li *et al.*, 2012). The increase in values of C as concentration increases shows that there was an increase in boundary layer effect as initial concentration increases.

The boundary layer diffusion is another likely mechanism for the diffusion of the pharmaceutical molecules into the adsorbent materials. The values obtained for boundary layer thickness (*C*) and K_{diff} were observed to increase generally as initial adsorbate concentration increased suggesting a consequent increase in the boundary layer effect. The capacity of adsorbent material to adsorb or retain MG in solution is greatly influenced by these parameters (Bello *et al.*, 2019).

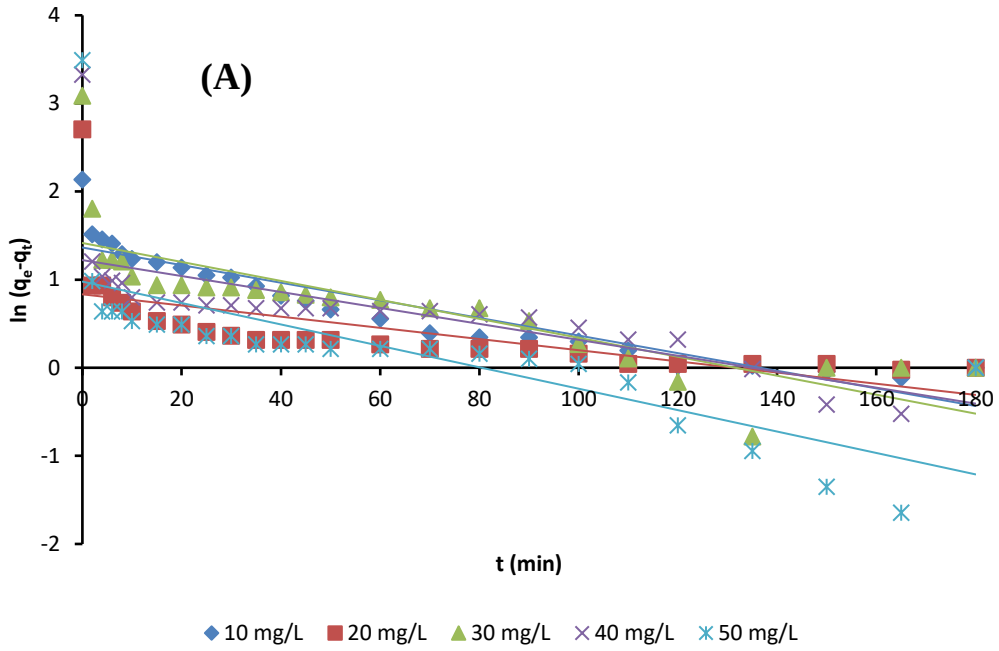
(A)
ln (qe-qt)
t (min)
10 mg/L
20 mg/L
30 mg/L
40 mg/L
50 mg/L

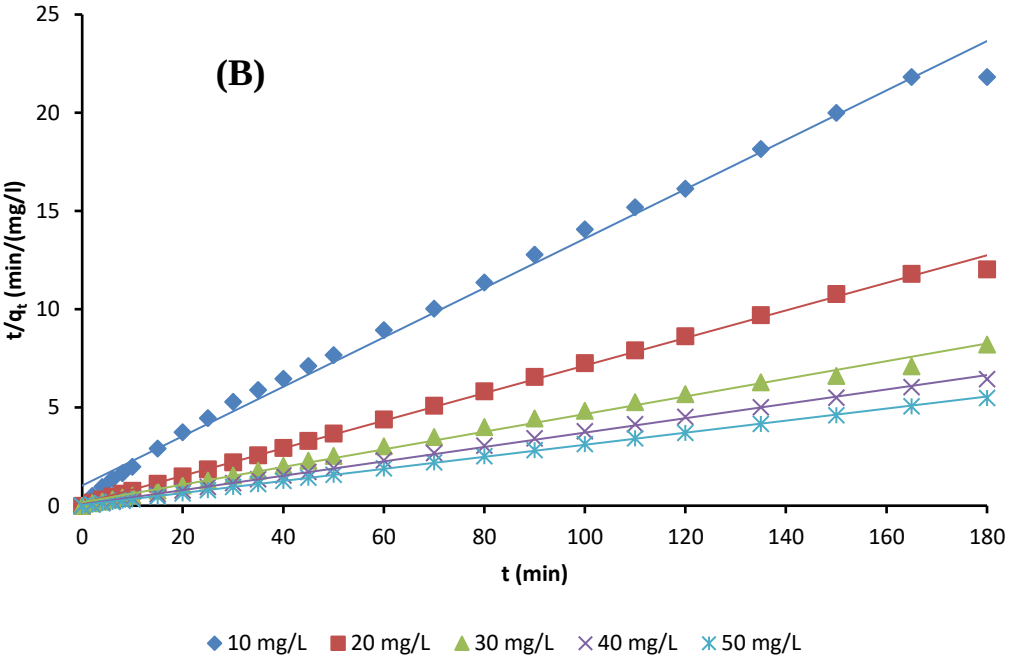
(B)
t/qt (min/(mg/l))
t (min)
10 mg/L
20 mg/L
30 mg/L
40 mg/L
50 mg/L

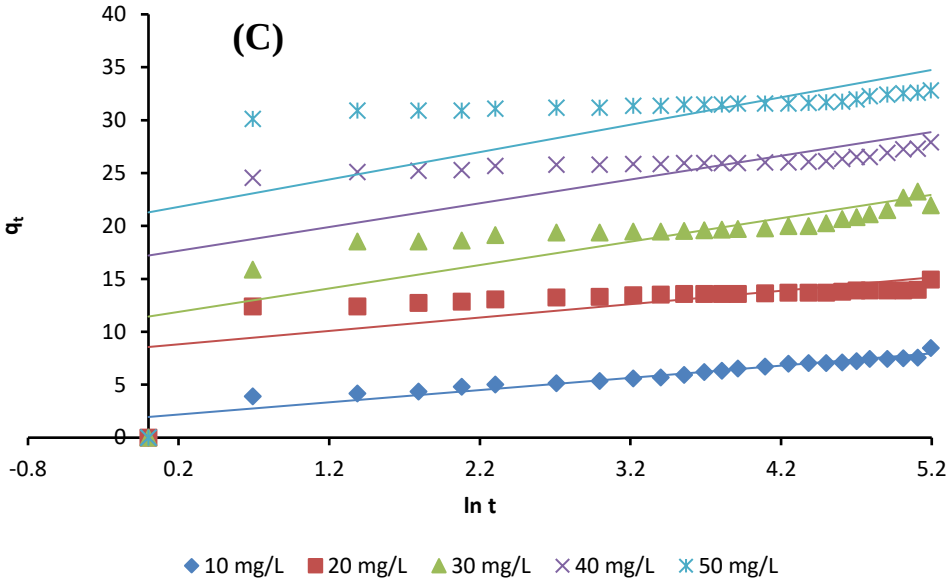

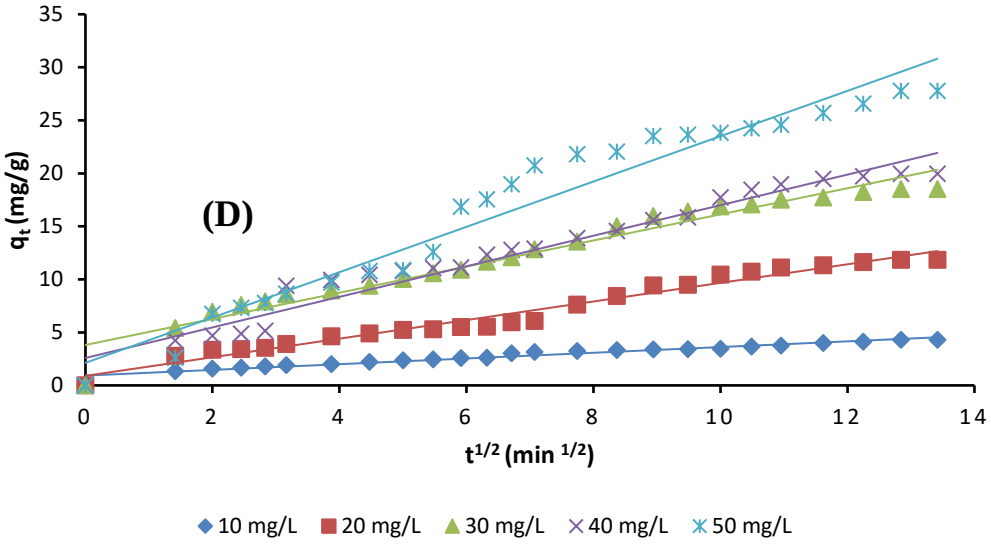

Figure 4.39: Plot of (a) PSO (b) PFO (c) Elovich and (d) IPD plot for RHAC-MG System.

Table 4.24: Parameters of Kinetic Model for MG Uptake using RHAC

Model	**Initial MG concentration (mg/L)**				
	10	20	30	40	50
PFO					
$q_{e(exp)}$(mg/L)	8.453	14.945	21.942	27.894	32.787
$q_{e(cal)}$(mg/L)	3.914	2.301	4.121	3.393	2.658
k_1(min^{-1})	0.01	0.006	0.011	0.009	0.012
R^2	0.860	0.407	0.652	0.528	0.532
SSE (%)	20.604	159.861	317.601	600.251	907.779
X^2	5.264	69.457	77.068	176.875	341.45
PSO					
$q_{e(exp)}$(mg/L)	8.453	14.945	21.942	27.893	32.787
$q_{e(cal)}$(mg/L)	7.955	14.245	22.271	27.322	32.573
k_2($gmg^{-1}min^{-1}$)	0.015	0.042	0.012	0.022	0.029
R^2	0.993	0.998	0.995	0.999	0.999
SSE (%)	0.247	0.490	0.108	0.326	0.046
X^2	0.031	0.034	0.004	0.012	0.001
Elovich					
β	1.253	0.444	0.304	0.255	0.175
α	0.890	3.307	4.257	5.114	9.652
R^2	0.087	0.879	0.948	0.951	0.949
Intraparticle-Diffusion					
C	0.924	0.901	3.812	2.587	2.128
k_{diff}	0.269	0.876	1.231	1.441	2.137
R^2	0.951	0.971	0.954	0.960	0.951

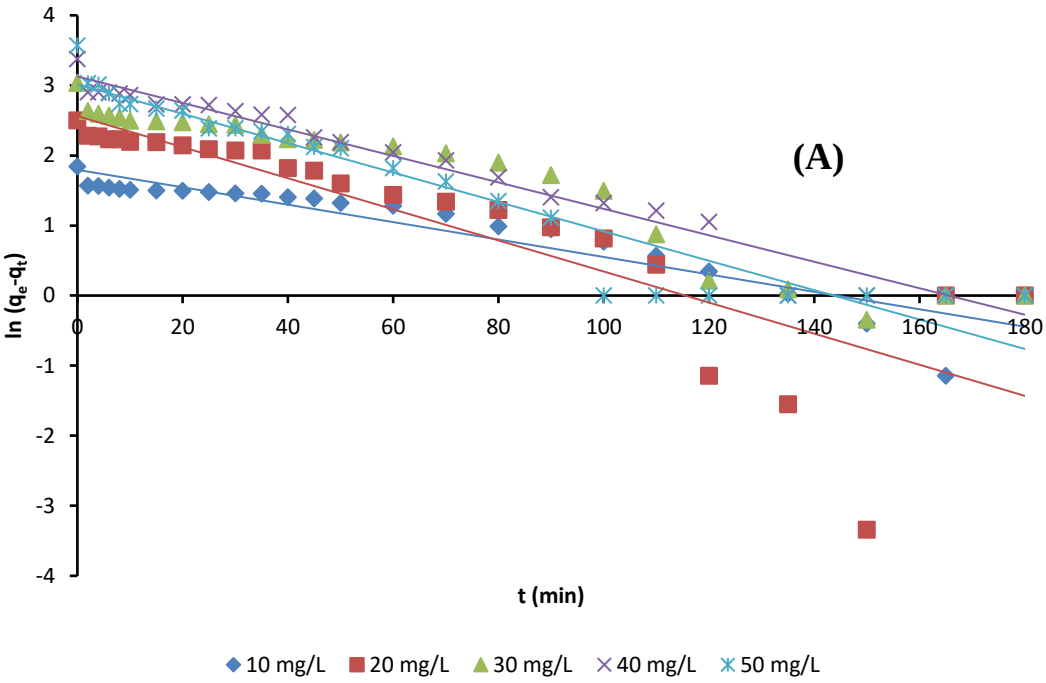
(A)
ln (qe-qt)
t (min)
10 mg/L
20 mg/L
30 mg/L
40 mg/L
50 mg/L

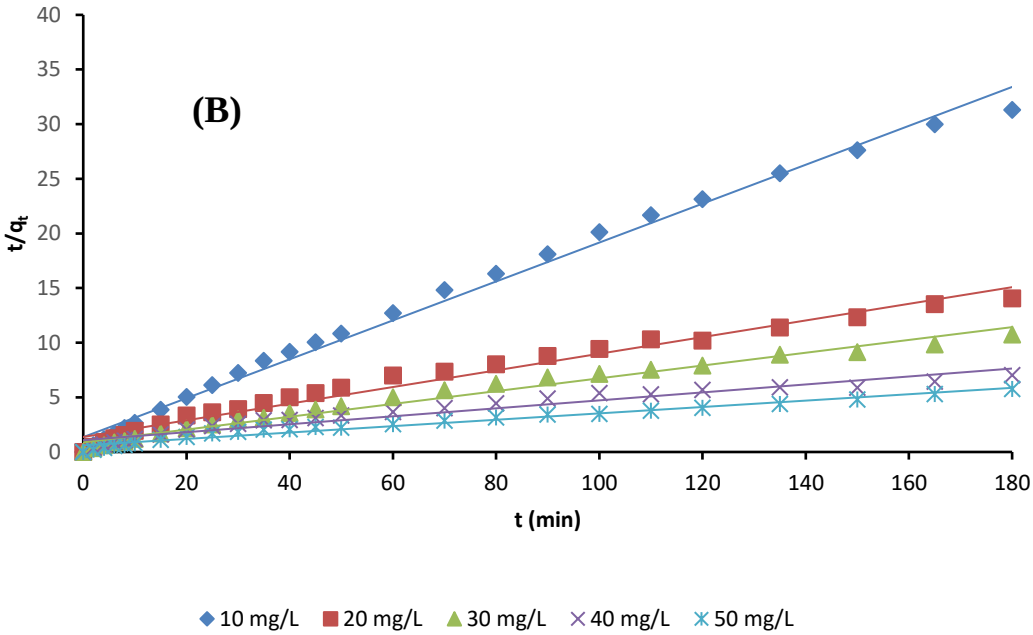
(B)
t/qt
t (min)
10 mg/L
20 mg/L
30 mg/L
40 mg/L
50 mg/L

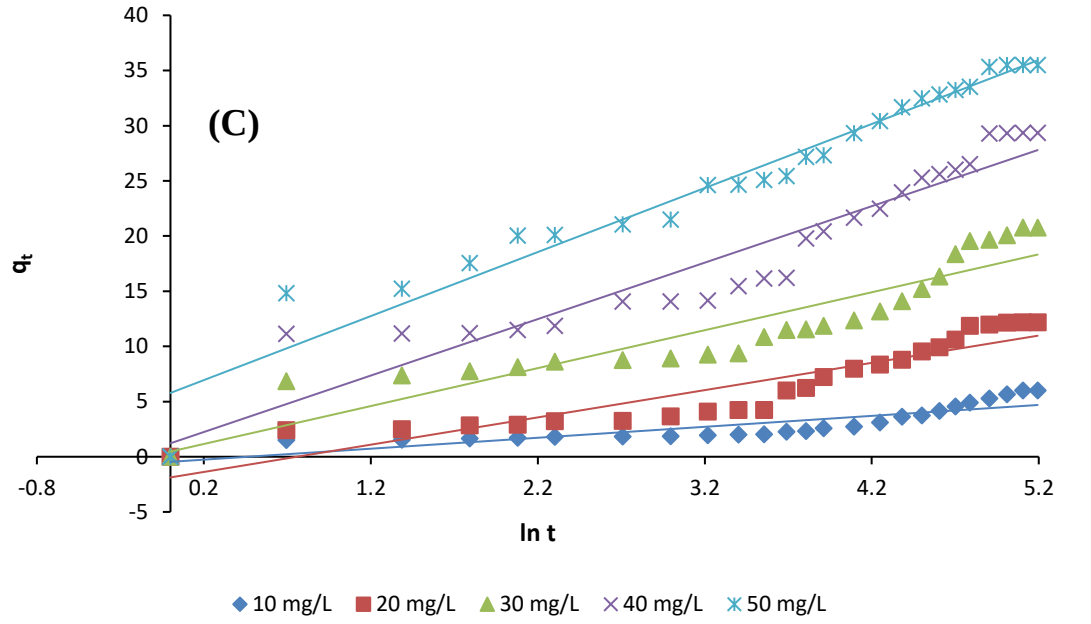

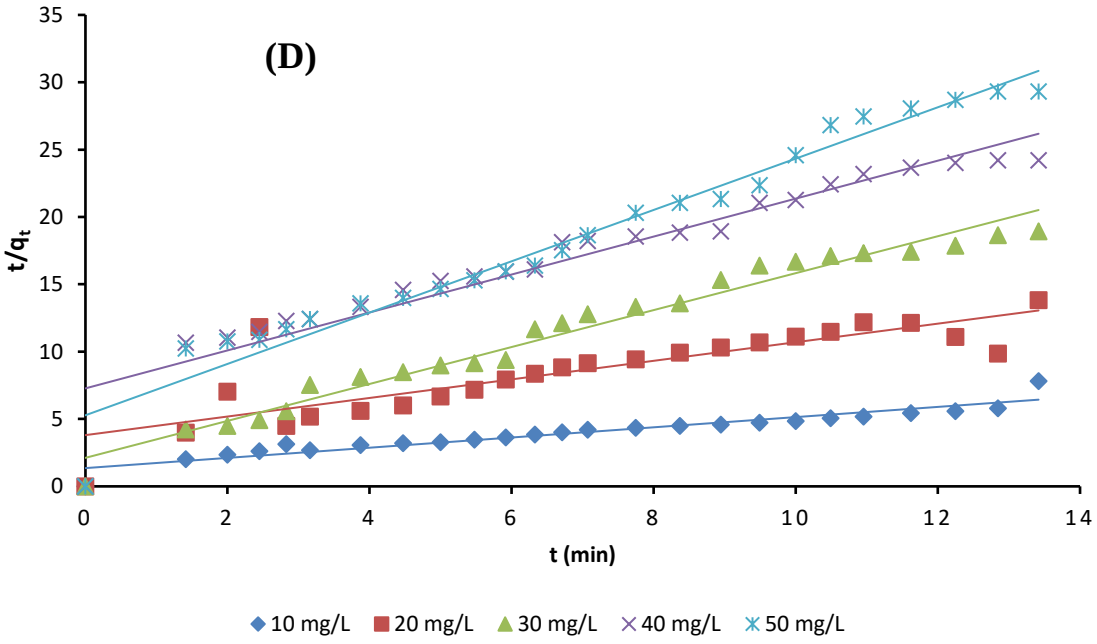

Figure 4.40: Plot of (a) PSO (b) PFO (c) Elovich and (d) IPD for RH-ZnO-NC-MG System.

Table 4.25: Parameters of Kinetic Model for MG Uptake using RH-ZnO-NC

Model	**Initial MG concentration (mg/L)**				
	10	20	30	40	50
PFO					
$q_{e(exp)}$(mg/L)	6.627	14.098	19.313	27.366	33.901
$q_{e(cal)}$(mg/L)	2.327	9.139	11.006	23.535	24.821
k_1(min^{-1})	0.011	0.015	0.0156	0.0168	0.020
R^2	0.777	0.951	0.893	0.9424	0.969
SSE (%)	28.084	24.587	151.464	14.674	82.459
X^2	12.063	2.69	13.761	0.623	3.322
PSO					
$q_{e(exp)}$(mg/L)	6.627	14.098	19.31373	27.36601	33.901
$q_{e(cal)}$(mg/L)	5.617	13.141	17.06485	27.47253	34.246
k_2($gmg^{-1}min^{-1}$)	0.023	0.0042	0.0039	0.0012	0.001
R^2	0.993	0.976	0.9786	0.9425	0.972
SSE (%)	1.019	0.916	5.057	0.011	0.118
X^2	0.181	0.069	0.296	0.00041	0.003
Elovich					
β	1.008	0.404	0.291	0.195454	0.172
α	1.578	5.274	3.939	6.489	15.71
R^2	0.754	0.853	0.8527	0.9054	0.953
Intraparticle-Diffusion					
C	0.169	0.029	3.1285	5.5604	11.648
k_{diff}	0.408	0.978	1.347	1.9495	2.0753
R^2	0.929	0.971	0.9512	0.9547	0.8851

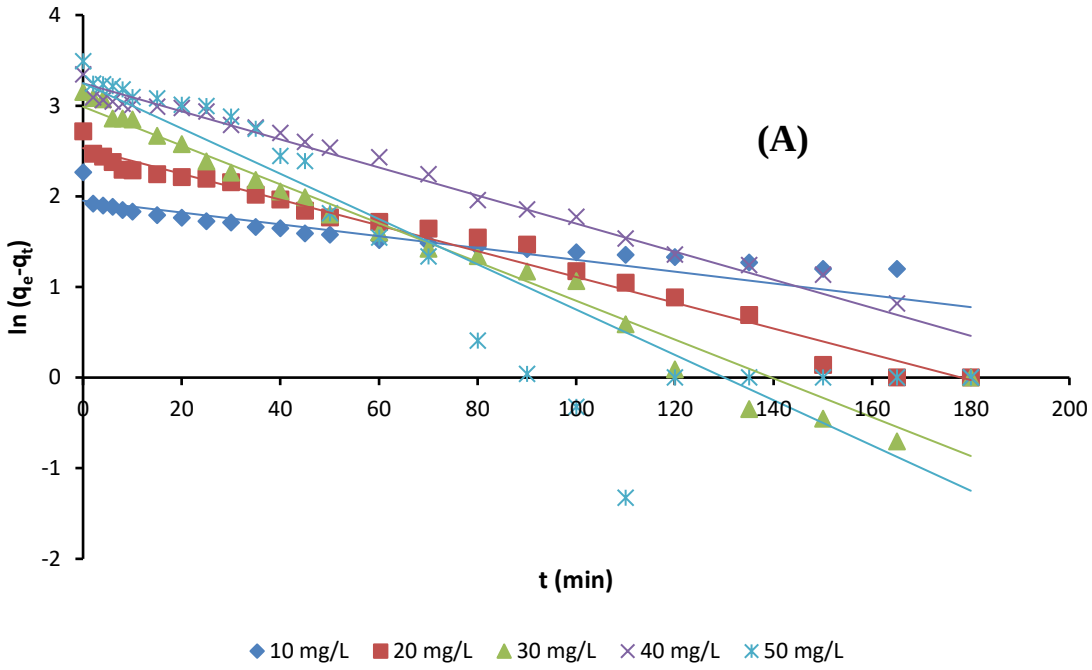
(A)
ln (qe-qt)
t (min)
10 mg/L
20 mg/L
30 mg/L
40 mg/L
50 mg/L

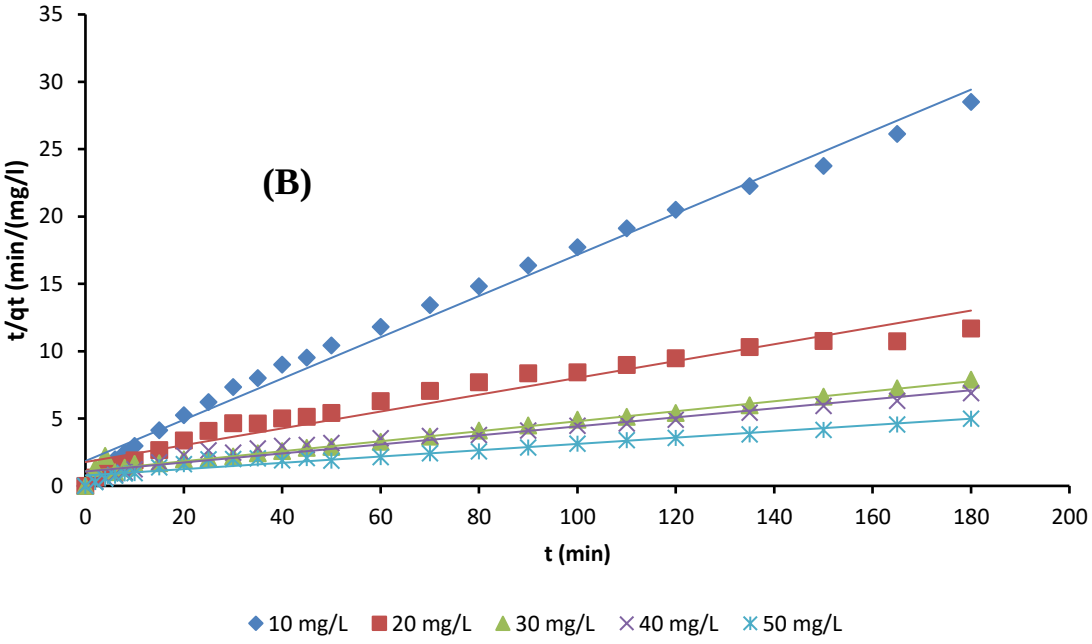
(B)
t/qt (min/(mg/l))
t (min)
10 mg/L
20 mg/L
30 mg/L
40 mg/L
50 mg/L

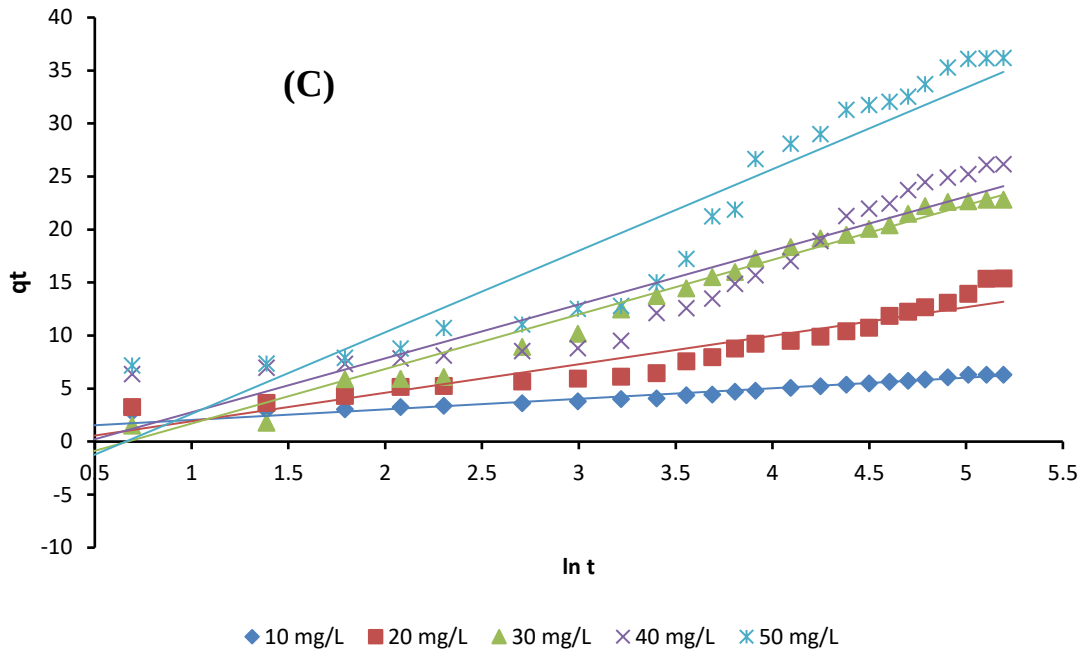

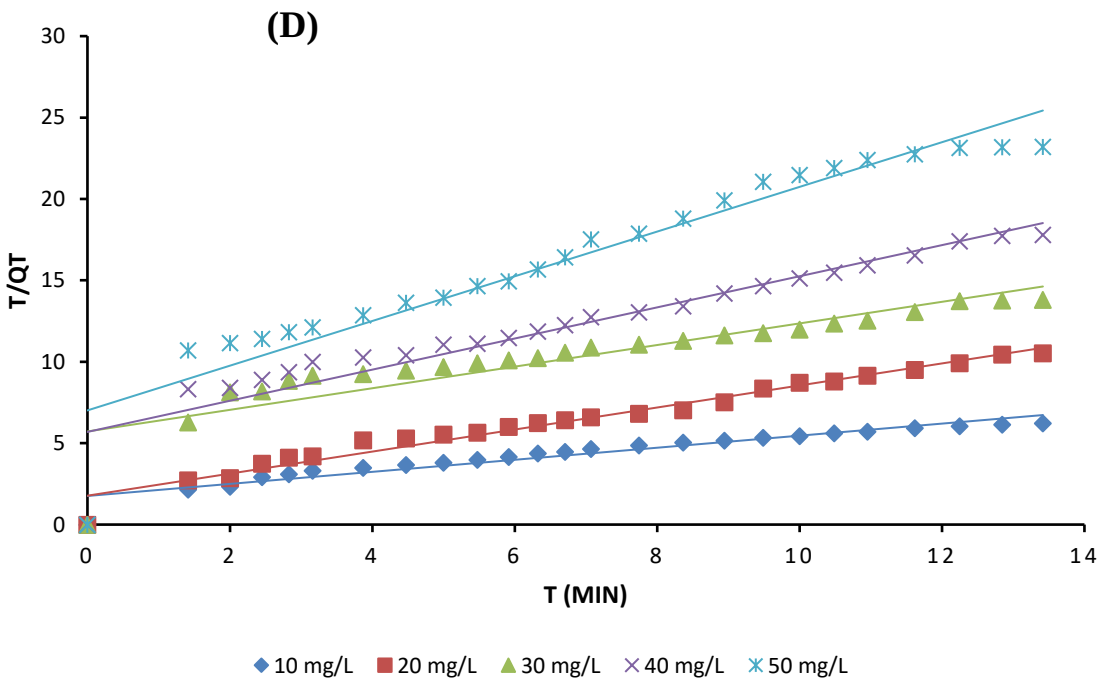

Figure 4.41: Plot of (a) PSO (b) PFO (c) Elovich and (d) IPD for PPAC-MG System

Table 4.26: Parameters of Kinetic Model for MG Uptake using PPAC

Model	**Initial MG concentration (mg/L)**				
	10	20	30	40	50
PFO					
$q_{e(exp)}$(mg/L)	6.212	10.522	13.809	17.802	23.208
$q_{e(cal)}$(mg/L)	3.811	8.567	7.816	12.208	18.152
k_1(min^{-1})	0.017	0.017	0.0201	0.019	0.0266
R^2	0.807	0.8	0.714	0.799	0.828
SSE (%)	5.766	3.823	35.906	31.293	25.564
X^2	1.513	0.446	4.593	2.563	1.408
PSO					
$q_{e(exp)}$(mg/L)	6.212	10.522	13.809	17.802	23.208
$q_{e(cal)}$(mg/L)	6.377	10.834	13.85	18.018	24.449
k_2($gmg^{-1}min^{-1}$)	0.012	0.0044	0.0079	0.0041	0.003
R^2	0.989	0.9652	0.989	0.981	0.986
SSE (%)	0.027	0.096	0.0017	0.0466	1.541
X^2	0.0042	0.0089	0.00012	0.0025	0.063
Elovich					
B	1.003	0.371	0.194	0.196	0.13
A	2.842982	3.584	10.049	8.021	14.868
R^2	0.939	0.913	0.974	0.889	0.905
Intraparticle-Diffusion					
C	1.994	1.467	1.944	1.871	1.922
k_{diff}	0.366	1.028	1.79	1.947	2.832
R^2	0.91	0.987	0.92	0.976	0.951

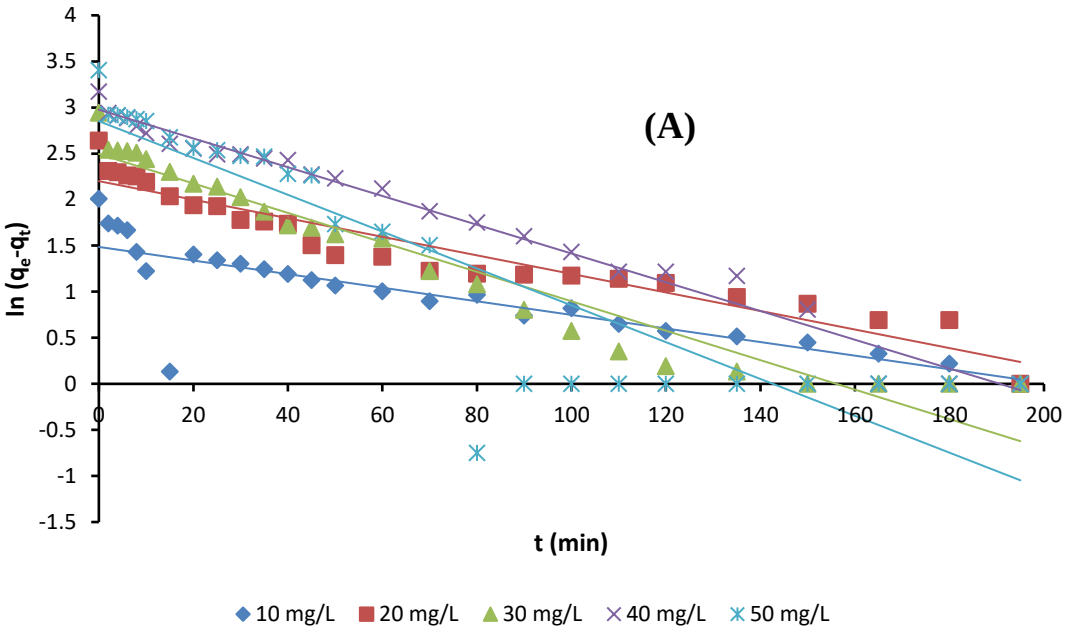
(A)
ln (qe-qt)
t (min)
10 mg/L
20 mg/L
30 mg/L
40 mg/L
50 mg/L

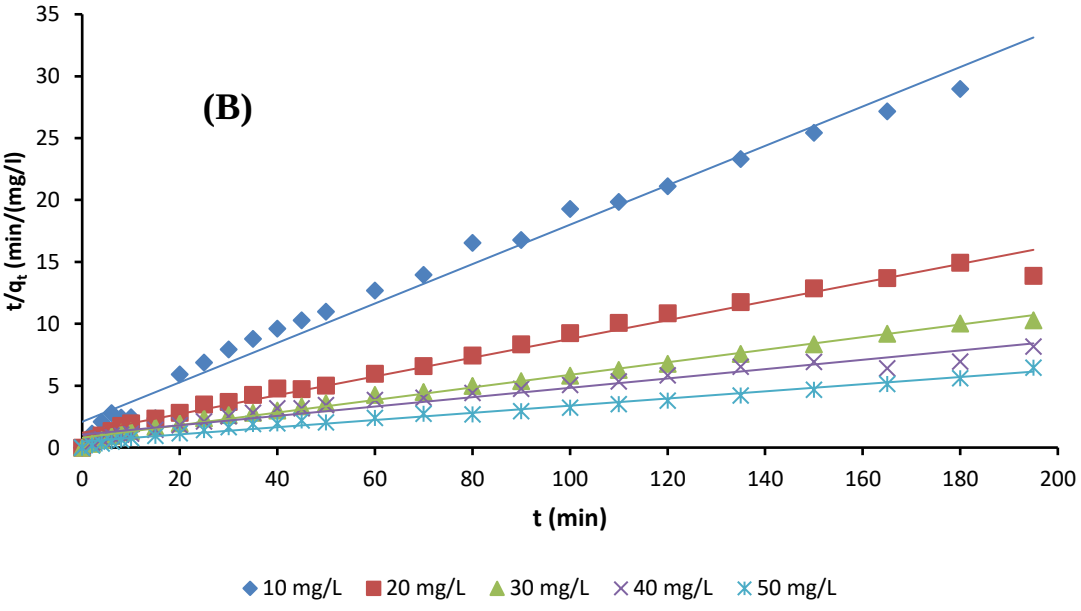
(B)
t/qt (min/(mg/l))
t (min)
10 mg/L
20 mg/L
30 mg/L
40 mg/L
50 mg/L

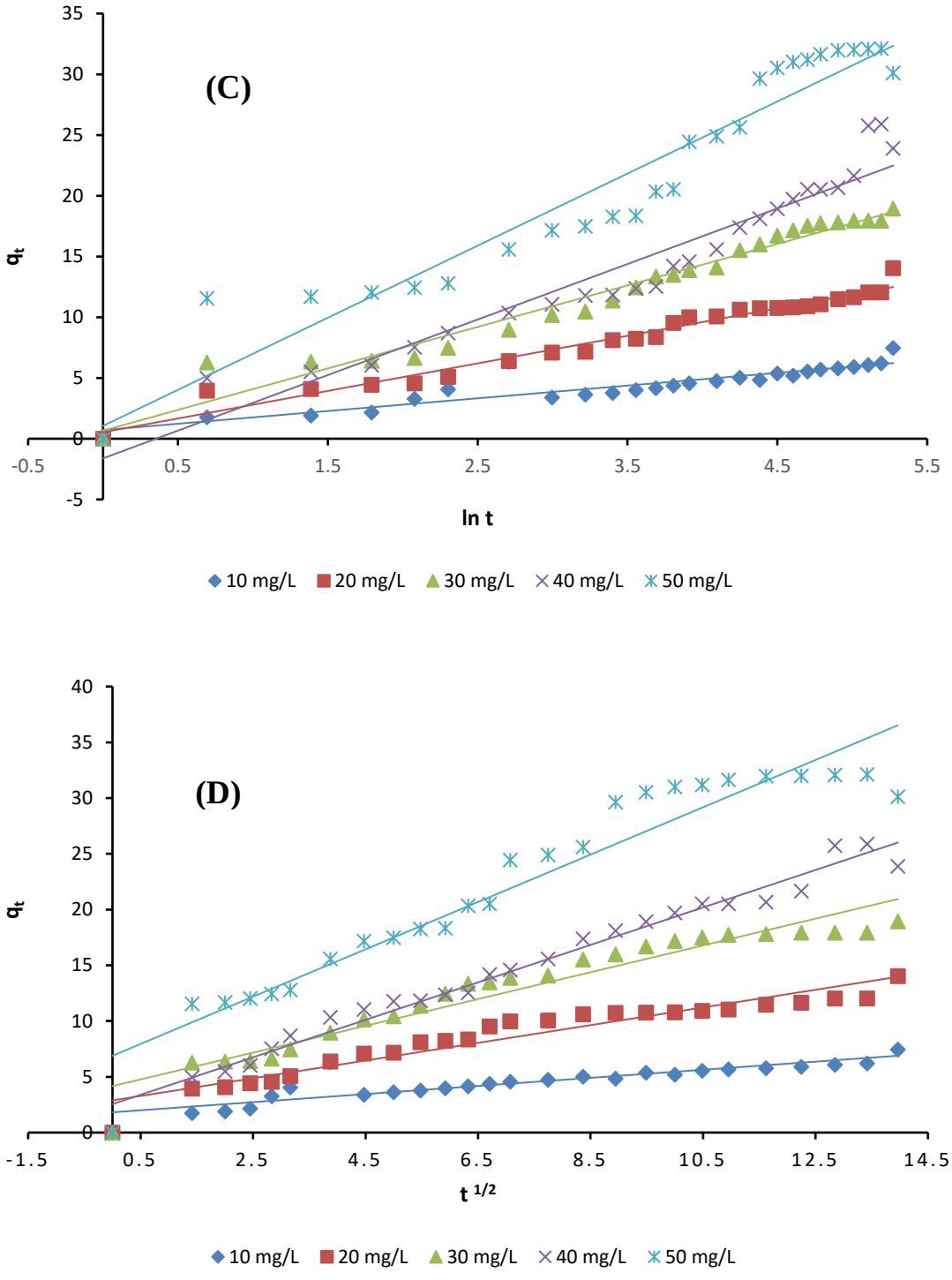

Figure 4.42: Plot of (a) PSO (b) PFO (c) Elovich and (d) IPD for PPAC-ZnO-MG system

Table 27: Parameters of Kinetic Model for MG Uptake using PPAC-ZnO-NC

Model	**Initial MG concentration (mg/L)**				
	10	20	30	40	50
PFO					
$q_{e(exp)}$(mg/L)	7.459	14.042	18.943	23.894	30.113
$q_{e(cal)}$(mg/L)	4.419	9.026	12.121	19.601	17.312
k_1(min^{-1})	0.007	0.01	0.016	0.015	0.02
R^2	0.701	0.915	0.942	0.981	0.797
SSE (%)	9.238	25.156	46.552	18.426	163.867
X^2	2.09	2.786	3.841	0.94	9.465
PSO					
$q_{e(exp)}$(mg/L)	7.459	14.0424	18.943	23.893	30.113
$q_{e(cal)}$(mg/L)	6.281	13.1926	19.685	26.455	34.482
k_2($gmg^{-1}min^{-1}$)	0.012	0.00479	0.0032	0.0013	0.0017
R^2	0.983	0.9833	0.991	0.956	0.981
SSE (%)	1.387	0.722	0.549	6.558	19.094
X^2	0.221	0.0547	0.0279	0.247	0.553
Elovich					
β	0.955	0.441	0.292	0.218	0.168
α	2.063	2.866	4.148	6.514	7.08
R^2	0.817	0.966	0.966	0.934	0.925
Intraparticle-Diffusion					
C	1.816	2.885	4.165	2.547	6.885
k_{diff}	0.363	0.793	1.201	1.680	2.122
R^2	0.763	0.916	0.925	0.978	0.918

4.3.3.5 Thermodynamic Studies

Thermodynamic studies were carried out to further understand the feasibility, nature and spontaneity of the adsorption. The enthalpy, entropy and Gibbs free energy were calculated. Thermodynamic parameters were evaluated using the ΔG, ΔH and ΔS values as shown in Figure 4.43 and Table 4.28-4.31. the Enthalpy values (ΔH) values give an idea of the nature of the adsorption, the entropy values (ΔS) give an idea on the feasibility while the Gibbs free energy values (ΔG) give an idea on the spontaneity of the adsorption. The amount of CQ removed by RHAC, RHAC-ZnO-NC, PPAC and PPAC-ZnO-NC between temperatures 303 K – 323K were obtained from the linear plot of $ln\ K_L$ against the reciprocal of temperature T (K). Figure 4.43 shows the Van't Hoff plot where the thermodynamic parameters were calculated from.

For all adsorption systems, negative ΔG values were obtained showing that all adsorption processes were spontaneous. The observed increase in the value of ΔG with increase in temperature implies that temperature rise has a significant impact on the thermodynamics. Positive values were obtained for ΔS which indicates that there was an increase in randomness at the adsorbent-adsorbate interface. The positive ΔH values however expressed the endothermic nature of the process. Similar trend in thermodynamic parameters was observed by Quesada *et al.,* (2019) who examined the use of modified Moringa Olifera Seed Husk for adsorptive uptake of acetaminophen.

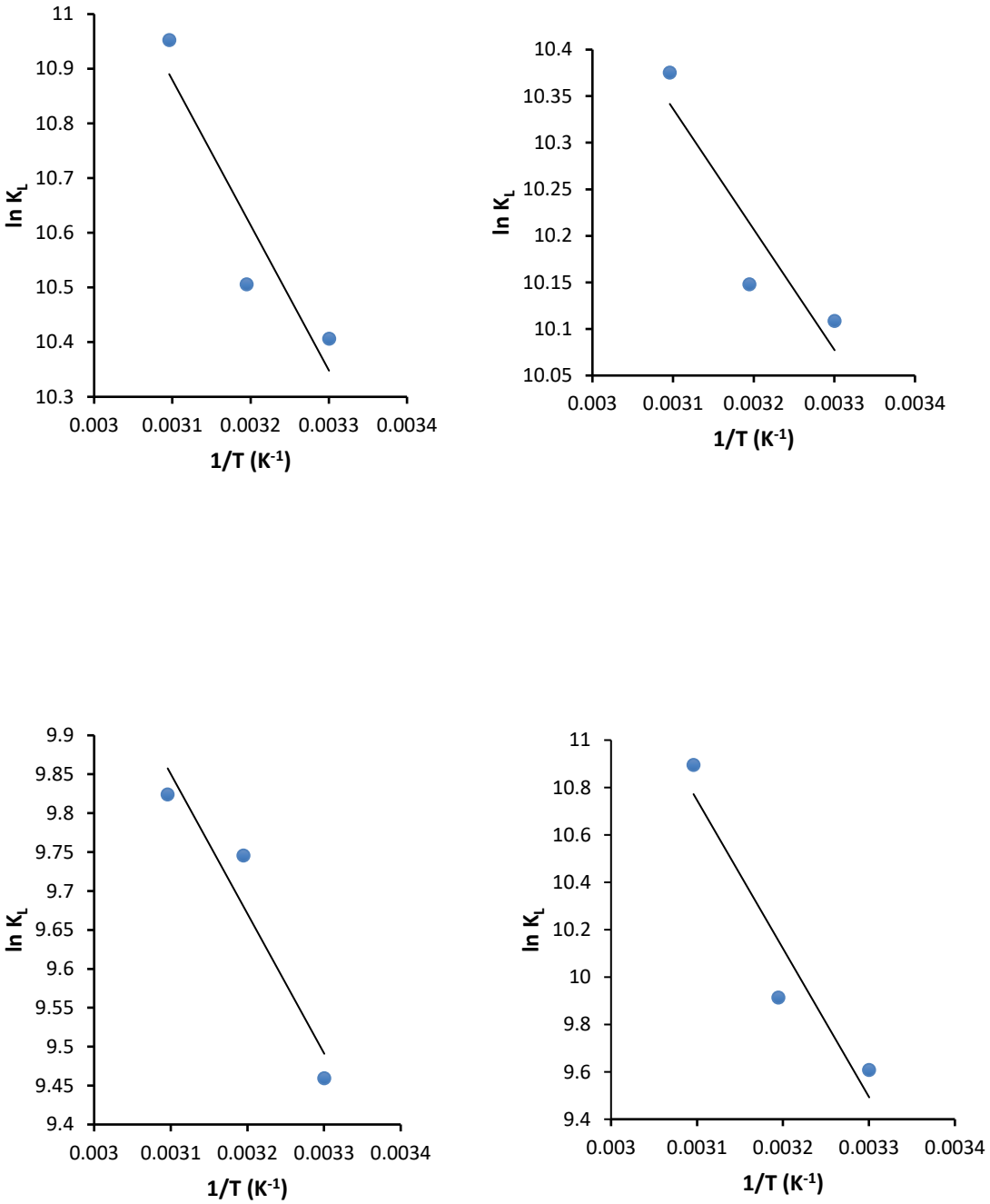

Figure 4.43: Van't Hoff Plot for the adsorption of MG onto (A) RHAC (B) RHAC/ZnO-NC (C) PPAC (D) PPAC-ZnO-NC

Table 4.28: Outlined Thermodynamics Data for the Adsorption of MG onto RHAC

Temp(*K*)	***ΔG*(kJ/mol)**	***ΔH*(kJ/mol)**	***ΔS*(J/mol)/K)**	E_a **(kJ/mol)**
303	-26.215	22.065	158.855	24.584
313	-27.340			24.667
323	-29.413			24.750

Table 4.29: Outlined Thermodynamics Data for the Adsorption of MG onto RHAC-ZnO-NC

Temp(*K*)	***ΔG*(kJ/mol)**	***ΔH*(kJ/mol)**	***ΔS*(J/mol)/K)**	E_a **(kJ/mol)**
303	-25.465	10.760	119.297	13.279
313	-26.408			13.363
323	-27.862			13.446

Table 4.30: Outlined Thermodynamics Data for the Adsorption of MG onto PPAC

Temp(*K*)	***ΔG*(kJ/mol)**	***ΔH*(kJ/mol)**	***ΔS*(J/mol)/K)**	E_a **(kJ/mol)**
303	-23.829	14.919	128.143	17.438
313	-25.360			17.521
323	-26.381			17.604

Table 4.31: Outlined Thermodynamics Data for the Adsorption of MG onto PPAC-ZnO-NC

Temp(*K*)	***ΔG*(kJ/mol)**	***ΔH*(kJ/mol)**	***ΔS*(J/mol)/K)**	E_a **(kJ/mol)**
303	-24.203	52.062	250.741	54.581
313	-25.798			54.664
323	-29.258			54.747

CHAPTER FIVE

5.0 SUMMARY, CONCLUSION AND RECOMMENDATION

5.1 Summary

From this study, the preparation and characterization of rice husk and plantain peel activated carbon and their zinc oxide nanocomposites was successfully done. Physicochemical characterization revealed that the adsorbents possessed excellent characteristics that makes them suitable for application as low-cost and efficient adsorbents. Characterization was done by series of physicochemical and spectroscopic techniques such as moisture content, ash content, volatile matter, determination of oxygen containing functional groups using Boehm titration, surface area determination using sears method, iodine number determination and Surface area using iodine number, X-ray Diffraction (XRD), Scanning Electron Microscopy (SEM) and Fourier Transform Infrared (FTIR). The adsorbents (base materials and nanocomposites) were utilized for effective sequestration of chloroquine and malachite green dye (endocrine disruptive compounds) by batch adsorption technique. The removal efficiency and quantity adsorbed were influenced by various operational parameters vis-à-vis effect of pH, initial concentrations, contact time and temperature.

Data obtained from equilibrium, kinetic and thermodynamic studies were fitted to relevant models. Equilibrium data were fitted to four isotherm models (Langmuir, Freundlich, Temkin and Dubunin Radushkelvich Isotherm models). Kinetic data were analysed using four kinetics and mechanism models (Pseudo First Order, Pseudo Second Order, Elovich and Intraparticle Diffusion). Thermodynamic parameters were evaluated from the thermodynamic studies suggesting a feasible, spontaneous and endothermic adsorption. The adsorbents therefore showed excellent performance for the sorption of CQ and MG from aqueous media.

5.2 Conclusion

The various physicochemical and spectroscopic characterization processes carried out on the adsorbents revealed that the acid modification and loading of nanoparticles improved the pore structure and surface characteristics of the agro wastes, thereby making them effective adsorbents. SEM results showed the presence of pores on the adsorbent surface. FTIR gave information on the functional groups on the adsorbents while investigations on the material structure was determined by X-ray Diffraction (XRD).

During the batch adsorption studies, fast and rapid adsorption occurred within the first 40 minutes for all adsorption systems monitored in this study and gradually became slower until equilibrium was attained between 180-300 minutes. It was also observed that temperature, pH, contact time and initial adsorbate concentration all affected the rate of adsorption of MG and CQ.

Generally, the equilibrium data best fitted the Freundlich model and the PSO Kinetics model as observed from the similarity between experimental and calculated Q_e values, low SSE and a high regression coefficient (R^2). Thermodynamics study revealed that all adsorption processes were spontaneous, favourable and endothermic with increased randomness at the adsorbent- adsorbate interface. The E values from the thermodynamics parameters and D-R plot also showed that physisorption was the dominant mode of adsorption.

In conclusion, it can be inferred that RHAC, PPAC, RHAC-ZnO-NC and PPAC-ZnO-NC are effective for uptake of CQ and MG dye.

5.3 Recommendations

Based on the limitations and findings from this research, I strongly recommend the following

i. The uptake of CQ and MG should be studied using real life industrial effluent.
ii. Desorption and reusability studies on these adsorbents can be carried out.

iii. EDX, TEM and other spectroscopic characterization can be carried out to give more light on the nature and characteristics of these adsorbents.

5.4 Contributions to knowledge

i. This study has been successful in removing CQ and MG from water using Rice Husk, Plantain peel and their ZnO nanocomposites.

ii. PPAC-ZnO-NC and RHAC-ZnO-NC which have not been previously explored by various researchers were prepared and characterized in this study

iii. The physicochemical and spectroscopic characterization showed unique properties of the base material and ZnO loaded nanocomposites. Their effectiveness in adsorption which has not been reported was explored in this study.

iv. Several studies have been reported on pharmaceutical adsorption but the adsorption of CQ has not been reported. The prepared adsorbents have been shown to exhibit excellent performance for the uptake of CQ.

REFERENCES

Abdullah, A. N., Abdullah, S. P., Amin, M. F. M., & Zainol, A. N. (2018). Preparation and characterization of a new biocarbon material derived from *Macaranga gigantea* (giant 'Mahang') leaf biomass as precursor. *Materials Today: Proceedings*, *5*(10), 21888–21896. https://doi.org/10.1016/j.matpr.2018.07.047

Adegoke, K. A., & Bello, O. S. (2015). Dye sequestration using agricultural wastes as adsorbents. *Water Resources and Industry*, *12*, 8–24. https://doi.org/10.1016/j.wri.2015.09.002

Adekola, F. A., Ayodele, S. B., & Inyinbor, A. A. (2019). Activated biochar prepared from plaintain peels : Characterization and Rhodamine B adsorption data set. *Chemical Data Collections*, *19*, 100170. https://doi.org/10.1016/j.cdc.2018.11.012

Adeolu, A. ., Okareh, O. ., & Dada, A. . (2016). Adsorption of Chromium Ion from Industrial Effluent Using Activated Carbon Derived from Plantain *(Musa paradisiaca)* Wastes. *American Journal of Environmental Protection*, *4*(No 1), 7–20. https://doi.org/10.12691/env-4-1-2

Adewale, O. B., Davids, H., Cairncross, L., & Roux, S. (2019). Toxicological Behavior of Gold Nanoparticles on Various Models: Influence of Physicochemical Properties and Other Factors. *International Journal of Toxicology*, *38*(5), 357–384. https://doi.org/10.1177/1091581819863130

Afolabi, I. C., Popoola, S. I., & Bello, S. O. (2020). Machine learning approach for prediction of paracetamol adsorption efficiency on chemically modified orange peel. *Spectrochimica Acta Part A: Molecular and Biomolecular Spectroscopy*, 6(24) 118769. https://doi.org/10.1016/j.saa.2020.118769

Agboola, O. S., Akanji, S. B., & Bello, O. S. (2021). Functionalized Banana Stalk for Lumefantrine Drug Removal. *Physical Chemistry Research*, *9*(3), 483–507. https://doi.org/10.22036/pcr.2021.261506.1865

Agboola, O. S, & Bello, O. S. (2020). Enhanced adsorption of ciprofloxacin from

aqueous solutions using functionalized banana stalk. *Biomass Conversion and Biorefinery*. 6(12) https://doi.org/10.1007/s13399-020-01038-9

Ahmad, M. A., Adilah, N., Ahmed, B., Adegoke, K. A., & Bello, O. S. (2020). Adsorptive potentials of Lemongrass leaf for Methylene Blue dye removal. *Chemical Data Collections*, 8(6)100578. https://doi.org/10.1016/j.cdc.2020.100578

Ahmed, M. B., Zhou, J. L., Ngo, H. H., Johir, A. H., & Sornalingam, K. (2017). Sorptive removal of phenolic endocrine disruptors by functionalized biochar: Competitive interaction mechanism , removal efficacy and application in wastewater. *Chemical Engineering Journal*. 6(23), 567-570. https://doi.org/10.1016/j.cej.2017.11.041

Akter, M., Sikder, M. T., Rahman, M. M., Ullah, A. K. M. A., Hossain, K. F. B., Banik, S., … Kurasaki, M. (2018). A systematic review on silver nanoparticles-induced cytotoxicity: Physicochemical properties and perspectives. *Journal of Advanced Research*, *9*, 1–16. https://doi.org/10.1016/j.jare.2017.10.008

Ali, I., Alharbi, O. M. L., Alothman, Z. A., & Alwarthan, A. (2018). Facile and eco-friendly synthesis of functionalized iron nanoparticles for cyanazine removal in water. *Colloids and Surfaces B: Biointerfaces*, *171*(4), 606–613. https://doi.org/10.1016/j.colsurfb.2018.07.071

Alipanahpour Dil, E., Ghaedi, M., Asfaram, A., Mehrabi, F., & Fardin Sadeghfar. (2019). Efficient adsorption of Azure B onto CNTs/Zn:ZnO@Ni2P-NCs from aqueous solution in the presence of ultrasound wave based on multivariate optimization. *Journal of Industrial and Engineering Chemistry*, *74*, 55–62. https://doi.org/10.1016/j.jiec.2018.12.050

Anna, T., Jens, K., Olov, E., Thomas, A., & Schroder, E. (2018). Removal of phenol and chlorine from wastewater using steam activated biomass soot and tire carbon black. *Journal of Harzadous Materials*.12(6) 2234-2456 https://doi.org/10.1016/j.jhazmat.2018.09.061

Anyanwu, I. N., Alo, M. N., Onyekwere, A. M., Crosse, J. D., Nworie, O., & Chamba, E. B. (2018). Influence of biochar aged in acidic soil on ecosystem engineers and two

tropical agricultural plants. *Ecotoxicology and Environmental Safety*, *153*(1), 116–126. https://doi.org/10.1016/j.ecoenv.2018.02.005

Arampatzidou, A. C., & Deliyanni, E. A. (2016). Comparison of activation media and pyrolysis temperature for activated carbons development by pyrolysis of potato peels for effective adsorption of endocrine disruptor bisphenol-A. *Journal of Colloid and Interface Science*, *466*, 101–112. https://doi.org/10.1016/j.jcis.2015.12.003

Ayhan, S. (2008). Adsorption of malachite green onto bentonite:Equilibrium and kinetic studies and Process design. *115*, 234–246. *Journal of microporous and mesoporous materials.*7(67) 432-429. https://doi.org/10.1016/j.micromeso.2008.01.039.

Bello, O. S., Adesina, K., Samuel, A., & Fagbenro, O. (2019). Functionalized coconut husks for rhodamine-B dye sequestration. *Applied Water Science*, (4)1–15. https://doi.org/10.1007/s13201-019-1051-4

Bello, O. S., Alao, O. C., Alagbada, T. C., Agboola, O. S., Omotoba, O. T., & Abikoye, O. R. (2021). A renewable, sustainable and low-cost adsorbent for ibuprofen removal. *Water Science and Technology*, *83*(1), 111–122. https://doi.org/10.2166/wst.2020.551

Bello, O. S., Alao, O. C., Alagbada, T. C., & Olatunde, A. M. (2019). Biosorption of ibuprofen using functionalized bean husks. *Sustainable Chemistry and Pharmacy*, *13(4)*, 100151. https://doi.org/10.1016/j.scp.2019.100151

Bello, O. S., Lasisi, B. M., Adigun, O. J., Ephraim, V., & Kalijadis, A. N. A. M. (2017). Scavenging Rhodamine B dye using moringa oleifera seed pod. *Chemical Speciation and Bioavailability*, *29*(1), 120–134. https://doi.org/10.1080/09542299.2017.1356694

Bello, O. S., Oluwadamilola, E., Adesina, K., Adewale, S., Inyinbor, A. A., & Dada, O. A. (2019). Rhodamine B dye sequestration using Gmelina aborea leaf powder. *Heliyon*, *5*(10), 2872. https://doi.org/10.1016/j.heliyon.2019.e02872

Bhatti, Haq N, Safa, Y., Yakout, S. M., Shair, O. H., Iqbal, M., & Nazir, A. (2020).

Efficient removal of dyes using carboxymethyl cellulose/alginate/polyvinyl alcohol/rice husk composite: Adsorption/desorption, kinetics and recycling studies. *International Journal of Biological Macromolecules*, *150*, 861–870. https://doi.org/10.1016/j.ijbiomac.2020.02.093

Bhatti, Haq Nawaz, Mahmood, Z., Abida, K., Yakout, S. M., Shair, O. H., & Iqbal, M. (2020). Biocomposites of polypyrrole , polyaniline and sodium alginate with cellulosic biomass: Adsorption-desorption , kinetics and thermodynamic studies for the removal of 2,4-dichlorophenol. *International Journal of Biological Macromolecules*, *153*, 146–157. https://doi.org/10.1016/j.ijbiomac.2020.02.306

Bouhamed, F., Elouear, Z., & Bouzid, J. (2012). Adsorptive removal of copper(II) from aqueous solutions on activated carbon prepared from Tunisian date stones: Equilibrium, kinetics and thermodynamics. *Journal of the Taiwan Institute of Chemical Engineers*, *43*(5), 741–749. https://doi.org/10.1016/j.jtice.2012.02.011

Chandrasekaran, A., Patra, C., Narayanasamy, S., & Subbiah, S. (2020). Adsorptive removal of Ciprofloxacin and Amoxicillin from single and binary aqueous systems using acid-activated carbon from Prosopis juliflora. *Environmental Research*, *188*(4), 109825. https://doi.org/10.1016/j.envres.2020.109825

Charola, S., Yadav, R., Das, P., & Maiti, S. (2018). Fixed-bed adsorption of Reactive Orange 84 dye onto activated carbon prepared from empty cotton flower agro-waste. *Sustainable Environment Research*, *28*(6), 298–308. https://doi.org/10.1016/j.serj.2018.09.003

Choina, J., Bagabas, A., Fischer, C., Flechsig, G. U., Kosslick, H., Alshammari, A., & Schulz, A. (2015). The influence of the textural properties of ZnO nanoparticles on adsorption and photocatalytic remediation of water from pharmaceuticals. *Catalysis Today*, *24*(12), 47–54. https://doi.org/10.1016/j.cattod.2014.05.014

Choudhary, M., Kumar, R., & Neogi, S. (2020). Activated biochar derived from Opuntia ficus-indica for the efficient adsorption of malachite green dye , Cu+2 and Ni+2 from water. *Journal of Hazardous Materials*, *392*(3), 122441.

https://doi.org/10.1016/j.jhazmat.2020.122441

Cruz, G. J. F., Mondal, D., Rimaycuna, J., Soukup, K., Gómez, M. M., Solis, J. L., & Lang, J. (2020). Agrowaste derived biochars impregnated with ZnO for removal of arsenic and lead in water. *Journal of Environmental Chemical Engineering*, *8*(3), 103800. https://doi.org/10.1016/j.jece.2020.103800

D'Alessandro, S., Scaccabarozzi, D., Signorini, L., Perego, F., Ilboudo, D. P., Ferrante, P., & Delbue, S. (2020). The Use of Antimalarial Drugs against Viral Infection. *MDPI Microorganisms*, (6)1–26. https://doi.org/10.1016/j.micro.2020.109825

Dabi, D., Babi, S., & Skori, I. (2019). *Chemosphere The role of photodegradation in the environmental fate of hydroxychloroquine*. *230*, 268–277. https://doi.org/10.1016/j.chemosphere.2019.05.032

Dada, A. O., Ojediran, J. O., & Olalekan, A. P. (2013). Sorption of Pb2+ from aqueous solution unto modified rice husk: Isotherms studies. *Advances in Physical Chemistry*, *24(6) 123-166*. https://doi.org/10.1155/2013/842425

Dada, A O, Adekola, F. A., & Odebunmi, E. O. (2014). Kinetics , Isotherms And Thermodynamics Studies Of Sorption Of Cu^{2+} Onto Novel Zerovalent Iron Nanoparticles. *Covenant Journal of Physical and Life Sciences 2*(1), 24–53. https://doi.org/10.1155/2013/842425

Dada, A O, Adekola, F. A., & Odebunmi, E. O. (2017). A novel zerovalent manganese for removal of copper ions : synthesis , characterization and adsorption studies. *Applied Water Science*, *7*(3), 1409–1427. https://doi.org/10.1007/s13201-015-0360-5

Dada, A O, Ojediran, J. O., & Olalekan, A. P. (2013). Sorption of Pb^{2+} from Aqueous Solution unto Modified Rice Husk : Isotherms Studies. *Hindawi Journal of Chemistry*. 6(5), 134-137. http://dx.doi.org/10.1155/2013/842425

Dada, Adewumi O., Adekola, F. A., & Odebunmi, E. O. (2017). Kinetics, mechanism, isotherm and thermodynamic studies of liquid phase adsorption of Pb^{2+} onto wood

activated carbon supported zerovalent iron (WAC-ZVI) nanocomposite. *Cogent Chemistry*, *3*(1), 1–20. https://doi.org/10.1080/23312009.2017.1351653

Dada, Adewumi O, Adekola, F. A., & Odebunmi, E. O. (2017). Environmental Nanotechnology , Monitoring & Management Liquid phase scavenging of Cd (II) and Cu (II) ions onto novel nanoscale zerovalent manganese (nZVMn): Equilibrium , kinetic and thermodynamic studies. *Environmental Nanotechnology, Monitoring & Management*, *8*(5), 63–72. https://doi.org/10.1016/j.enmm.2017.05.001

Dada, Adewumi O, Adekola, F. A., Odebunmi, E. O., Dada, F. E., Bello, O. M., Akinyemi, B. A., … Umukoro, O. G. (2020). Sustainable and low-cost Ocimum gratissimum for biosorption of indigo carmine dye: kinetics, isotherm, and thermodynamic studies. *International Journal of Phytoremediation*, *12*(6), 1–14. https://doi.org/10.1080/15226514.2020.1785389

Dada, Adewumi O, Latona, D. F., Ojediran, O. J., & Nath, O. O. (2016). Adsorption of Cu(II) onto Bamboo Supported Manganese (BS-Mn) Nanocomposite : Effect of Operational Parameters , Kinetic , Isotherms , and Thermodynamic Studies. *Journal of Applied Science and Environmental Management*, *20*(2), 409–422.

Dada, Adewumi Oluwasogo, Inyinbor, A., Adekola, F., & Odebunmi, E. (2018). Adsorption ofRhodamine B dye onto chitosansupported zerovalent Iron. *International Journal of Civil Engineering and Technology*, *9*(13), 1591–1609. https://doi.org/10.1155/2013/842425

Dada, O. A., Adekola, F. A., Odebunmi, E. O., Dada, F. E., Bello, O. S., & Ogunlaja, A. S. (2020). Bottom-up approach synthesis of core-shell nanoscale zerovalent iron (CS-nZVI): Physicochemical and spectroscopic characterization with Cu(II) ions adsorption application. *MethodsX*, *7*, 100976. https://doi.org/10.1016/j.mex.2020.100976

Dada, O. A. F. A. A., Odebunmi, E. O., Inyinbor, A. A., Akinyemi, B. A., & Ilesanmi, D. A. (2019). Kinetics and Thermodynamics of Adsorption of Rhodamine B onto

Bentonite Supported Nanoscale Zerovalent Iron Nanocomposite Kinetics and Thermodynamics of Adsorption of Rhodamine B onto Bentonite Supported Nanoscale Zerovalent Iron Nanocomposite. *3rd International Conference on Science and Sustainable Development(ICSSD)*, *1299*(012106). https://doi.org/10.1088/1742-6596/1299/1/012106

Dasgupta, N., Ranjan, S., & Chidambaram, R. (2017). Applications of nanotechnology in agriculture and water quality management. *Environmental Chemistry Letters*. 12(7), 122-126 https://doi.org/10.1007/s10311-017-0648-9

Deb, A., Kanmani, M., Debnath, A., Bhowmik, K. L., & Saha, B. (2019). Ultrasonic assisted enhanced adsorption of methyl orange dye onto polyaniline impregnated zinc oxide nanoparticles: Kinetic, isotherm and optimization of process parameters. *Ultrasonics Sonochemistry*, *54*(2), 290–301. https://doi.org/10.1016/j.ultsonch.2019.01.028

Ding, C., Cheng, W., Sun, Y., & Wang, X. (2015). Effects of Bacillus subtilis on the reduction of U(VI) by nano-FeO. *Geochimica et Cosmochimica Acta*, *165*, 86–107. https://doi.org/10.1016/j.gca.2015.05.036

Ekpete, O. A., Marcus, A. C., & Osi, V. (2017b). Preparation and Characterization of Activated Carbon Obtained from Plantain (Musa paradisiaca) Fruit Stem. *Hindawi Journal of Chemistry, 8(5) 145-149*. https://doi.org/10.1155/2017/8635615

Elhag Elhussien, M. (2017). Removal of Ciprofloxacin Hydrochloride from Aqueous Solution by Pomegranate Peel Grown in Alziedab Agricultural Scheme - River Nile State, Sudan. *Advances in Biochemistry*, *5*(5), 89. https://doi.org/10.11648/j.ab.20170505.12

Eltaweil, A. S., Mohamed, H. A., & El-monaem, E. M. A. (2020). Mesoporous magnetic biochar composite for enhanced adsorption of malachite green dye : Characterization , adsorption kinetics , thermodynamics and isotherms. *Advanced Powder Technology*, 8(1), 1–11. https://doi.org/10.1016/j.apt.2020.01.005

Ferreira, R. ., De Lima, H. ., Candido, A. ., Couto Junior, O. ., Arroyo, P. ., De Carvalho,

K. ., … Barros, A. S. . (2015). Adsorption of Paracetamol Using Activated Carbon of Dende and Babassu. *International Journal of Biological, Agricultural, Food and Biotechnological Engineering*, *9*(7) 1134-1345. https://doi.org/10.1016/j.ecoenv.2017.01.006

Foo, K. Y., & Hameed, B. H. (2010). Insights into the modeling of adsorption isotherm systems. *Chemical Engineering Journal*, *156*, 2–10. https://doi.org/10.1016/j.cej.2009.09.013

Gan, H. Y., Leow, L.-E., & Ong, S.-T. (2017). Utilization of corn cob and TiO2 photocatalyst thin films for dyes removal. *Acta Chimica Slovenica*, *64*(1), 144–158. https://doi.org/10.17344/acsi.2016.2983

Ghani, Z. A., Yusoff, M. S., & Andas, J. (2015). Review on Applications of Nanoparticles in Landfill Leachate Treatment. *Journal of Scientific Research*. *802*, 525–530. https://doi.org/10.4028/www.scientific.net/AMM.802.525

Guechi, E. K., & Hamdaoui, O. (2016). Sorption of malachite green from aqueous solution by potato peel: Kinetics and equilibrium modeling using non-linear analysis method. *Arabian Journal of Chemistry*, *9*, S416–S424. https://doi.org/10.1016/j.arabjc.2011.05.011

Gündüz, F., & Bayrak, B. (2017). Biosorption of malachite green from an aqueous solution using pomegranate peel: Equilibrium modelling, kinetic and thermodynamic studies. *Journal of Molecular Liquids*, *243*, 790–798. https://doi.org/10.1016/j.molliq.2017.08.095

Gupta, N., Kushwaha, A. K., & Chattopadhyaya, M. C. (2016). Application of potato (Solanum tuberosum) plant wastes for the removal of methylene blue and malachite green dye from aqueous solution. *Arabian Journal of Chemistry*, *9*, S707–S716. https://doi.org/10.1016/j.arabjc.2011.07.021

Gupta, V. K., Pathania, D., Singh, P., Kumar, A., & Rathore, B. S. (2014). Adsorptional removal of methylene blue by guar gum–cerium (IV) tungstate hybrid cationic exchanger. *Carbohydrate Polymers*, *101*, 684–691.

https://doi.org/10.1016/j.carbpol.2013.09.092

Howard, P. H., & Muir, D. C. G. (2011). Identifying New Persistent and Bioaccumulative Organics Among Chemicals in Commerce II: Pharmaceuticals. *Environmental Science and Technology*, *45*, 6938–6946. https://doi.org/10.1016/j.ecoenv.2017.01.006

Inyinbor, A. A., Adekola, F. A., & Olatunji, G. A. (2016). Kinetics , isotherms and thermodynamic modeling of liquid phase adsorption of Rhodamine B dye onto Raphia hookerie fruit epicarp. *Water Resources and Industry*, *15*, 14–27. https://doi.org/10.1016/j.wri.2016.06.001

Jasper, E. E., Ajibola, V. O., & Onwuka, J. C. (2020). Nonlinear regression analysis of the sorption of crystal violet and methylene blue from aqueous solutions onto an agro-waste derived activated carbon. *Applied Water Science*, *10*(6), 1–11. https://doi.org/10.1007/s13201-020-01218-y

Kalderis, D., Kayan, B., Akay, S., Kulaksız, E., & Gözmen, B. (2017). Adsorption of 2,4-dichlorophenol on paper sludge/wheat husk biochar: Process optimization and comparison with biochars prepared from wood chips, sewage sludge and hog fuel/demolition waste. *Biochemical Pharmacology*. 18(3) 18-23 https://doi.org/10.1016/j.jece.2017.04.039

Karnati, S. R., Agbo, P., & Zhang, L. (2020). Applications of silica nanoparticles in glass/carbon fiber-reinforced epoxy nanocomposite. *Composites Communications*, *17*(10), 32–41. https://doi.org/10.1016/j.coco.2019.11.003

Kumar, K. V., & Kumaran, A. (2005). Removal of methylene blue by mango seed kernel powder. *Biochemical Engineering Journal*, *27*(1), 83–93. https://doi.org/10.1016/j.bej.2005.08.004

Lazim, Z. M., Hadibarata, T., Yusop, Z., Nazifa, T. H., Abdullah, N. H., & Nuid, M. (2021). Bisphenol A Removal by Adsorption Using Waste Biomass : Isotherm and Kinetic Studies. *Biointerface Research in Applied Chemistry*, *11*(1), 8467–8481.

Leupin, O. X., & Hug, S. J. (2005). Oxidation and removal of arsenic (III) from aerated groundwater by filtration through sand and zero-valent iron. *Water Research*, *39*(9), 1729–1740. https://doi.org/10.1016/j.watres.2005.02.012

Li, R., Wang, Z., Guo, J., Li, Y., Zhang, H., Zhu, J., & Xie, X. (2018). Enhanced adsorption of ciprofloxacin by KOH modified biochar derived from potato stems and leaves. *Water Science and Technology*, *77*(4), 1127–1136. https://doi.org/10.2166/wst.2017.636

Li, Y., Du, Q., Liu, T., Sun, J., Jiao, Y., Xia, Y., … Wu, D. (2012). Equilibrium, kinetic and thermodynamic studies on the adsorption of phenol onto graphene. *Materials Research Bulletin*, *47*(8), 1898–1904. https://doi.org/10.1016/j.materresbull.2012.04.021

Lindroos, M., Hörnström, D., Larsson, G., Gustavsson, M., & Maris, A. J. A. Van. (2019). Continuous removal of the model pharmaceutical chloroquine from water using melanin-covered Escherichia coli in a membrane bioreactor. *Journal of Hazardous Materials*, *365*(9), 74–80. https://doi.org/10.1016/j.jhazmat.2018.10.081

Malik, R., Ramteke, D. S., & Wate, S. R. (2007). Adsorption of malachite green on groundnut shell waste based powdered activated carbon. *Waste and Biomass Valorization*, *27*, 1129–1138. https://doi.org/10.1016/j.wasman.2006.06.009

Masoudian, N., Rajabi, M., & Ghaedi, M. (2019). Titanium oxide nanoparticles loaded onto activated carbon prepared from bio-waste watermelon rind for the efficient ultrasonic-assisted adsorption of congo red and phenol red dyes from wastewaters. *Polyhedron*, *173*, 114105. https://doi.org/10.1016/j.poly.2019.114105

Menya, E., Olupot, P. W., Storz, H., Lubwama, M., & Kiros, Y. (2017). Chemical Engineering Research and Design Production and performance of activated carbon from rice husks for removal of natural organic matter from water : A review. *Chemical Engineering Research and Design*, *129*, 271–296. https://doi.org/10.1016/j.cherd.2017.11.008

Mohammed, A. A., Al-Musawi, T. J., Kareem, S. L., Zarrabi, M., & Al-Ma’abreh, A. M.

(2019). Simultaneous adsorption of tetracycline, amoxicillin, and ciprofloxacin by pistachio shell powder coated with zinc oxide nanoparticles. *Arabian Journal of Chemistry*, *13*(3), 4629–4643. https://doi.org/10.1016/j.arabjc.2019.10.010

Mountassir, E., Mouchtari, E., Daou, C., Rafqah, S., Najjar, F., Piram, A., … Wong-wah-chung, P. (2020). TiO_2 and activated carbon of Argania Spinosa tree nutshells composites for the adsorption photocatalysis removal of pharmaceuticals from aqueous media. *Journal of Photochemistry & Photobiology*. *388*(7). https://doi.org/10.1016/j.jphotochem.2019.112183

Mudyawabikwa, B., Mungondori, H. H., Tichagwa, L., & Katwire, D. M. (2017). Methylene blue removal using a low-cost activated carbon adsorbent from tobacco stems: Kinetic and equilibrium studies. *Water Science and Technology*, *75*(10), 2390–2402. https://doi.org/10.2166/wst.2017.041

Muhammed, Y. (2020). Biosafety and Health Molecular targets for COVID-19 drug development: Enlightening Nigerians about the pandemic and future treatment. *Biosafety and Health*. 6(18), 334-338. https://doi.org/10.1016/j.bsheal.2020.07.002

Muinde, V. M., Onyari, J. M., Wamalwa, B., & Wabomba, J. N. (2020). Environmental Chemistry and Ecotoxicology Adsorption of Malachite green dye from aqueous solutions using mesoporous chitosan – Zinc Oxide composite material. *Environmental Chemistry and Ecotoxicology*, *2*, 115–125. https://doi.org/10.1016/j.enceco.2020.07.005

Nguyen, H. T., Phuong, V. N., & Van, T. N. (2020). Environmental Technology & Innovation Low-cost hydrogel derived from agro-waste for veterinary antibiotic removal: Optimization , kinetics , and toxicity evaluation. *Environmental Technology & Innovation*, *20*, 101098. https://doi.org/10.1016/j.eti.2020.101098

Nworie, F. ., Nwabue, F., Ikelle, I. I., Ogah, A. O., Elom, N., Illochi, N. ., … Oroke, C. . (2018). Activated Plantain Peel Biochar As Adsorbent For Sorption of Zinc (II) Ions: Equilibrium and Kinetics Studies. *Journal of the Turkish Chemical Society*, *5*(3), 1257–1270. https://doi.org/10.1016/j.ecoenv.2017.01.006

Obi-ani, N. A., Anikwenze, C., Isiani, M. C., Obi-ani, N. A., Anikwenze, C., & Isiani, M. C. (2020). Cogent Arts & Humanities Social media and the Covid-19 pandemic: Observations from Nigeria Social media and the Covid-19 pandemic: Observations from Nigeria. *Cogent Arts & Humanities*, *7*(1). https://doi.org/10.1080/23311983.2020.1799483

Ojediran, J. O., Dada, A. O., Aniyi, S. O., & David, R. O. (2020). Functionalized Zea Mays Cob (FZMC) as low-cost agrowaste for effective adsorption of malachite green dyes data set. *Chemical Data Collections*, *30*, 100563. https://doi.org/10.1016/j.cdc.2020.100563

Okereke, J. N., & Obasi, K. (2016). Environmental and Health Impact of Industrial Wastewater Effluents in Nigeria - A Review. *International Journal of Advanced Research in Biological Sciences.* 3(6), 2349-8069. http://s-o-i.org/1.15/ijarbs-2016-3-6-8.

Olarinmoye, O., Bakare, A., Ugwumba, O., & Hein, A. (2016). Quantification of pharmaceutical residues in wastewater impacted surface waters and sewage sludge from Lagos, Nigeria. *Journal of Environmental Chemistry and Ecotoxicology*, *8*(3), 14–24. https://doi.org/10.5897/JECE2015.0364

Onaga, F. M., Aguiar, M. B., Parolo, M. E., & Avena, M. J. (2021). Insights of competitive adsorption on activated carbon of binary caffeine and diclofenac solutions. *Journal of Environmental Management*, *278*(P2), 111523. https://doi.org/10.1016/j.jenvman.2020.111523

Orimolade, B., Adekola, F., & Aminat, M. A. (2018). Removal of Bisphenol-A from Aqueous Solution Using Rice Husk Nanosilica: Adsorption Kinetics , Equilibrium and Thermodynamic Studies. 66(8), 117-119. *Journal of Chemical Data Collections.* https://doi.org/10.1016/j.cdc.2020.100563

Pour, M. N., Rangkooy, H. A., Jahani, F., & Golbaghi, A. (2019). Removal of styrene by the synthesized ZnO nanoparticles coated on the activated carbon adsorbent in the presence of UV irradiation. *Environmental HealthEngineering and Management*

Journal. *6*(4), 225–232. https://doi.org/10.15171/EHEM.2019.25

Qiu, X., Qin, J., Xu, M., Kang, L., & Hu, Y. (2019). Biointerfaces Organic-inorganic nanocomposites fabricated via functional ionic liquid as the bridging agent for Laccase immobilization and its application in 2,4- dichlorophenol removal. *Colloids and Surfaces B: Biointerfaces*, *179*(4), 260–269. https://doi.org/10.1016/j.colsurfb.2019.04.002

Quesada, Heloise B., Cusioli, L. F., de O Bezerra, C., Baptista, A. T. A., Nishi, L., Gomes, R. G., & Bergamasco, R. (2019). Acetaminophen adsorption using a low-cost adsorbent prepared from modified residues of *Moringa oleifera Lam*. seed husks. *Journal of Chemical Technology and Biotechnology*, *94*(10), 3147–3157. https://doi.org/10.1002/jctb.6121

Quesada, Heloise Beatriz, Baptista, T. A. A., Cusioli, L. F., Seibert, D., Bezerra, C. D. O., & Bergamasco, R. (2019). Surface water pollution by pharmaceuticals and an alternative of removal by low-cost adsorbents : A review. *Chemosphere*, *222*, 766–780. https://doi.org/10.1016/j.chemosphere.2019.02.009

Rajasulochana, P., & Preethy, V. (2016). Comparison on efficiency of various techniques in treatment of waste and sewage water – A comprehensive review. *Resource-Efficient Technologies*, 2405–6537. https://doi.org/10.1016/j.reffit.2016.09.004

Renita, A. A., Kumar, P. S., Srinivas, S., Priyadharshini, S., & Karthika, M. (2017). A review on analytical methods and treatment techniques of pharmaceutical wastewater. *Desalination and Water Treatment*, *87*, 160–178. https://doi.org/10.5004/dwt.2017.21311

Rong, X., Xie, M., Kong, L., Natarajan, V., Ma, L., & Zhan, J. (2019). The magnetic biochar derived from banana peels as a persulfate activator for organic contaminants degradation. *Chemical Engineering Journal*, *372*(4), 294–303. https://doi.org/10.1016/j.cej.2019.04.135

Rudd, N. D., Wang, H., Fuentes-Fernandez, E. M. A., Teat, S. J., Chen, F., Hall, G., … Li, J. (2016). Highly Efficient Luminescent Metal-Organic Framework for the

Simultaneous Detection and Removal of Heavy Metals from Water. *ACS Applied Materials and Interfaces*, *8*(44), 30294–30303. https://doi.org/10.1021/acsami.6b10890

Saha, P., Chowdhury, S., Gupta, S., Kumar, I., & Kumar, R. (2010). Assessment on the removal of malachite green using tamarind fruit shell as biosorbent. *Clean - Soil, Air, Water*, *38*(5–6), 437–445. https://doi.org/10.1002/clen.200900234

Sartape, A. S., Mandhare, A. M., Jadhav, V. V., Raut, P. D., Anuse, M. A., & Kolekar, S. S. (2017). Removal of malachite green dye from aqueous solution with adsorption technique using Limonia acidissima (wood apple) shell as low cost adsorbent. *Arabian Journal of Chemistry*, *10*, S3229–S3238. https://doi.org/10.1016/j.arabjc.2013.12.019

Saucier, C., Karthickeyan, P., Ranjithkumar, V., Lima, E. C., Reis, G. S. dos, & Brum, I. A. . (2017). Efficient removal of amoxicillin and paracetamol from aqueous solutions using magnetic activated carbon. *Environmental Science and Pollution Research*. https://doi.org/10.1007/s11356-016-8304-7

Shen, Y., & Fu, Y. (2018). KOH-activated rice husk char via CO_2 pyrolysis for phenol adsorption. *Materials Today Energy*, *9*, 397–405. https://doi.org/10.1016/j.mtener.2018.07.005

Siddiqui, S. I., Manzoor, O., & Chaudhry, S. A. (2018). Nigella sativa seed based nanocomposite-MnO_2/BC: An antibacterial material for photocatalytic degradation, and adsorptive removal of dye from water. *Environmental Research*. 4(12) 123-145 https://doi.org/10.1016/j.envres.2018.11.044

Sonawane, G. H., Patil, S. P., & Sonawane, S. H. (2018). Nanocomposites and Its Applications. *Applications of Nanomaterials*. 4(12) 11-16. https://doi.org/10.1016/B978-0-08-101971-9.00001-6

Spessato, L., Bedin, K. C., Cazetta, A. L., Souza, I. P. A. F., Duarte, V. A., Crespo, L. H. S., … Almeida, V. C. (2019). KOH-super activated carbon from biomass waste : Insights into the paracetamol adsorption mechanism and thermal regeneration

cycles. *Journal of Hazardous Materials*, *371*(2), 499–505. https://doi.org/10.1016/j.jhazmat.2019.02.102

Sridhar, R., Ramanane, U. U., & Rajasimman, M. (2018). ZnO nanoparticles – Synthesis, characterization and its application for phenol removal from synthetic and pharmaceutical industry wastewater. *Environmental Nanotechnology, Monitoring and Management*, *10*, 388–393. https://doi.org/10.1016/j.enmm.2018.09.003

Steplin, P. S., Kumar, G. A., Sarala, L., Rajaram, R., Sathiyan, A., Merlin, P., & Lydia, I. S. (2018). Photocatalytic Degradation of Rhodamine B Using Zinc Oxide Activated Charcoal Polyaniline Nanocomposite and Its Survival Assessment Using Aquatic Animal Model. *Sustainable Chemistry and Engineering*, *6*, 258–267. https://doi.org/10.1021/acssuschemeng.7b02335

Sudhakar, P, Mall, I. D., & Srivastava, V. C. (2015). Adsorptive removal of bisphenol-A by rice husk ash and granular activated carbon — A comparative study. *Desalination and Water Treatment*, 6(5), 37–41. https://doi.org/10.1080/19443994.2015.1050700

Sudhakar, Padmaja, & Soni, H. (2018). PT SC. *Biochemical Pharmacology*. https://doi.org/10.1016/j.jece.2018.04.013

Sukla Baidya, K., & Kumar, U. (2021). Adsorption of brilliant green dye from aqueous solution onto chemically modified areca nut husk. *South African Journal of Chemical Engineering*, *35*(7), 33–43. https://doi.org/10.1016/j.sajce.2020.11.001

Supong, A., Bhomick, P. C., Baruah, M., Pongener, C., Sinha, U. B., & Sinha, D. (2019). Adsorptive removal of Bisphenol A by biomass activated carbon and insights into the adsorption mechanism through density functional theory calculations. *Sustainable Chemistry and Pharmacy*, *13*(4), 100159. https://doi.org/10.1016/j.scp.2019.100159

Tapia-Orozco, N., Ibarra-Cabrera, R., Tecante, A., Gimeno, M., Parra, R., & Garcia-Arrazola, R. (2016). Removal strategies for endocrine disrupting chemicals using cellulose-based materials as adsorbents: A review. *Journal of Environmental*

Chemical Engineering, *4*(3), 3122–3142. https://doi.org/10.1016/j.jece.2016.06.025

Tursi, A., Chatzisymeon, E., Chidichimo, F., Beneduci, A., & Chidichimo, G. (2018). Removal of Endocrine Disrupting Chemicals from Water : Adsorption of Bisphenol-A by Biobased Hydrophobic Functionalized Cellulose. *International Journal of Environmental Research and Public Health*, *15*, 2419. https://doi.org/10.3390/ijerph15112419

Vinayagam, M., Ramachandran, S., Ramya, V., & Sivasamy, A. (2017). Journal of Environmental Chemical Engineering Photocatalytic degradation of orange G dye using ZnO / biomass activated carbon nanocomposite. *Journal of Environmental Chemical Engineering*, 6(10), https://doi.org/10.1016/j.jece.2017.06.005

Wang, M., Li, G., Huang, L., Xue, J., Liu, Q., Bao, N., & Huang, J. (2017). Study of ciprofloxacin adsorption and regeneration of activated carbon prepared from Enteromorpha prolifera impregnated with H3PO4 and sodium benzenesulfonate. *Ecotoxicology and Environmental Safety*, *139*(10), 36–42. https://doi.org/10.1016/j.ecoenv.2017.01.006

Wang, S., & Ariyanto, E. (2007). Competitive adsorption of malachite green and Pb ions on natural zeolite. *Journal of Colloid and Interface*, *314*, 25–31. https://doi.org/10.1016/j.jcis.2007.05.032

Yazidi, A., Sellaoui, L., Dotto, G. L., Bonilla-petriciolet, A., Frohlich, C. A., & Ben, A. (2019). Monolayer and multilayer adsorption of pharmaceuticals on activated carbon : Application of advanced statistical physics models. *Journal of Molecular Liquids*, *283*, 276–286. https://doi.org/10.1016/j.molliq.2019.03.101

Zarghi, M. H., Roudbari, A., Jorfi, S., & Jaafarzadeh, N. (2019). Removal of Estrogen Hormones (17B-Estradiol and Estrone) from Aqueous Solutions Using Rice Husk Silica. *Chemical Biochemical Engineering*, *33*(2), 281–293. https://doi.org/10.1016/j.chem.2007.05.032

Zeng, Y., & Xue, Y. (2019). Novel Crayfish Shell Biochar Nanocomposites Loaded with Ag-TiO_2 Nanoparticles Exhibit Robust Antibacterial Activity. *Water, Air, and Soil*

Pollution, 230:50. https://doi.org/10.1016/j.ecoenv.2017.01.006

Zhang, F., Lan, J., Yang, Y., Wei, T., Tan, R., & Song, W. (2013). Adsorption behavior and mechanism of methyl blue on zinc oxide nanoparticles. *Journal of Nanoparticle Research*, *15*(11). https://doi.org/10.1007/s11051-013-2034-2

Zhang, S., & Lu, X. (2018). Treatment of Wastewater Containing Reactive Brilliant Blue KN-R Using TiO_2/BC Composite as Heterogeneous Photocatalyst and Adsorbent. *Chemosphere*. https://doi.org/10.1016/j.chemosphere.2018.05.073

Zheng, J., Zhao, Q., & Ye, Z. (2014). Preparation and characterization of activated carbon fiber (ACF) from cotton woven waste. *Applied Surface Science*, *299*, 86–91. https://doi.org/10.1016/j.apsusc.2014.01.190

Zhou, N., Chen, H., Xi, J., Yao, D., Zhou, Z., Tian, Y., & Lu, X. (2017). Biochars with Excellent Pb (II) Adsorption Property Produced from Fresh and Dehydrated Banana Peels via Hydrothermal Carbonization. *Bioresource Technology*, (Ii). https://doi.org/10.1016/j.biortech.2017.01.074

Zhu, H., Li, Z., & Yang, J. (2018). A novel composite hydrogel for adsorption and photocatalytic degradation of bisphenol A by visible light irradiation. *Chemical Engineering Journal*, *334*(10), 1679–1690. https://doi.org/10.1016/j.cej.2017.11.148

APPENDICES

Appendix 1: Timeline Chart of Research

S/N	Month	Activity
1	July-August 2020	Collection and Preparation of Modified Agro wastes and Zinc Oxide Nanocomposites
2	August-September 2020	Physicochemical and Spectroscopic Characterization
3	October-December 2020	Adsorption of Chloroquine
4	January -March 2021	Adsorption of Malachite Green Dye
5	April-June 2021	Data Analysis and Plotting of graphs (Isotherms, Kinetics and Thermodynamic Studies)
6	June-August 2021	Thesis Write Up

Appendix 2: FTIR spectrum of RHAC and (B) RHAC-ZNO-NC after CQ adsorption

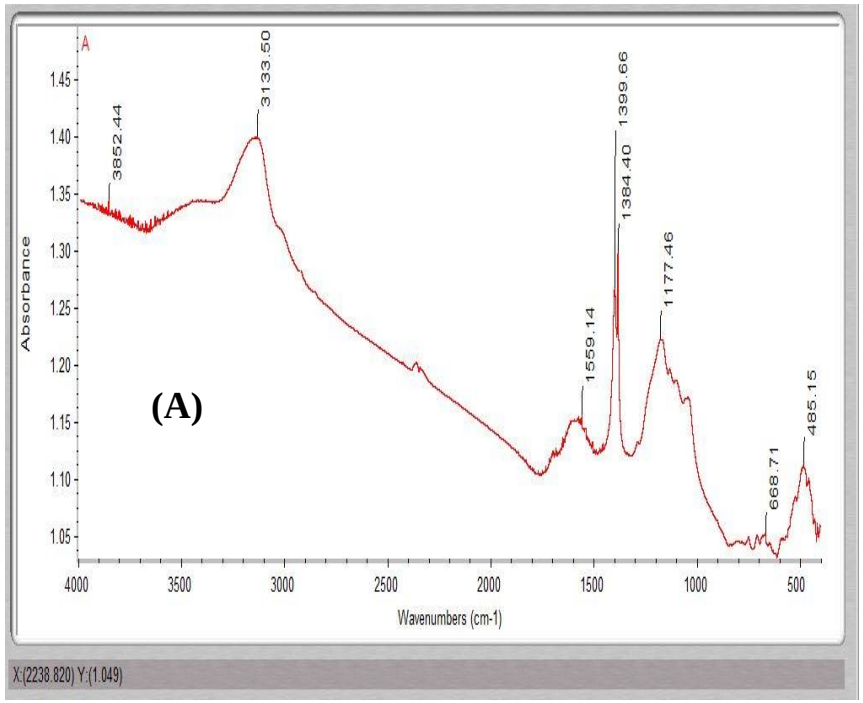

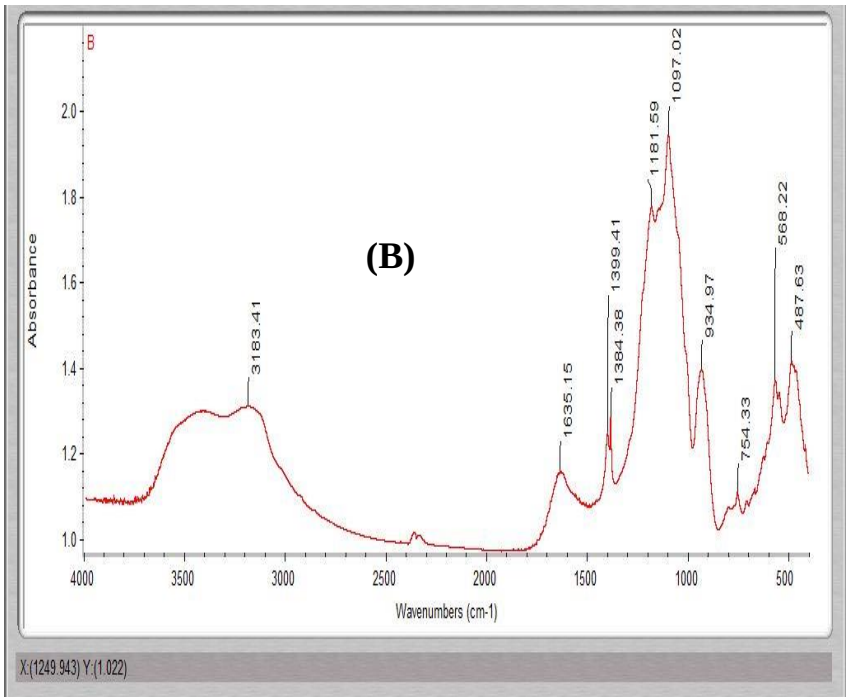

Appendix 3: FTIR spectrum of (A) PPAC and (B) PPAC-ZnO-NC after MG dye Adsorption

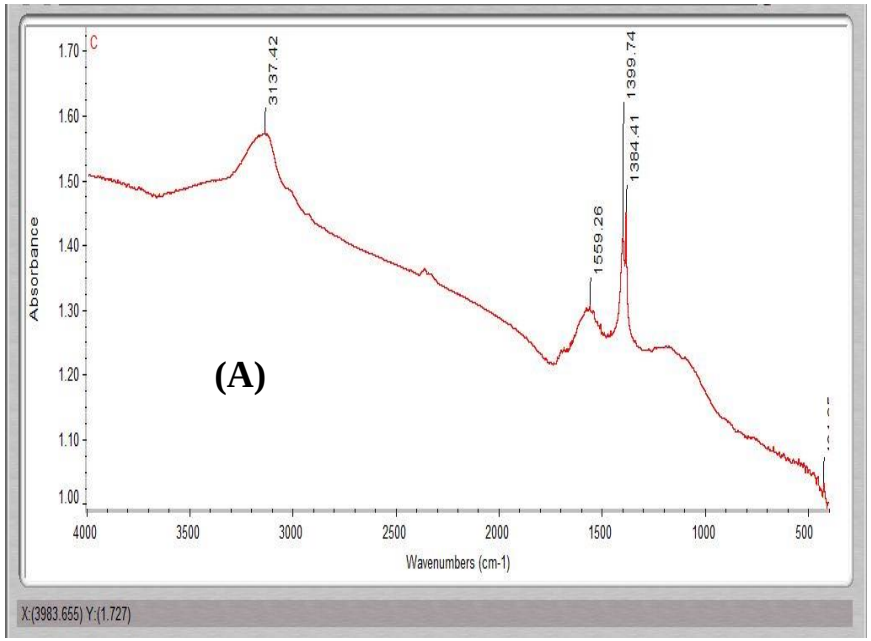

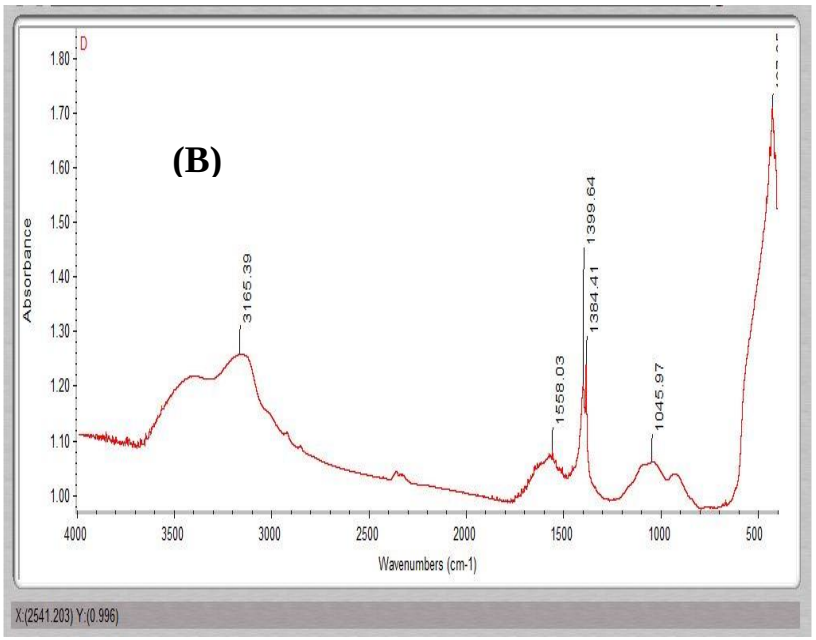

Appendix 4: SEM image of RHAC and (B) RHAC-ZnO-NC after MG dye adsorption

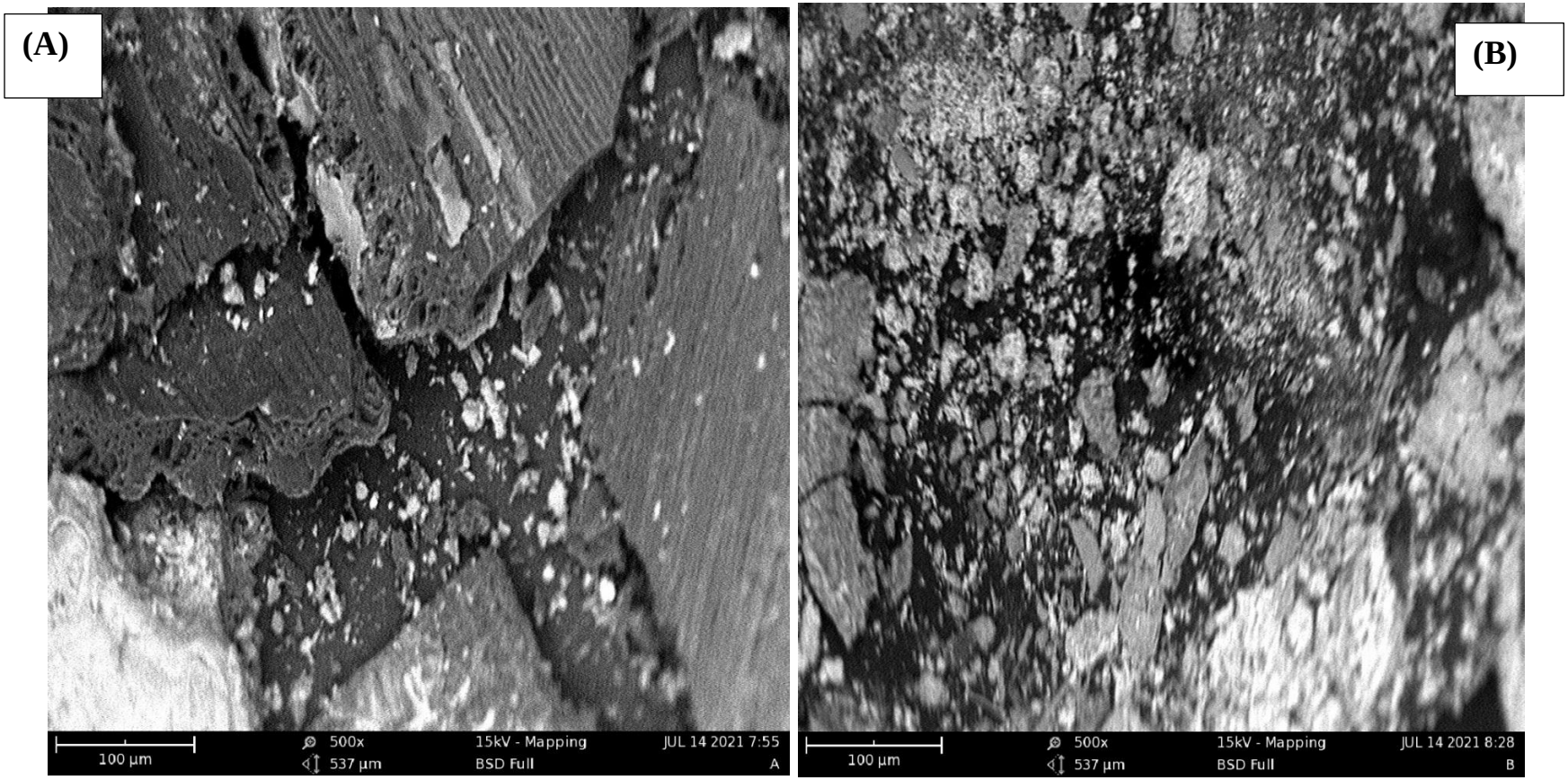

Appendix 5: SEM of A) PPAc and (B) PPAC-ZnO-NC after CQ adsorption

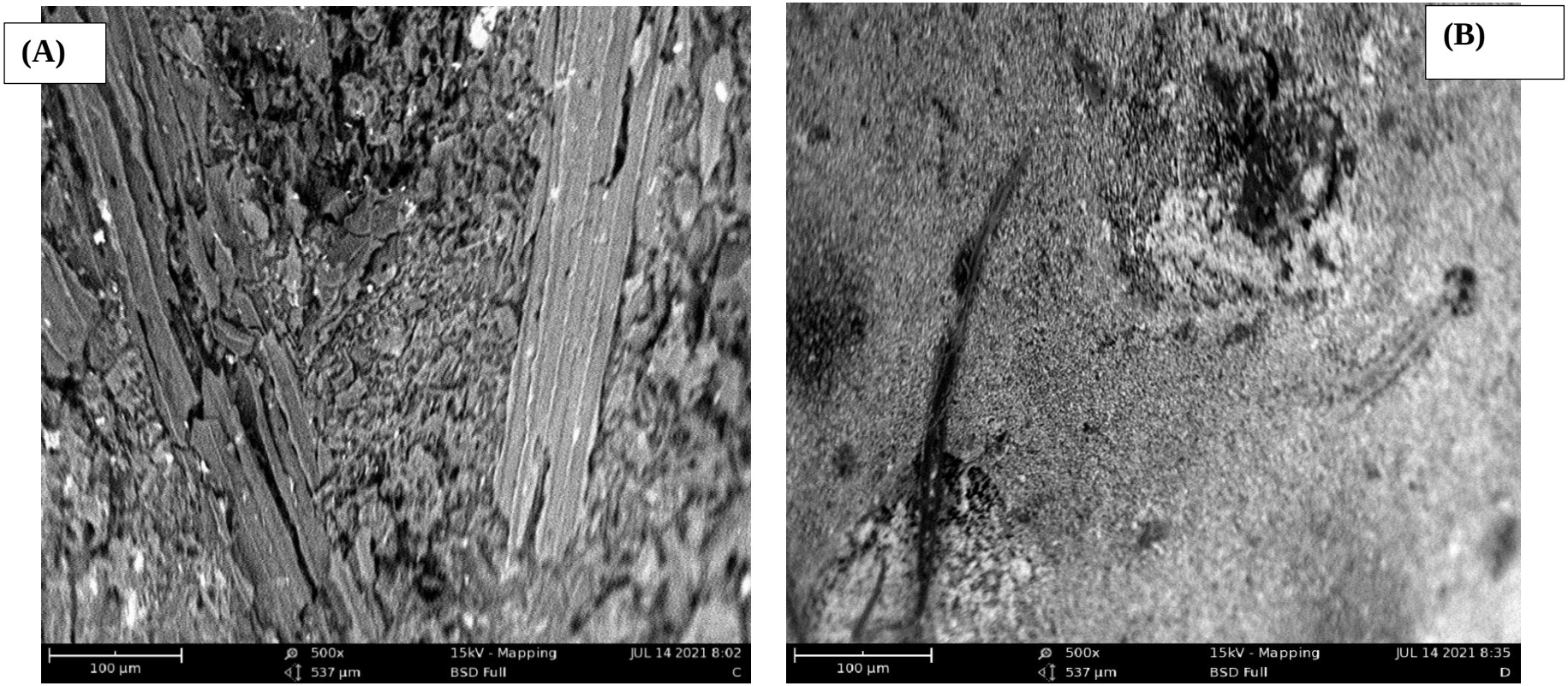

Appendix 6: Kinetic data for RHAC-CQ system

					PFO		PSO		Elovich		IPD	
t (min)	C_t	$Q_t (C_o-C_t)$	% RE	Q_e-Q_t	ln q_e-q_t	t (min)	t/qt	t(min)	$Q_t (C_o-C_t)$	Ln t	$t^{1/2}$	$Q_t (C_o-C_t)$
10	7.27	2.73	27.25	1.37	0.32	10	3.66	10	2.73	2.30	3.16	2.73
30	6.56	3.44	34.44	0.65	0	30	8.71	30	3.44	3.40	5.47	3.44
60	5.44	4.56	45.55	-0.45	0	60	13.17	60	4.56	4.09	7.74	4.56
90	4.73	5.27	52.75	-1.17	0	90	17.06	90	5.27	4.49	9.48	5.27
120	4.01	5.99	59.93	-1.89	0	120	20.02	120	5.99	4.78	10.95	5.99
180	3.35	6.64	66.47	-2.54	0	180	27.08	180	6.64	5.19	13.41	6.64

Appendix 7: Isotherm data for RHAC-CQ system

	Langmuir			Freundlich		Temkin		D-R	
Initial Conc.	q_e	C_e	C_e/q_e	Log C_e	Log Q_e	ln C_e	q_e	Ɛ-sqr	ln q_e
10	6.65	3.35	0.50	0.53	0.82	1.21	6.64	491306	1.89
20	12.79	7.21	0.56	0.86	1.11	1.97	12.79	121683.6	2.54
30	18.80	11.19	0.59	1.05	1.27	2.42	18.80	52780.57	2.93
40	24.97	15.03	0.60	1.18	1.39	2.71	24.96	29911.1	3.21
50	30.92	19.08	0.62	1.283	1.49	2.95	30.92	18821.67	3.43

Appendix 8: Kinetic data for RHAC-ZnO-NC-CQ system

					PFO		PSO		Elovich		IPD	
t (min)	C_t	$Q_t (C_o-C_t)$	% RE	Q_e-Q_t	ln q_e-q_t	t (min)	t/qt	t(min)	$Q_t (C_o-C_t)$	Ln t	$t^{1/2}$	$Q_t (C_o-C_t)$
10	3.29	6.71	67.12	2.61	0.96	10	1.49	10	6.71	2.30	3.16	6.71
30	2.04	7.95	79.54	1.37	0.31	30	3.77	30	7.95	3.40	5.47	7.95
60	1.06	8.93	89.35	0.39	-0.94	60	6.72	60	8.93	4.09	7.74	8.93
90	0.73	9.26	92.61	0.065	-2.73	90	9.72	90	9.26	4.49	9.48	9.26
120	0.67	9.32	93.27	0	0	120	12.87	120	9.32	4.78	10.95	9.32

Appendix 9: Isotherm data for RHAC-ZnO-NC-CQ system

	Langmuir			Freundlich		Temkin		D-R	
Initial Conc.	q_e	C_e	C_e/q_e	Log C_e	Log Q_e	ln C_e	q_e	∑-sqr	ln q_e
10	9.33	0.67	0.072	-0.17	0.97	-0.39	9.33	5977723	2.23
20	17.59	2.40	0.14	0.38	1.25	0.87	17.59	872872.1	2.86
30	22.24	7.66	0.34	0.88	1.35	2.03	22.24	108502.7	3.10
40	31.29	8.71	0.28	0.94	1.49	2.16	31.29	85139.63	3.44
50	38.31	11.69	0.31	1.07	1.58	2.46	38.31	48599.41	3.65

Appendix 10: Kinetic data for PPAC-CQ system

					PFO		PSO		Elovich		IPD	
t (min)	C_t	$Q_t (C_o-C_t)$	% RE	Q_e-Q_t	ln q_e-q_t	t (min)	t/qt	t(min)	$Q_t (C_o-C_t)$	Ln t	$t^{1/2}$	$Q_t (C_o-C_t)$
10		2.01	20.06	7.19	1.97	10	4.98	10	2.01	2.30	3.16	2.01
30		3.25	32.48	5.95	1.78	30	9.23	30	3.25	3.40	5.47	3.25
60		3.57	35.75	5.62	1.73	60	16.78	60	3.57	4.09	7.74	3.57
90		4.94	49.47	4.24	1.45	90	18.19	90	4.94	4.49	9.48	4.94
120		7.16	71.69	2.03	0.71	120	16.73	120	7.16	4.78	10.95	7.16
180		9.19	91.96	0	0	180	19.57	180	9.19	5.19	13.41	9.19

Appendix 11: Isotherm data for PPAC-CQ system

	Langmuir			Freundlich		Temkin		D-R	
Initial Conc.	q_e	C_e	C_e/q_e	Log C_e	Log Q_e	ln C_e	q_e	Ɛ-sqr	ln q_e
10	9.75	0.25	0.025	-0.59	0.98	-1.38	9.74	-1.37	9.74
20	19.53	0.47	0.024	-0.32	1.29	-0.75	19.53	-0.75	19.52
30	22.33	7.66	0.34	0.88	1.34	2.036	22.33	2.036	22.33
40	26.77	13.22	0.49	1.12	1.42	2.58	26.77	2.58	26.77
50	34.68	15.31	0.44	1.18	1.54	2.73	34.69	2.73	34.68

Appendix 12: Kinetic data for PPAC-ZnO-NC-CQ system

					PFO		PSO		Elovich		IPD	
t (min)	C_t	Q_t (C_o-C_t)	% RE	Q_e-Q_t	ln q_e-q_t	t (min)	t/qt	t(min)	Q_t (C_o-C_t)	Ln t	$t^{1/2}$	Q_t (C_o-C_t)
10	8.647059	2.86	13.52941	4.052288	1.399282	10	3.501144	10	2.86	2.30	3.16	2.86
30	8.320261	4.08	16.79739	2.810458	1.033347	30	7.320574	30	4.08	3.40	5.47	4.08
60	7.405229	6.45	25.94771	0.457516	-0.78194	60	9.300912	60	6.45	4.09	7.74	6.45
90	6.555556	6.91	34.44444	0	0	90	13.02744	90	6.91	4.49	9.48	6.91
120	5.640523	6.91	43.59477	0	0	120	17.36991	120	6.91	4.78	10.95	6.91
180	3.54902	6.91	64.5098	0	0	180	26.05487	180	6.91	5.19	13.41	6.91
240	3.091503	6.91	69.08497	0	0	240	34.73983	240	6.91	5.481	15.49193	6.91

Appendix 13: Isotherm data for PPAC-ZnO-NC-CQ system

	Langmuir			Freundlich		Temkin	D-R		
Initial Conc.	q_e	C_e	C_e/q_e	Log C_e	Log Q_e	ln C_e	q_e	Ɛ-sqr	ln q_e
10	8.21	1.79	0.22	0.25	0.91	0.58	8.21	1418605	2.11
20	15.61	4.38	0.28	0.64	1.19	1.47	15.61	304250.9	2.75
30	18.15	11.84	0.65	1.07	1.25	2.47	18.15	47335.73	2.89
40	24.37	15.63	0.64	1.19	1.38	2.74	24.37	27739.69	3.19
50	29.33	20.67	0.70	1.31	1.46	3.03	29.33	16092.13	3.37

Appendix 14: Kinetic data for RHAC-MG system

					PFO		PSO		Elovich		IPD	
t (min)	C_t	$Q_t (C_o-C_t)$	% RE	Q_e-Q_t	ln q_e-q_t	t (min)	t/qt	t(min)	$Q_t (C_o-C_t)$	Ln t	$t^{1/2}$	$Q_t (C_o-C_t)$
10	8.09894	1.90106	19.0106	2.402827	0.876646	10	5.260223	10	1.90106	2.30	3.16	1.90106
30	7.533569	2.466431	24.66431	1.837456	0.608382	30	12.16332	30	2.466431	3.40	5.47	2.466431
60	6.756184	3.243816	32.43816	1.060071	0.058336	60	18.49673	60	3.243816	4.09	7.74	3.243816
90	6.579505	3.420495	34.20495	0.883392	-0.12399	90	26.31198	90	3.420495	4.49	9.48	3.420495
120	6.261484	3.738516	37.38516	0.565371	-0.57027	120	32.0983	120	3.738516	4.78	10.95	3.738516
180	5.660777	4.339223	43.39223	0	0	180	41.82266	180	4.339223	5.19	13.41	4.339223

Appendix 15: Isotherm data for RHAC-MG system

	Langmuir			Freundlich		Temkin	D-R		
Initial Conc.	q_e	C_e	C_e/q_e	Log C_e	Log Q_e	ln C_e	q_e	ℇ-sqr	ln q_e
10	6.339223	3.66	0.577	0.56	0.80	1.29	6.34	370138.1	1.85
20	11.73039	8.26	0.704	0.91	1.07	2.10	11.83	84619.5	2.47
30	17.76219	12.43	0.70	1.08	1.25	2.49	17.86	39775.46	2.88
40	21.49894	18.50	0.86	1.27	1.32	2.93	21.29	17220.72	3.06
50	26.08481	23.92	0.92	1.37	1.42	3.18	26.08	10648.94	3.26

Appendix 16: Kinetic data for RHAC-ZnO-NC-MG system

					PFO		PSO		Elovich		IPD	
t (min)	C_t	$Q_t (C_o-C_t)$	% RE	Q_e-Q_t	ln q_e-q_t	t (min)	t/qt	t (min)	Q_t (C_o-C_t)	Ln t	$t^{1/2}$	$Q_t (C_o-C_t)$
10	6.932862	3.067138	30.67138	5.144876	1.638001	10	3.733509	10	3.067138	2.30	3.16	3.067138
30	6.54417	3.45583	34.5583	4.367491	1.474189	30	8.680982	30	3.45583	3.40	5.47	3.45583
60	5.660777	4.339223	43.39223	3.484099	1.248209	60	13.82736	60	4.339223	4.09	7.74	4.339223
90	5.272085	4.727915	47.27915	3.095406	1.129919	90	19.03587	90	4.727915	4.49	9.48	4.727915
120	4.812721	5.187279	51.87279	2.636042	0.969279	120	23.13351	120	5.187279	4.78	10.95	5.187279
180	4.176678	5.823322	58.23322	0	0	180	28.50733	180	5.823322	5.19	13.41	5.823322

Appendix 17: Isotherm data for RHAC-ZnO-NC-MG system

	Langmuir			Freundlich		Temkin		D-R	
Initial Conc.	q_e	C_e	C_e/q_e	Log C_e	Log Q_e	ln C_e	q_e	Ɛ-sqr	ln q_e
10	7.823322	2.176678	0.278229	0.337794	0.893391	0.7778	7.823322	906925.8	2.057109
20	13.81625	6.183746	0.44757	0.791252	1.14039	1.821924	13.81625	142590.2	2.625846
30	18.93286	11.06714	0.584546	1.044035	1.277216	2.40398	18.93286	47489.2	2.940899
40	24.19788	15.80212	0.653037	1.198715	1.383777	2.760144	24.19788	23894.04	3.186265
50	29.32155	20.67845	0.70523	1.315518	1.467187	3.029092	29.32155	14153.98	3.378323

Appendix 18: Kinetic data for PPAC-CQ system

					PFO		PSO		Elovich		IPD	
t (min)	C_t	$Q_t (C_o-C_t)$	% RE	Q_e-Q_t	ln q_e-q_t	t (min)	t/qt	t(min)	$Q_t (C_o-C_t)$	Ln t	$t^{1/2}$	$Q_t (C_o-C_t)$
10	6.685512	3.314488	33.14488	2.897527	1.063857	10	3.017058	10	3.314488	2.30	3.16	3.314488
30	6.014134	3.985866	39.85866	2.226148	0.800273	30	7.526596	30	3.985866	3.40	5.47	3.985866
60	5.130742	4.869258	48.69258	1.342756	0.294724	60	12.32221	60	4.869258	4.09	7.74	4.869258
90	4.671378	5.328622	53.28622	0.883392	-0.12399	90	16.88992	90	5.328622	4.49	9.48	5.328622
120	4.282686	5.717314	57.17314	0.4947	-0.7038	120	20.98888	120	5.717314	4.78	10.95	5.717314
180	3.787986	6.212014	62.12014	0	0	180	28.97611	180	6.212014	5.19	13.41	6.212014

Appendix 19: Isotherm data for PPAC-CQ system

	Langmuir			Freundlich		Temkin	D-R		
Initial Conc.	q_e	C_e	C_e/q_e	Log C_e	Log Q_e	ln C_e	q_e	Ɛ-sqr	ln q_e
10	8.627451	3.787986	0.439062	0.578408	0.935883	1.331834	8.627451	348304.1	2.154949
20	16.09804	8.477032	0.526588	0.928244	1.206773	2.13736	16.09804	78911.29	2.778697
30	23.31373	16.22615	0.695991	1.210215	1.367612	2.786624	23.31373	22697.2	3.149042
40	28.36601	21.23322	0.748544	1.327016	1.452798	3.055567	28.36601	13440.35	3.345192
50	33.80196	26.79152	0.792603	1.427997	1.528942	3.288085	33.80196	8522.109	3.520519

Appendix 20: Kinetic data for PPAC-ZnO-NC-MG system

					PFO		PSO		Elovich		IPD	
t (min)	C_t	$Q_t (C_o-C_t)$	% RE	Q_e-Q_t	ln q_e-q_t	t (min)	t/qt	t(min)	$Q_t (C_o-C_t)$	Ln t	$t^{1/2}$	$Q_t (C_o-C_t)$
10	6.650177	3.349823	33.49823	3.402827	1.224607	10	2.985232	10	3.349823	2.30	3.16	3.349823
30	6.579505	3.420495	34.20495	3.332155	1.203619	30	8.770661	30	3.420495	3.40	5.47	3.420495
60	6.04947	3.95053	39.5053	2.80212	1.030376	60	15.18784	60	3.95053	4.09	7.74	3.95053
90	5.660777	4.339223	43.39223	2.413428	0.881048	90	20.74104	90	4.339223	4.49	9.48	4.339223
120	5.095406	4.904594	49.04594	1.848057	0.614135	120	24.46686	120	4.904594	4.78	10.95	4.904594
180	4.24735	5.75265	57.5265	0	0	180	26.6562	180	5.75265	5.19	13.41	5.75265

Appendix 21: Isotherm data for PPAC-ZnO-NC-MG system

	Langmuir			Freundlich		Temkin	D-R		
Initial Conc.	q_e	C_e	C_e/q_e	Log C_e	Log Q_e	ln C_e	q_e	Ɛ-sqr	ln q_e
10	6.75265	3.24735	0.4809	0.511529	0.829474	1.177839	6.75265	457353	1.909935
20	12.9258	7.074205	0.547294	0.849678	1.111457	1.956455	12.9258	110941.8	2.559225
30	18.41413	11.58587	0.629183	1.063928	1.265151	2.449786	18.41413	43495.63	2.913119
40	23.53392	16.46608	0.699674	1.21659	1.371694	2.801302	23.53392	22059.41	3.158443
50	26.70671	23.29329	0.872188	1.367231	1.42662	3.148165	26.70671	11213.06	3.284915